LASER-MATTER INTERACTIONS
AT
SUB-MICRON LASER WAVELENGTHS

by

DANIEL PASINI

B.Sc., McGill University, 1978

M.Sc. Institut National de la Recherche Scientifique,

Université du Québec, 1980

A THESIS SUBMITTED IN PARTIAL FULFILMENT OF

THE REQUIREMENT FOR THE DEGREE OF

DOCTOR OF PHILOSOPHY

in

THE FACULTY OF GRADUATE STUDIES

DEPARTMENT OF PHYSICS

We accept this thesis as confirming

to the required standard

THE UNIVERSITY OF BRITISH COLUMBIA

September 1984

© Daniel Pasini, 1984

In presenting this thesis in partial fulfilment of the requirements for an advanced degree at the University of British Columbia, I agree that the Library shall make it freely available for reference and study. I further agree that permission for extensive copying of this thesis for scholarly purposes may be granted by the head of my department or by his or her representatives. It is understood that copying or publication of this thesis for financial gain shall not be allowed without my written permission.

Department of PHYSICS

The University of British Columbia
1956 Main Mall
Vancouver, Canada
V6T 1Y3

Date OCTOBER 18 - 1984

Abstract

In recent years there has been considerable interest in the use of sub-micron wavelength lasers for target irradiation in laser fusion experiments. We present here an experimental investigation of laser-matter interaction in this short wavelength regime. We have irradiated planar targets with 0.532, 0.355 and 0.266 μm laser light with pulse lengths of 2 ns and at intensities ranging from 10^{12} to 5×10^{13} W/cm^2. The results show that for these conditions inverse bremsstrahlung is very effective and leads to very high absorption ($\sim$ 95%). The X-ray spectrum also show that the absorbed energy is well thermalized and only a small number of energetic, non-thermal electrons are present. Also a very low level of scattered light was measured indicating that laser-plasma collective processes are not important. Energy transport was investigated using multilayer targets. Anomalous laser penetration depths in the target were obtained in these measurements. This has been successfully explained in a simple hydrodynamic model where two-dimensional effects were taken into account. In the study of the ablation process wavelength and intensity scaling laws for the mass ablation rate and ablation pressure have been obtained. These results show the inadequacy of the present analytical theories of the laser-driven ablation process.

Table of contents

Chapter 1 Introduction 1

1 – 1 Introduction to controlled fusion research 1

1 – 2 Basic concept of laser fusion 2

1 – 3 Recent developments in laser-matter interaction studies 4

1 – 4 Present investigation 5

1 – 5 Thesis outline 6

Chapter 2 Absorption of laser light in a laser produced plasma 7

2 – 1 Inverse bremsstrahlung absorption 8

2 – 2 Resonance absorption 14

2 – 3 Absorptive and scattering instabilities 18

Chapter 3 Electron thermal transport in laser produced plasmas 22

3 – 1 Basic concepts 23

3 – 2 Spitzer-Härm theory of thermal conductivity: small temperature gradients 25

3 – 3 Thermal transport in laser produced plasmas: large temperature gradients 27

3 – 4 Thermal transport inhibition mechanisms 28

3 – 4 – A Self-generated magnetic field 29

3 – 4 – B Ion acoustic turbulence 29

Chapter 4 Scaling laws for the mass ablation rate and ablation pressure: one dimensional steady-state ablation theory 32

4 – 1 Structure of the laser induced plasma flow 32

4 – 2 One dimensional steady-state ablation theory 35

4 – 2 – A Conservation equations and model assumptions 35

4 – 2 – B Flow solutions in the plasma corona: isothermal expansion 38

4 – 2 – C Flow solutions in the conduction zone: steady state flow 41

4 – 2 – D Scaling laws 42

4 – 2 – E Discussion of model assumptions 45

Chapter 5 Experimental facility and diagnostics 48

5 – 1 Neodymium-glass laser system and the experimental arrangement 48

5 – 2 Irradiation conditions 50

5 – 3 Diagnostics 56

5 – 3 – A Integrating sphere 56

5 – 3 – B Faraday cup 58

5 – 3 – C Differential calorimeter 60

5 – 3 – D X-ray crystal spectrometer 60

5 – 3 – E An in-situ X-ray film calibration technique 62

5 – 3 – F X-ray pinhole camera 74

5 – 3 – G Multichannel X-ray detector 83

5 – 4 Multilayer target fabrication 90

5 – 4 – A Fabrication of CH-glass multilayer targets 90

5 – 4 – B Fabrication of Mg-, Sn-, Ag- and Au-glass multilayer targets 91

Chapter 6 Experimental measurements of laser energy coupling to target 93

6 – 1 Absorption measurements 93

6 – 2 Plasma electron temperature 95

6 – 3 Laser induced plasma instabilities 102

Chapter 7 Investigation of electron energy transport using multilayer targets 106

7 – 1 Experimental conditions 107

7 – 2 Experimental results 110

7 – 3 A hydrodynamic model for laser penetration depth 118

Chapter 8 Experimental scaling laws for the mass ablation rate and the ablation pressure 121

8 – 1 Measurement principle and experimental set-up 121

8 – 2 – A Angular distribution of the plasma energy and velocity 124

8 – 2 – B Experimental scaling laws for the mass ablation rate and the ablation pressure 124

8 – 3 Discussion of the results 126

Chapter 9 Summary and conclusions 133

9 – 1 Experimental effort 133

9 – 2 Experimental results and conclusion 133

9 – 3 New contributions 134

9 – 4 Suggestions for future work 136

Bibliography 136

Appendix 143

List of Figures

1 – 1 Schematic of laser-driven implosion of a pellet containing deuterium-tritium fuel. 3

2 – 1 Schematic picture of electron density profile in a laser produced plasma, showing locations of major coupling processes. 9

2 – 2 Percentage absorption of laser energy in an exponential plasma density profile for different laser wavelengths. 13

2 – 3 Schematic representation of resonance absorption for 'p' polarized light obliquely incident on a plasma density gradient. 16

2 – 4 Feedback mechanism for growth of stimulated Brillouin scattering. 19

3 – 1 Electron and ion distribution in the presence of an electron heat flux Q. 30

4 – 1 Structure of the steady-state plasma flow: density and temperature profiles. 34

4 – 2 Space-time diagram for the densities associated to the shock front, the ablation surface and the absorption surface. 36

4 – 3 Density profile for isothermal plasma expansion. 40

5 – 1 Schematic of the laser system and oscilloscope trace of the oscillator laser pulse. 49

5 – 2 Experimental set-up. 51

5 – 3 Backscatter signal as function of the lens position. 53

5 – 4 Intensity distribution acsross the diameter of focal spot. 54

5 – 5 Time integrated two-dimensional image of the focal spot intensity distribution... 55

5 – 6 Experimental arrangement for the laser energy absorption measurement. 578

5 – 7 (A) Faraday cup electrical connections. (B) Oscilloscope display of a Faraday cup signal. 59

5 – 8 (A) Schematic of a differential calorimeter. (B) Oscilloscope display of a differential calorimeter signal. 61

5 – 9 Experimental set-up used in the X-ray film calibration technique. 65

5 – 10 Silicon X-ray spectrum obtained with a three-channel step-wedge filter. 66

5 – 11 Silicon spectrum transmitted through different filters..... 68

5 – 12 Film transmission (%) for the four silicon lines used. 70

5 – 13 Relative intensity calibration curve obtained with silicon spectrum. 71

5 – 14 Intensity of a group of silicon lines as a function of CH thickness..... 73

5 – 15 Aluminum X-ray spectrum obtained with a four-channel step-wedge filter. 76

5 – 16 Film transmission (%) for each channel for the six aluminum lines used. 77

5 – 17 Relative intensity calibration curve obtained with an aluminum spectrum. 78

5 – 18 X-ray pinhole photograph of plasma. 80

5 – 19 X-ray pinhole photograph of plasma. 81

5 – 20 Series of X-ray pinhole photographs obtained by irradiating thin strip of aluminum foils of different thicknesses..... 82

5 – 21 (A) Schematic diagram of the electron temperature monitor. (B) Theoretical X-ray response of the Reticon array. 85

5 – 22 (A) Block diagram of synchronization circuit. (B) Timing sequence of synchronization circuit..... 86

5 – 23 (A) Relative response of diode elements of the Reticon array. (B) Output waveform for a nine-channel electron temperature monitor. 88

5 – 24 Linearity of response of the Reticon detector 89

5 – 25 Experimental arrangement used in the fabrication of CH-multilayer targets 92

6 – 1 Absorption fraction as a function of the laser intensity for different laser wavelengths. 94

6 – 2 Relative intensity of X-ray continuum transmitted through different filters. 97

6 – 3 Scaling of electron temperature as a function of laser intensity for 0.532 μm radiation. 98

6 – 4 X-ray continuum spectrum for 0.532 μm radiation. 100

6 – 5 X-ray continuum for 0.266 μm radiation. 101

6 – 6 Brillouin reflectivity as a function of incident laser intensity for 0.532 μm radiation. 104

6 – 7 $\frac{3}{2}w_L$ backscatter reflectivity as a function of laser intensity for 0.532 μm radiation 105

7 – 1 Experimental arrangement for energy transport measurement 108

7 – 2 Silicon line spectrum. 109

7 – 3 Intensity of the silicon line group between 6.65 and 6.74 Å as function of CH layer thickness 112

7 – 4 Intensity of the silicon line group between 6.65 and 6.74 Å as function of Sn layer thickness 113

7 – 5 Intensity of the silicon line group between 6.65 and 6.74 Å as function of Ag layer thickness 114

7 – 6 Intensity of the Si XIII $1s^2(^1S_0) - 1s2p(^1P_1)$ line as a function of Mg layer thickness. 115

7 – 7 Intensity of the Si XIII $1s^2(^1S_0) - 1s2p(^1P_1)$ line as a function of Au layer thickness. 116

7 – 8 Laser penetration depth as a function of target density. 117

7 – 9 Schematic showing the hydrodynamic shearing of the target layer. 119

8 – 1 Experimental arrangement to measure energy and velocity of the expanding plasma. 119

8 – 2 Energy and velocity distribution of the expanding plasma. 125

8 – 3 Mass ablation rate as a function of absorbed flux for 0.532, 0.355 and 0.266 μm laser light. 127

8 – 4 Ablation pressure as a function of absorbed flux for 0.532, 0.355 and 0.266 μm laser light. 128

8 – 5 Wavelength dependence of mass ablation rate at absorbed irradiances of $2.6 \times 10^{12}, 6.6 \times 10^{12}$ and 10^{13} W/cm^2. 120

8 – 6 Wavelength dependence of ablation pressure at absorbed irradiances of $2.6 \times 10^{12}, 6 \times 10^{12}$ and 10^{13} W/cm^2. 130

List of Tables

2 – 1 Partial list of the instabilities which can be driven by laser light propagating in a plasma 20

5 – 1 List of the foils used for three channel step-wedge filter 64

5 – 2 List of the silicon lines used for constructing the calibration curve and the transmission factors through different channels 69

5 – 3 List of foils used for four-channel step-wedge filter 74

5 – 4 List of aluminum lines used for constructing the calibration curve and their transmission factors through the different channels 75

5 – 5 X-ray filters for various channels of the electron temperature monitor 87

Acnowledgements

I wish to thank my supervisor Dr. Andrew Ng for proposing the experiment and for his help and guidance throughout this work. His deep involvement, dedication and undeterred enthousiasm were most appreciated.

This was also an opportunity for me to work in fruitful collaboration with other people. I wish to express my deep appreciation to Peter Celliers, Luiz Da Silva, Joe Kwan and Dean Parfeniuk for their assistance and frienship. Their presence made the work much more satisfying and pleasant.

Dr. Sidney Kastner read the manuscript of this thesis as it was written. I want to thank him for his corrections and suggestions. This led to several interesting and valuable discussions.

Thanks are due to the members of my supervisory committee: Dr. A.J. Barnard, Dr. F.L. Curzon, Dr. D.S. Beder and Dr. H.P. Gush.

It has been a pleasure to be associated with the friendly and stimulating people comprising the plasma physics group at UBC. In particular I have had many usefull discussions with John Bernard, Hubert Houtman and Roman Popil. Also, the technical assistance of Allan Cheuck was greatly appreciated.

Chapter 1

Introduction

1–1 Introduction to controlled thermonuclear fusion

For the past thirty years there has been intense research towards controlled thermonuclear fusion. The easiest fusion reaction to initiate is:

$$D + T \longrightarrow {}^4He(3.5\ MeV) + n(14.1\ MeV) \quad ,$$

where a deuterium nucleus fuses with a tritium nucleus to produce an α particle and a neutron. The energy release when such a reaction takes place is in the form of the kinetic energy of the reaction products. This energy can then be recovered in a heat cycle. The difficulty in attaining the fusion reaction is to have the deuterium and tritium nuclei collide with sufficient energy to overcome their repulsive Coulomb potential barrier. One way to achieve this is to heat up the reacting nuclei in a plasma to a temperature of approximately 10^8 K. As only a small fraction of the collisions between the nuclei leads to fusion events, the high temperature fusion fuel , must be held together long enough for sufficient fusion reactions to occur.

Therefore to achieve thermonuclear fusion two problems must be solved: (1) production and heating of a plasma to thermonuclear temperatures, and (2) confinement of the reacting plasma to produce a positive energy yield, that is, more energy generated than expended in the heating and confinement of the fuel. These two requirements impose a condition on the plasma density n , the confinement time τ and the plasma temperature T. This condition is usually expressed through the Lawson[1] criterion which reflects the balance between the input energy to the plasma, the thermonuclear energy production, the plasma radiation losses and recovery of the thermonuclear and radiation energy through

a thermal cycle with an efficiency of 33 %. The Lawson criterion for the D-T reaction at T$\approx 10^8$ K requires that $n\tau > 10^{14}$ cm^{-3} s for "break-even".

Two different approaches have been investigated to confine the plasma. In the magnetic confinement scheme, the attempt is to confine the plasma (at $n \sim 10^{14} - 10^{15}$ cm^{-3}) for relatively long time ($\tau \sim 0.1 - 1$ s) in a suitably shaped magnetic field. This method is on the threshold of achieving "break-even". In the inertial confinement approach, the objective is to compress the fuel to very high densities ($\approx 10^{26}$ cm^{-3}) and heat it to thermonuclear temperatures extremely rapidly ($\approx$ 100 ps) so that appreciable thermonuclear reaction energy will be produced before the fuel disintegrates by rapid expansion. This could be achieved, in principle, by focussing an intense laser beam (or beam of charged particles) onto small deuterium-tritium spherical pellets. This approach will now be discused further in order to introduce laser-matter interaction studies described in this thesis.

1-2 Basic concept of laser fusion

To satisfy the Lawson criterion with practical laser energy ($<$ 1 MJ) the deuterium-tritium fuel must be compressed to 10,000 times its liquid density[2]. Fuel compression to such extremely high densities may be achieved by laser-driven implosion of spherical fuel pellets as schematically represented in Figure 1 – 1. The pellet containing deuterium-tritium fuel is uniformly irradiated with intense laser light ($\sim 10^{13} - 10^{15}$ W/cm^2). The laser energy is absorbed in the outer atmosphere of low density plasma, produced by the vaporization of material at the pellet surface. The energy is then carried inward by electron thermal conduction. This heat flux causes ablation of the target material and the resulting hot, dense plasma rapidly expands outward. The recoil momentum generates a strong pressure wave which propagates inwards, accelerating and compressing the material behind it. Consequently, the shock-compressed outer shell begins to implode. When the imploding shell stagnates at the center of the pellet, its kinetic energy is transformed into heat, initiating a thermonuclear burn. The thermonuclear burn front then propagates outward, burning the compressed fuel to depletion before it disassembles.

Using this simplified picture, the interaction physics leading to thermonuclear burn can be categorized according to the various processes involved:

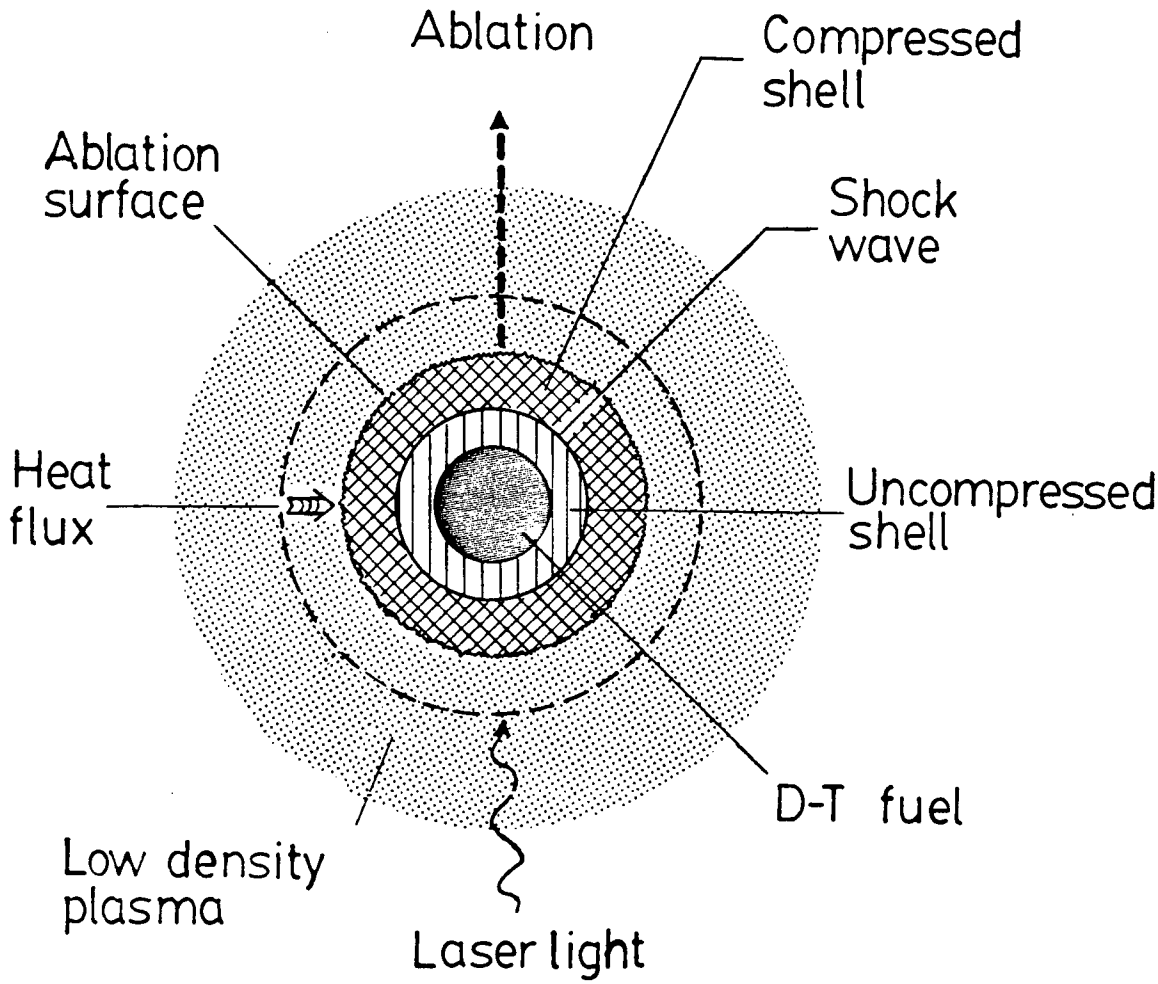

Figure 1-1 Schematic of laser-driven implosion of a pellet containing deuterium-tritium fuel.

(i) absorption of laser energy in the low density plasma,

(ii) transport of energy by electron thermal conduction from the absorption region to the target surface,

(iii) compression of the target material by the ablation process, and

(iv) ignition and nuclear burn.

1-3 Recent developments in laser-matter interaction studies

Present lasers lack the energy required to both compress and heat the fuel mass sufficiently to produce large thermonuclear energy yields. Experiments to date[3] have only produced yields approximately 3×10^{-6} the input laser energy. To optimize the design of fusion targets and determine the characteristics of future fusion drivers a detailed understanding of laser-matter interaction is most vital.

Until a few years ago experiments in laser fusion were done using almost exclusively 1.06 μm radiation from a Nd-glass laser or the 10.6 μm radiation from a CO_2 laser. Two particularly challenging problems for laser fusion were identified in these experiments[3]. Firstly at high laser intensities (especially at 10.6 μm) a large fraction of the absorbed energy was coupled to very energetic electrons. Because of their long range for energy deposition in the target, these "hot"electrons would heat the core of the fuel pellet before it was compressed, that is, preheating the fuel. Much larger laser energy would then be needed to compress the fuel to the required density. Secondly energy transport by electron thermal conduction was found to be much less than theoretically calculated. As a result much higher laser energy than previously assumed would be necessary to achieve the required compression.

Short-wavelength lasers offer several possible advantages over long-wavelength lasers[2,4]. At short wavelengths classical collisional absorption is more effective, and this should lead to higher absorption efficiency. Deposition of the laser energy also occurs at higher plasma densities, leading to higher mass ablation rate and ablation pressure. Furthermore most of the collective laser-plasma interaction processes which lead to scattering of the incoming laser light and which are responsible for the production of hot electrons, will be mitigated because of the higher laser intensity thresholds required at shorter wavelengths.

Experiments performed at Ecole Polytechnique[54] (1980) were the first to demonstrate increased laser absorption, higher mass ablation rate, and reduced hot electron energies when using sub-micron wavelength laser radiation. These preliminary results sparked an increasing interest in the use of short-wavelengths for target irradiation. The process of laser-driven ablation in particular received considerable attention and analytical models predicting the scaling of the mass ablation rate and ablation pressure with laser irradiance and wavelength were proposed[55–57]. At the same time many laboratories[5–15,58] including our own intiated intense investigations specifically to study the effect of the laser wavelength in laser-matter interactions.

1-4 Present investigation

The main objective of this work was to study the effect of the laser wavelength in laser-matter interactions for sub-micron laser light. Specifically the physics issues that we adressed in our work were:

1. coupling of laser energy to the target plasma,

2. energy transport from the absorption region to the high density target interior by electron thermal conduction and

3. dependence of the mass ablation rate and ablation pressure on laser intensity and wavelength.

For this work we have used sub-micron laser wavelengths (0.532, 0.355 and 0.266 μm) at moderate irradiances ($10^{12} - 5 \times 10^{13}$ W/cm^2) and with long pulse length (2ns FWHM). To allow a clear comparative study of the effect of the laser wavelength, identical irradiation conditions were used for each laser wavelength. For this short wavelength and relatively low intensity regime, it is expected that classical collisional absorption is the dominant absorption mechanism and laser-plasma collective processes should not be important. Therefore the production of hot electrons should be kept to a minimum and energy transport into dense matter should be mainly through classical electron thermal conduction. Also using long laser pulses the plasma flow from the target suface should reach a steady-state. Thus the results should provide in principle a valid comparison with predictions from classical, steady-state theories.

Related works studying the dependence of the mass ablation rate and ablation pressure on laser wavelength and intensity has been carried out concurrently at other laboratories. In the work of Fabro et al.[68], the mass ablation rates have been determined for 1.06, 0.53 and 0.26 μm laser irradiation of thin foils. The results were based on a limited number of data points obtained over a wide range of laser intensities and pulse lengths. Collective plasma processes which become important at high irradiances (10^{15} W/cm^2) and long wavelengths (1.06 μm) may affect the overall wavelength dependence of the ablation rate. Also, the ablation process will reach steady-state conditions only for the long pulse ($\geq$ 1ns) experiments. Key et al.[14] obtained both wavelength and intensity scaling laws for the mass ablation rate and ablation pressure using 1.06, 0.53 and 0.35 μm laser radiation. The laser intensity on target was varied by changing the focal spot sizes. The results appeared to be dominated by significant lateral energy transport out of the focal spot area, particularly for the longer wavelength radiation. Most recently, Meyer and Thiell[15] have measured the total ablated mass in planar targets irradiated with 1.05 and 0.35 μm laser light. Again, lateral energy transport in the longer wavelength measurement made wavelength scaling comparisons difficult. In our work, using identical laser focal spot sizes and pulse lengths, moderate irradiances and sub-micron wavelength laser radiation, the effect of collective plasma processes and lateral energy transport on the scaling studies were minimized.

1-5 Thesis outline

Chapters 2, 3 and 4 present a theoretical background on laser-plasma coupling, electron thermal transport and steady-state ablation. Estimates of the importance of the different physical mechanisms will be made for typical conditions in our work. In Chapter 5 we describe our experimental set-up, the experimental conditions and the different diagnostics which have been used. The experimental results and their interpretations are presented in Chapter 6, 7 and 8. Finally in Chapter 9 we summarize the results and conclusions of our work, highlight the original contributions and give suggestions for future work.

Chapter 2

Absorption of laser light in a laser produced plasma

In this chapter we describe the principal mechanisms through which laser light can interact with a plasma and which lead to absorption and/or scattering of the radiation. This will constitute a general background for the interpretation of our measurements on the coupling of the laser energy to the target, that we present in Chapter 6. First let us introduce some basic properties which characterize laser light propagation in a plasma.

The laser radiation is considered as a plane wave described by a transverse electric field

$$\mathbf{E} = \mathbf{E}_0 \exp i(w_L t - \mathbf{k}_L \cdot \mathbf{r})$$

where w_L and $\mathbf{k}_L$ are the frequency and wave number of the laser light in the plasma. The propagation of laser light in a plasma will be governed by its dispersion relation[16] :

$$\frac{k_L^2 c^2}{w_L^2} = \epsilon \simeq 1 - \frac{w_p^2}{w_L^2} + i\left(\frac{\nu_{ei}}{w_L}\right)\left(\frac{w_p^2}{w_L^2}\right) \qquad (2-1)$$

where ϵ is the plasma dielectric constant, ν_{ei} is the electron-ion collision frequency which leads to a damping for the incident laser light, c is the velocity of light in free space and w_p is the "plasma frequency" which is the natural frequency of oscillation of the electrons in a plasma, given by :

$$w_p = \left(\frac{n_e e^2}{m_e \epsilon_0}\right)^{1/2} \qquad (2-2)$$

where n_e represents the plasma electron density, e and m_e the electric charge and mass of an electron respectively and ϵ_0 the permitivity of free space. The plasma frequency depends on the electron density. Thus as laser light propagates from lower to higher density in a plasma its wave number as given by (2−1) becomes smaller. Finally at the "critical density" the plasma frequency w_p becomes equal to the laser light frequency w_L and the laser light

can no longer propagate ; for $n_e > n_{cr}$ the wave number becomes purely imaginary and the light wave is evanescent. Thus the critical density

$$n_{cr} = \frac{m_e \epsilon_0 w_L^2}{e^2} \quad \Longleftrightarrow \quad n_{cr} = \frac{1.1 \times 10^{21}}{\lambda_L^2(\mu\mathrm{m})} \quad (\mathrm{cm}^{-3}) \qquad (2-3)$$

is the reflection point for laser light of wavelength λ_L in a plasma.

Figure $2-1$ shows a schematic of the electron density profile in the expanding or "blow-off" plasma of a laser irradiated solid. It also identifies different processes through which laser light interacts with the plasma. Since the laser radiation cannot penetrate to densities above n_{cr} all laser light absorption and reflection processes occur at electron densities $n_e < n_{cr}$, that is, in the so called underdense plasma.

In section $2-1$ we will discuss inverse bremsstrahlung absorption where the electrons oscillate in the electric field of the laser light and by colliding with ions convert their coherent energy of oscillation into random thermal energy. The laser light can also excite plasma waves which in turn can heat the plasma or scatter the incident laser radiation. (There are two plasma waves of interest in an unmagnetized plasma ; the first is a high frequency electron plasma wave which occurs at the natural frequency with which electron oscillates, the second is a low frequency ion acoustic wave which is the analog of a sound wave in a ordinary gas). In particular in section $2-2$, we will describe a process known as "resonance absorption" where the electric field of the laser light resonantly excites electron plasma waves (Langmuir waves) at the critical density surface. In section $2-3$ we will discuss laser driven plasma instabilities . These processes which includes the parametric instability, the two-plasmon decay instability, the Raman and Brillouin scattering instabilities lead to the excitation of plasma waves and can occur throughout the underdense plasma as shown in Figure $2-1$.

2–1 Inverse bremsstrahlung absorption

The main absorption mechanism for laser light in a plasma is inverse bremsstrahlung or collisional absorption. We recall that bremsstrahlung radiation is emitted when a free electron is accelerated in collision with an ion. The reverse process is also possible where radiation is absorbed by accelerating an electron in the field of an ion (the presence of an

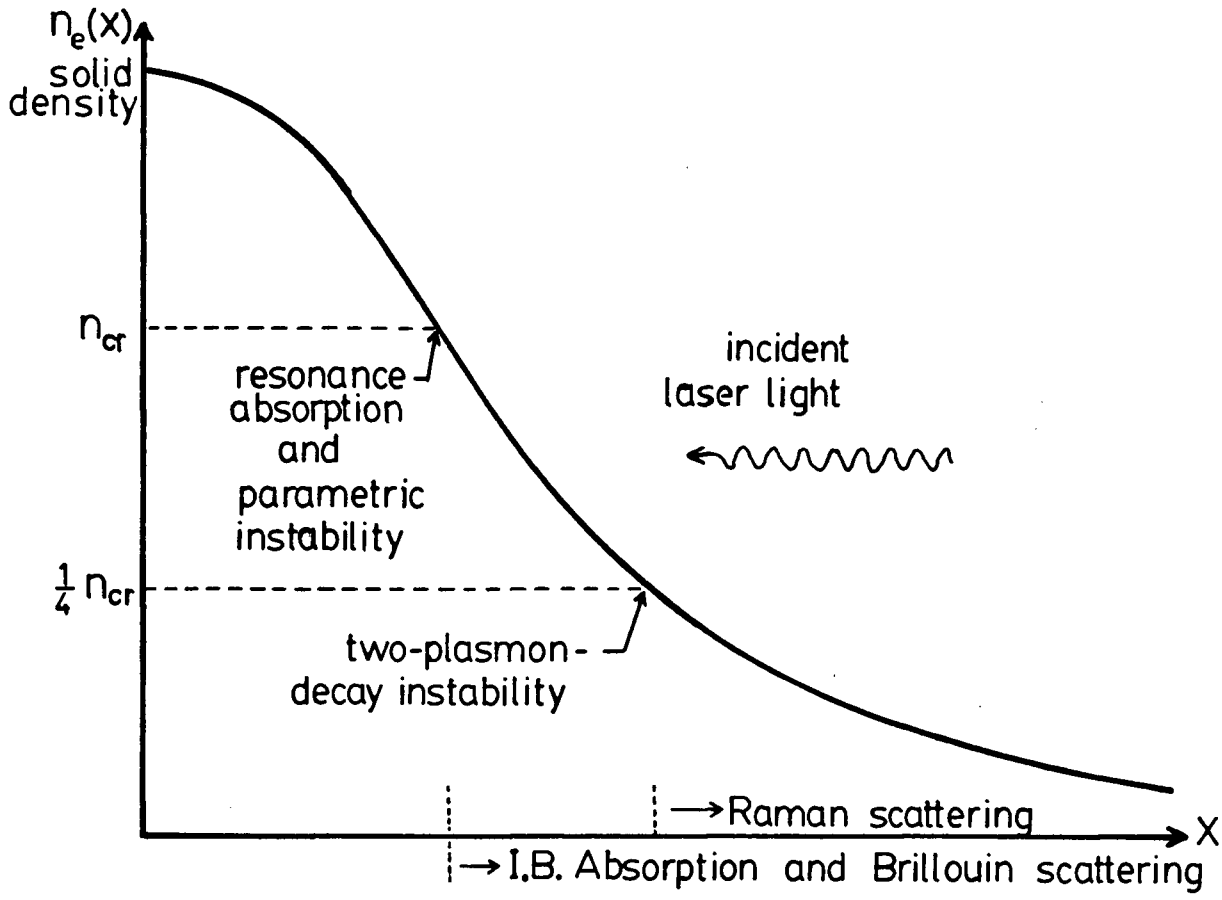

Figure 2–1 Schematic picture of electron density profile in a laser-produced plasma, showing locations of major coupling processes.

ion is necessary to conserve momentum). Let us consider the motion of an electron in the oscillating electric field of an incident electromagnetic wave (the incident laser light). As the electron oscillates in this field, it collides with the ions, thereby converting its coherent energy of oscillation into random thermal energy. In other words, the incident laser light drives electron currents and the resistivity represented by electron-ion collisions leads to a heating of the plasma. This implies a spatial attenuation of the incident wave as it propagates in the plasma, a process that we will now analyse in more detail.

In describing the spatial attenuation of an electromagnetic wave in a plasma, the parameter normally used is the "linear absorption coefficient". It is defined in terms of the laser light intensity I_{w_L}. For a wave travelling in the z direction, $I_{w_L} = I_{0,w_L} \exp -(a_{w_L} z)$. Since the intensity I_{w_L} is proportional to the square of the electric field $\mathbf{E} = \mathbf{E}_0 \exp i(w_L t - k_L z)$, we have :

$$a_{w_L} = -2Im(k_L) \quad . \tag{2-4}$$

The imaginary part of k_L is obtained by solving equation $(2-1)$ from which we find :

$$a_{w_L} = \left(\frac{\nu_{ei}}{c}\right)\left(\frac{w_p^2}{w_L^2}\right)\frac{1}{(1 - w_p^2/w_L^2)^{1/2}} \quad . \tag{2-5}$$

By using the appropriate expression for the electron-ion collision frequency ν_{ei} the following expression for the absorption coefficient is finally obtained[17-18] for a Maxwellian velocity distribution

$$a_{w_L} = \frac{< Z > n_e^2 e^6 \ln \Lambda}{3\epsilon_0^3 c (2\pi m_e k T_e)^{3/2} w_L^2} \frac{1}{(1 - w_p^2/w_L^2)^{1/2}} \quad \text{(SI units)} \quad , \tag{2-6}$$

where $< Z >$ is the average ion charge, T_e the electron temperature, k the Boltzmann constant, $\ln \Lambda$ the Coulomb logarithm. Λ is the ratio of the maximum and minimum distance through which an electron interacts with an ion. It is given by :

$$\Lambda = \lambda_D / d_{min} \quad ,$$

where $\lambda_D = \left(\frac{\epsilon_0 k T_e}{n_e e^2}\right)^{1/2}$ and $d_{min} \equiv \text{Max}\left[\frac{1}{2\pi\epsilon_0}\frac{Ze^2}{kT_e} \; , \; \frac{h}{2\pi m_e^{1/2}(kT_e)^{1/2}}\right]$.

Thus,

$$\ln\Lambda = \mathrm{Min}[\ln(2.58\times10^{9}\frac{T_e^{3/2}}{Zn_e^{1/2}})\ ,\ \ln(2.83\times10^{10}\frac{T_e}{n_e^{1/2}})] \qquad (2-7)$$

where the units of T_e and n_e are in eV and cm^{-3} respectively. Equation $(2-6)$ shows that inverse bremsstrahlung is strongest for low-temperature, high-density and high-Z plasmas. For the absorption of laser light in a density gradient it is convenient to rewrite equation $(2-6)$ as :

$$a_{w_L} = \eta\frac{Z\ln\Lambda}{T_e^{3/2}\lambda_L^2}(\frac{n_e}{n_{cr}})^2(1-\frac{n_e}{n_{cr}})^{-1/2} \quad , \qquad (2-8)$$

$$\text{where} \qquad \eta = \frac{(2\pi)^{1/2}}{3}\frac{m_e^{1/2}c^2e^2}{\epsilon_0 k^{3/2}} \quad .$$

Let us consider a plasma with an exponential density profile

$$n_e = n_{cr}\exp-(\frac{x}{L}) \quad , \qquad (2-9)$$

where L is the density gradient scale length, and calculate the absorption for a laser beam propagating at normal incidence to this gradient. The absorption fraction up to the density $n_e = \beta n_{cr}$ (where β is a number less or equal to 1) is given by :

$$A(\beta n_{cr}) = 1-\exp-\Big(\int_{n_e=0}^{n_e=\beta n_{cr}} a_{w_L}(x)\,dx\Big) \qquad (2-10)$$

Substituting equations $(2-8)$ and $(2-9)$ in this equation yields :

$$A(\beta n_{cr}) = 1-\exp\Big(-\frac{\eta Z\ln\Lambda}{T_e^{3/2}\lambda_L^2}\int_{+\infty}^{-L\ln\beta}\exp-\frac{2x}{L}(1-\exp\frac{-x}{L})^{-1/2}\,dx\Big) \qquad (2-11)$$

The integral is easily evaluated to give :

$$A(\beta n_{cr}) = 1-\exp-[\frac{4}{3}\frac{\eta\,Z\,L\ln\Lambda}{T_e^{3/2}\lambda_L^2}F(\beta)] \qquad (2-12)$$

$$\text{where} \qquad F(\beta) = 1-(1-\beta)^{1/2}(\frac{\beta}{2}+1)$$

or in practical units

$$A(\beta n_{cr}) = 1 - \exp -[15.33 \frac{Z \ln \Lambda \, L(\mu m)}{\lambda_L^2(\mu m) T_e^{3/2}(eV)} F(\beta)] \qquad (2-13)$$

This expression shows that inverse bremsstrahlung absorption in an exponential density profile is stronger for low temperature (low laser intensity), large scale length, high Z material, short laser wavelength and high electron densities (the function $F(\beta)$ increases rapidly with $\beta = n_e/n_{cr}$). Figure $2-2$ shows the evolution of the percentage absorption of laser radiation of different wavelengths as it penetrates an exponential density profile. This calculation was done for typical conditions encountered in our experiments namely : $Z \simeq 11$ (using aluminum targets), $L = 80\,\mu$m (determined by our laser focal spot according to equation $(4-35)$ of chapter 4) and plasma temperatures of 500 eV at 0.532 μm, 390 eV at 0.355 μm, 330 eV μm at 0.265 μm (according to formula $(4-36)$ of chapter 4 for an incident irradiance of 10^{13} W/cm^2, which yields good agreement with our experimental measurements of plasma temperature). The Coulomb logarithm was calculated using equation $(2-7)$ for the critical density value at each laser wavelength. Our simple calculation shows that the absorption coefficient is so high for these experimental conditions that in fact most of the laser energy will be deposited before reaching the critical density. This last point will have an important consequence on the scaling of the plasma parameters with laser intensity and wavelength as will shall see in chapter 4.

For high laser fluxes the non-linear processes can reduce the effectiveness of collisional absorption. In one effect, discussed by Silin[19], the electron collision frequency is modified by the coherent oscillation of the electrons in the laser electric field. Thus rather than having only a thermal velocity $V_{te} = (kT_e/m_e)^{1/2}$ the electrons have an effective velocity V_{eff} given by :

$$V_{eff}^2 = V_{te}^2 + V_{osc}^2 \quad , \qquad (2-14)$$

$$\text{where} \qquad V_{osc} = \frac{eE_L}{m_e w_L} \qquad (2-15)$$

is the oscillatory velocity of an electron in the electric field E_L of the laser light. Because the absorption coefficient a_{w_L} scales as $T_e^{-3/2} \propto V_{eff}^{-3}$, $(2-8)$ the absorption coefficient becomes

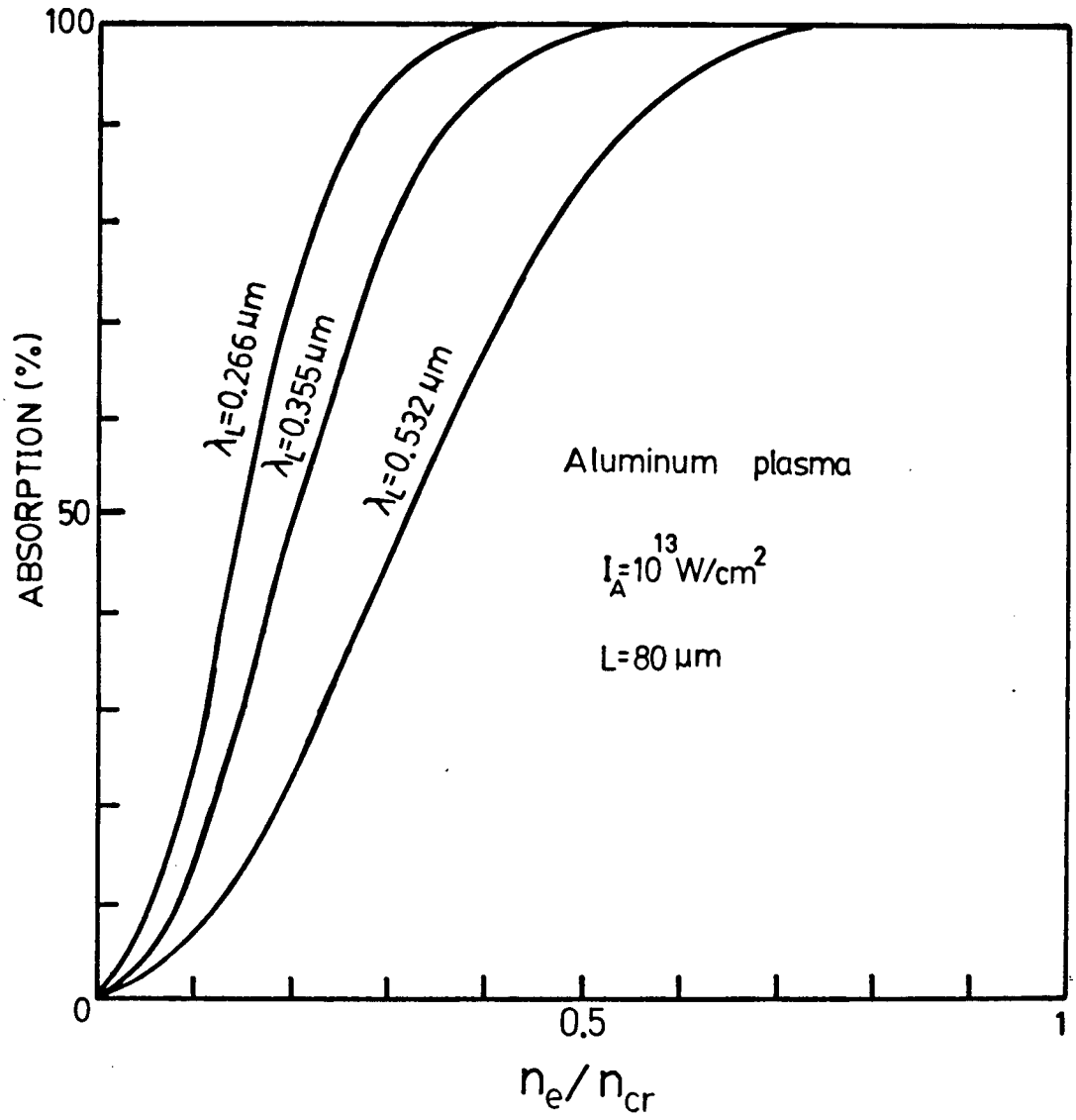

Figure 2–2 Percentage absorption of laser energy in an exponential plasma density profile for different laser wavelengths.

$$a_{w_L}(non\,linear) \rightarrow \frac{a_{w_L}(linear)}{1+\frac{3}{2}(eE_L/(m_e w_L V_{te}))^2} \qquad (2-16)$$

at high laser intensities.

Another non-linear effect, discussed more recently by Langdon[20] is due to the fact that for high laser intensity the electron velocity distribution can be far from Maxwellian. This will occur when the rate of laser energy absorption by the electrons becomes larger than the relaxation rate of the electron distribution towards a Maxwellian, a condition which can be expressed as :

$$\nu_{ei}V_{osc}^2 > \nu_{ee}V_{te}^2 \quad \Longleftrightarrow \quad Z(\frac{eE_L}{m_e\, w_L\, V_{te}})^2 > 1 \qquad (2-17)$$

where ν_{ei} is the electron-ion collision frequency and $\nu_{ee}(\sim \nu_{ei}/Z)$ the electron-electron collision frequency. It is those electrons with electron-ion collision frequency $\nu_{ei}(V)$ close to the laser frequency w_L that contribute most to the absorption process. Because $\nu_{ei}(V)\ \alpha\ V^{-3}$ and since generally $\nu_{ei}(V_{te}) << w_L$, the electrons responsible for absorption have relatively low velocity compare to V_{te}. However when equation $(2-17)$ is satisfied (for high laser intensities), the electron distribution becomes distorted and has relatively less low velocity electrons than in a Maxwellian distribution. For this non-Maxwellian velocity distribution the amount of absorption is reduced by a up to a factor of two compared to what is predicted with the Maxwellian distribution usually assumed (eq. $2-6$).

The relevant parameter in these two non-linear processes is V_{osc}^2/V_{te}^2 . This ratio may be expressed as $V_{osc}^2/V_{te}^2 = 4\times10^{-16}I_L\lambda_L^2/T_e$ where I_L is the intensity in W/cm^2, λ_L is the laser wavelength in μm and T_e is the electron temperature in keV. Typical conditions in our experiments are $I_L = 10^{13}$ W/cm^2, $\lambda_L = 0.532\,\mu$m, $Z = 11$ and $T_e = 500$ eV. For these values $V_{osc}^2/V_{te}^2 \approx 2\times10^{-3} << 1$. Therefore non-linear effects will not be important in the inverse bremsstrahlung absorption process in our experiment.

2-2 Resonance absorption

Resonance absorption[21–23] is the simplest absorption process via electron plasma wave. Consider 'p' polarized ($\mathbf{E}_L$ vector parallel to the plane of incidence) laser light

obliquely incident on a plasma with a density gradient ∇n_e. The component of the laser electric field $\mathbf{E}_L$ parallel to the density gradient produces a charge separation and drives a charge density fluctuation δn_e at the laser frequency w_L. At the critical density surface, this driven fluctuation is at the plasma frequency ($w_L = w_p$) and an electron plasma wave is resonantly excited. The laser energy is thus transferred to the electron plasma waves. The damping of these waves then completes the energy transfer to the thermal energy of the plasma.

Figure $2-3$ illustrates this process in more detail. For light incident on a plasma density gradient at an angle θ to the normal, Snell's law and the dispersion relation $(2-1)$ can be combined to show[23] that the the classical turning point for the light wave occurs at a density $n_e(\theta) = n_{cr}\cos\theta$. Beyond this point, the wave is evanescent. However, if the electric field vector of the wave is in the direction of the density gradient, part of this field can penetrate through to the critical-surface region where it can resonantly drive electron plasma waves. We can show[24] this rather easily from Maxwell's equations which can be written as

$$\nabla\cdot[\epsilon(x)\mathbf{E}] = 0 \quad , \tag{2-19}$$

$$\text{where} \quad \epsilon(x) = 1 - \frac{w_p^2(x)}{w_L^2} \qquad [\text{see eq. } (2-1)] \quad . \tag{2-20}$$

Expanding this we get

$$\epsilon(x)\nabla\cdot\mathbf{E} + (\mathbf{E}\cdot\nabla)\epsilon(x) = 0 \quad . \tag{2-21}$$

Now, from Poisson's equation we have

$$\nabla\cdot\mathbf{E} = -\frac{e\,\delta n_e}{\epsilon_0} \quad , \tag{2-22}$$

where δn_e is the electron density perturbation. Since $\nabla\epsilon(x) \;\; \alpha \;\; \nabla n_e$, comparison with $(2-21)$ gives

$$\frac{e\,\delta n_e}{\epsilon_0} \;\; \alpha \;\; \frac{\mathbf{E}\cdot\nabla n_e}{\epsilon(x)} \tag{2-23}$$

This simple result illustrates the two main characteristics of resonant absorption: the density perturbations are only excited by a light wave with a component of its electric field

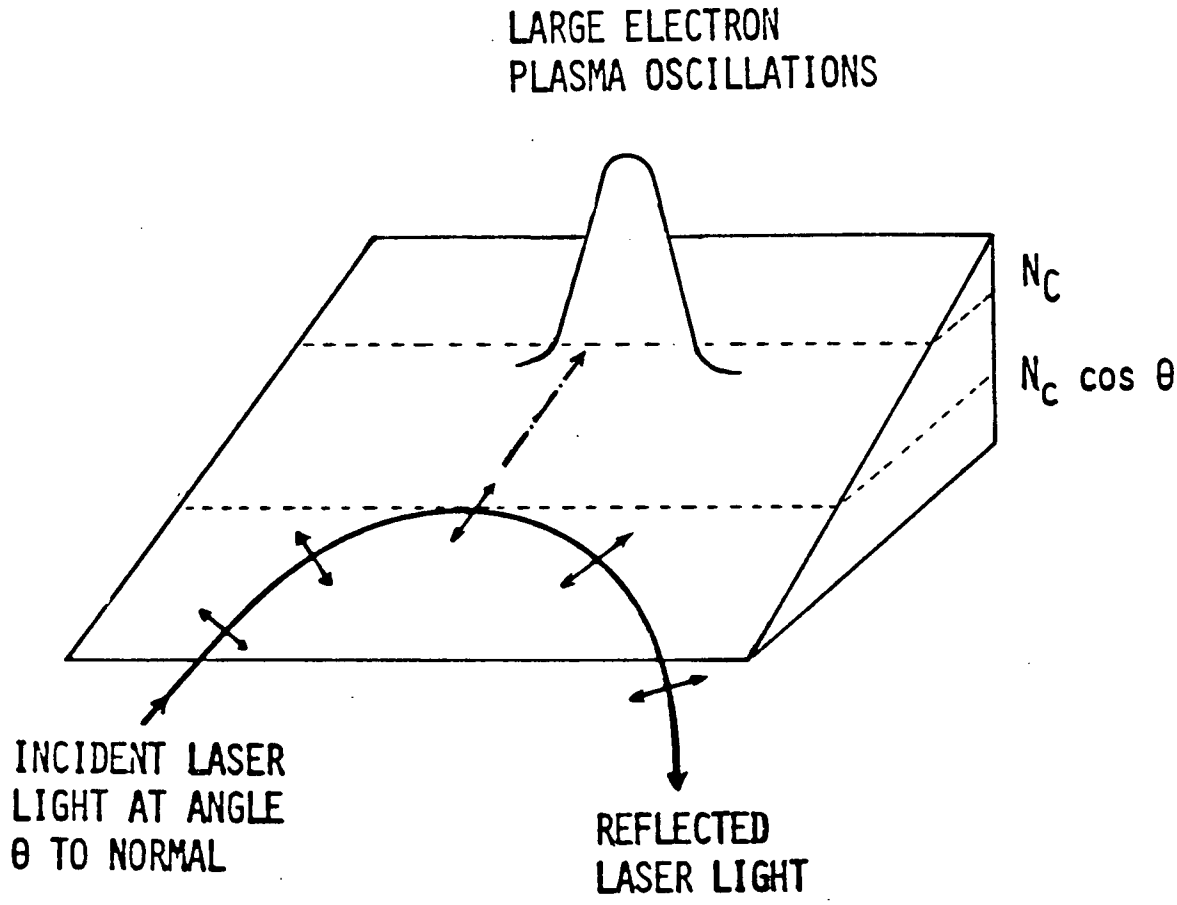

Figure 2–3 Schematic representation of resonance absorption for 'p' polarized laser light obliquely incident on a plasma density gradient.

in the direction of the density gradient, and these perturbations are resonantly excited only for $\epsilon \approx 0$, that is, where $w_L = w_p$.

The actual amount of absorption for 'p' polarized light will depend on the angle of incidence θ (Fig. $2-3$). For small θ the electric field is almost parallel to surfaces of constant electron density and the resulting density fluctuation is small. For large θ, the cut-off and the resonance regions are widely separated and the driving electric field is greatly attenuated in the evanescent region. The absorption fraction maximizes at about 60 % for an angle θ which satisfies

$$\sin\theta \simeq 0.8(\frac{\lambda_L}{2\pi L})^{1/3} \qquad (2-24)$$

where c is the speed of light in vacuum and L the density gradient scale length.

Computer simulations of resonance absorption[25–28] show collisionless heating of electrons traveling through the resonant electron plasma waves from high densities towards low densities. Electrons with a velocity close to the phase velocity of a wave see nearly a constant electric field. A large energy transfer then occurs as the electrons are efficiently accelerated by the wave. Hence, faster electrons are preferentially heated, which leads to a heated velocity distribution characterized by an energetic tail. This velocity distribution can be described using a two-temperature Maxwellian distribution. The lower energy thermal electrons are characterized by a temperature T_{cold} and the very energetic resonantly heated electrons by a temperature T_{hot}. The average temperature T_{hot} has been estimated to be[27]

$$T_{hot} = T_{cold} + 4.3 \times 10^{-6} T_{cold}^{0.04} (I_L[\lambda_L/1.06]^2)^{0.42} \qquad (2-25)$$

where the units for T, I_L and λ_L are keV, W/cm^2 and μm respectively.

Computer simulations have also shown the importance of plasma density profile-steepening in resonance absorption. This steepening can be due to the ponderomotive force (light pressure in a plasma[29]), but the dominant force is frequently due to the resonant plasma waves which accelerate hot electrons down the density gradient during resonance absorption[28]. To balance the momentum they carry away, the density profile adjusts near critical and steepens there. Such profile steepening then makes resonance absorption more

effective as it is less sensitive to the angle of incidence because there is now less distance to penetrate to reach the critical density surface. In addition, laser-driven plasma instabilities near the critical surface (discussed in the next section) are strongly limited since there is only a very small region of plasma in which these instabilities can operate.

Resonance absorption will be the dominant absorption mechanism for high plasma temperature (high laser intensity), long laser wavelength and short plasma scale-length, that is, under conditions for which inverse bremsstrahlung absorption is inefficient and for which most of the laser radiation reaches the critical density surface. Evidently with very strong inverse bremsstrahlung absorption, resonance absorption is not expected to be important in our experiment.

2–3 Absorptive and scattering instabilities

At high intensities the laser light can excite natural modes of oscillation of the plasma (electron plasma wave and ion acoustic wave) by laser-driven plasma instabilities[30]. These waves in turn can lead to absorption or scattering of the incident laser light.

As an example the stimulated Brillouin scattering instability will be described. The feedback loop leading to instability is illustrated in Figure $2-4$. Consider a small density fluctuation δn associated with an ion acoustic wave. The electric field E_L couple with the density fluctuation δn and produces a transverse current $\alpha\ \delta n E_L$, due to the oscillatory motion of electrons in the laser electric field. This transverse current produces a reflected light wave with field E_R. The ponderomotive force $\nabla(E_L E_R/8\pi)$ of the incident and reflected light waves in turn enhances the density fluctuation. If such enhancement in δn exceeds its damping losses, the process becomes unstable. In this case, it will lead to exponential growth of both the ion acoustic wave and the scattered light wave.

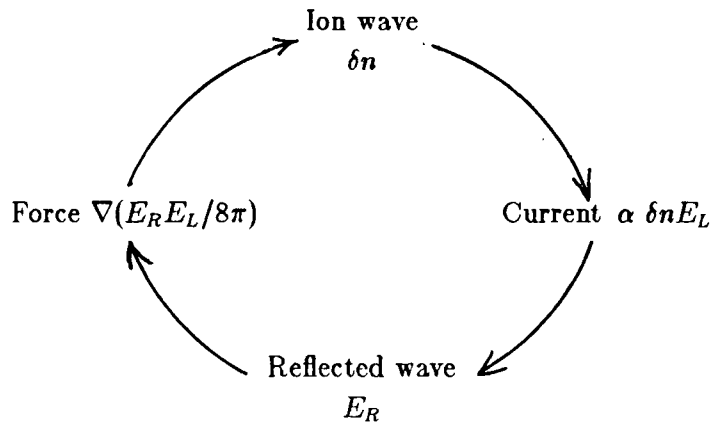

Figure 2–4 Feedback mechanism for growth of stimulated Brillouin scattering

Most of the laser-driven plasma instabilities can be described as the resonant decay of an electromagnetic wave into two other waves. The parametric-decay instability represents the decay of the incident light wave (w_L , k_L) into an ion-acoustic wave (w_{ia} , k_{ia}) plus an electron plasma wave (w_{pe} , k_{pe}). This takes place near the critical density n_{cr} as shown in Figure $2-1$. If the two waves product are two electron-plasma waves, we have the two-plasmon-decay ($2w_{pe}$) instability. This occurs near $(1/4)n_{cr}$. The Raman scattering instability represents the decay of the light wave into a scattered light wave (w_{sc}) plus an electron plasma wave, a process which occurs for $n_e < (1/4)n_{cr}$. The analogous scattering process in which the electron plasma wave is replaced by an ion-acoustic wave is called the Brillouin scattering instability and occurs for $n_e < n_{cr}$.

In the ion-acoustic and two-plasmon decay instabilities part of the laser energy will be transferred to plasma waves and this represents energy absorption by the plasma. On the other hand in Raman and Brillouin scattering, an electromagnetic wave is also produced which can escape from the plasma. This represents reflection of the incident laser radiation by the plasma.

For strong coupling of the laser light wave to the excited waves, the following matching or "resonance" conditions must be satisfied

$$w_L = w_1 + w_2 \qquad (2-26)$$

$$\mathbf{k}_L = \mathbf{k}_1 + \mathbf{k}_2 \qquad (2-27)$$

where w_L and $\mathbf{k}_L$ are the frequency and wave number of the laser light and w_1 , w_2 , $\mathbf{k}_1$, $\mathbf{k}_2$ the frequencies and wave numbers of the excited waves. The frequency matching conditions will determine the region of plasma densities for which the various instabilities occur. Also in order for the excited waves to grow, the laser field must feed energy into the waves w_1 and w_2 faster than the natural rate of energy dissipation or damping of these two modes. The latter requirement determines a "threshold intensity" for the laser "pump" field below which w_1 and w_2 are not excited. For any given process the threshold will depend on the strength of the coupling and on the damping of the natural modes of oscillation. These thresholds can be calculated theoretically as a function of the plasma parameters[30] and are given in Table $2-1$.

Table 2–1

Partial list of the instabilities which can be driven by laser light propagating in a plasma

name	process	density	threshold intensity[31–33] W/cm^2>
parametric-decay instability	$w_L \rightarrow w_{pe} + w_{ia}$	at $n_e \sim n_{cr}$	$6.72 \times 10^{19} T_e^{3/2} \lambda_L^{-5/3} \times L^{-2/3} n_e^{1/2}$
two-plasmon-decay instability	$w_L \rightarrow w_{pe} + w_{pe}$	at $n_e \sim (1/4) n_{cr}$	$3 \times 10^{13} Z\, T_e^{-1/2} \lambda_L^{-3}$
Raman scattering	$w_L \rightarrow w_{sc} + w_{pe}$	at $n_e < (1/4) n_{cr}$	$5 \times 10^{17} L_L^{-4/3} \lambda_L^{-2/3}$
Brillouin scattering	$w_L \rightarrow w_{sc} + w_{ia}$	at $n_e < n_{cr}$	$7.5 \times 10^{12} T_e \lambda_L^{-1} L^{-1} (\frac{n_{cr}}{n_e})$

where T_e, n_e, λ_L and L are in eV, cm^{-3}, μm and μm respectively.

Evaluation of the threshold intensities for typical conditions in our experiment, namely , $T_e = 500$ eV, $n_e = 4 \times 10^{21}$ cm^{-3}, $Z = 11$, $L = 80\,\mu$m and $\lambda_L = 0.532\,\mu$m

yields 9.8×10^{10} W/cm^2 for the parametric-decay instability, 9.8×10^{13} W/cm^2 for the two-plasmon-decay instability, 2.2×10^{15} W/cm^2 for the stimulated Raman scattering instability and 8.8×10^{13} W/cm^2 for the stimulated Brillouin scattering instability. Since typical laser intensities of 10^{13} W/cm^2 are used in our experiments, laser-driven plasma instabilities are not expected to play a significant role. The parametric-decay instability could be excited but because of the strong inverse bremsstrahlung absorption only very little laser energy will reach the critical density where the instability is excited.

Chapter 3

Electron thermal transport in laser produced plasmas

As we have seen inthe irradiation of a solid by a high power laser, the laser energy can only be absorbed in the "blow-off" plasma. It is mainly the heated electrons which transport the energy from the laser-absorption region towards the solid interior thereby controlling the mass ablation rate and the ablation pressure generated at the solid surface (in the case of high Z target material, the X-rays can also contribute significantly to the transport of energy). Electron thermal conduction thus play a very important role. For high laser intensities very strong density and temperature gradients exist in the plasma. The classical theory of heat transport in plasmas can no longer be applied and an exact description of energy transport becomes very complex. Furthermore coherent fluctuations in the ion charge density (ion turbulence) and large self-generated d c.magnetic fields in the plasma may also affect the heat flow. Some of these considerations are described here as background for laser experiments in general.

Some basic concepts of electron thermal conduction are introduced in Section $3-1$. In Section $3-2$ we review the classical theory of Spitzer-Härm on the thermal conductivity of a plasma and show that it is valid only in plasmas with small temperature gradients. In Section $3-3$ we discuss the problem of heat transport in laser-produced plasmas which are characterized by large temperature gradients. Finally in Section $3-4$ we will mention two possible mechanisms which may contribute to a reduction of the heat flux in laser produced plasma.

In our work attempts were made to ascertain the role of electron thermal conduction in the series of multilayer targets experiments presented in Chapter 7. However as will be seen in Chapter 7 our results revealed anomalies which precluded such interpretation in our experiment.

3–1 Basic concepts

A temperature gradient in a plasma gives rise to a heat flux which tends to equalize the temperature difference. This heat flux represents an energy transfer by particles which have a thermal velocity given by $V_t = (kT/M)^{1/2}$, where T is the temperature of the particles contributing to the heat flux and M their mass. Because of their lower mass, the electrons have a much higher thermal velocity than the ions and therefore play the main role in heat transport. Electrons with higher thermal energy will tend to move down a temperature gradient. This produces an electric field which then gives rise to a return electron current. As a result, there is a net flow of thermal energy towards the colder layers of plasma with no net current flowing. This heat flux is proportional to the relative temperature drop, and the heat flux crossing a unit plane can be described by :

$$Q = -K\frac{dT}{dx} \qquad (3-1)$$

where K is the plasma thermal conductivity. Since the electrons contributing to the heat flux at a given plane come from a distance of the order of their mean free path, equation $(3-1)$ is strictly valid only if the temperature gradient is constant over a distance of few mean free paths. Otherwise, the heat flux at a given plane will not depend only on the local thermal conductivity and temperature gradient, as implied by equation $(3-1)$, but will also depend on energy transport by electrons many free paths away. This condition is most commonly expressed as $\lambda_e/L_T < 1$ where λ_e is the mean free path of energy carrying electrons and L_T is the temperature gradient scale length.

An expression for the plasma thermal conductivity can be obtained using a simple electron thermal transport theory. Let us imagine a plane perpendicular to a temperature gradient dT/dx and calculate the heat fluxes passing through it in both directions. Each of the fluxes is :

$$Q \sim n_e V_{te} \times m_e V_{te}^2 \sim n_e V_{te} T_e \qquad (3-2)$$

where n_e is electron density and V_{te} their thermal velocity. These heat fluxes are due to the motion of the electrons which travel, prior to collision, a distance which is about their

mean free path λ_e. Since the heat fluxes in both directions are due to the particles moving on different sides of the plane where the temperatures are different, the net flux is :

$$Q \sim n_e V_{te} \Delta T \quad . \tag{3-3}$$

Here ΔT is the temperature difference over a distance of the order of the mean free path (the characteristic size of the region from which the electrons get to the plane without collisions with other particles, that is, without energy exchange). Hence, we obtain $\Delta T \sim \lambda_e \, dT/dx$ and :

$$Q \sim n_e V_{te} \lambda_e \frac{dT}{dx} \quad . \tag{3-4}$$

A comparison with equation $(3-2)$ yields the following dependence for the thermal conductivity :

$$K \sim n_e V_{te} \lambda_e = n_e \frac{V_{te}^2}{\nu_{ei}} \tag{3-5}$$

where ν_{ei} is the electron-ion collision frequency. Since $\nu_{ei} \sim n_e/T_e^{3/2}$ (see eq. $2-5$ and $2-6$ of chapter 2) and $V_{te} \sim (T_e/m_e)^{1/2}$ equation $(3-5)$ can be rewritten as :

$$K \sim \frac{T_e^{5/2}}{m_e} \quad . \tag{3-6}$$

The thermal conductivity of a plasma is therefore an extremely sensitive function of temperature (for comparison, in an ordinary gas[34] $K \sim T_e^{1/2}/M$ since the mean free path $\lambda \sim 1/N$ where N is the density of the gas particles). Also we see that the thermal conductivity is independent of the density of the electrons. Indeed, an increase in electron density gives rise to a proportional increase in the number of electrons transporting heat and to a proportional decrease in the mean free path of the electrons. These two effects cancel each other.

Using this simple theory we can only obtain a rough estimate for the thermal conductivity. A more correct treatment of heat transport in a plasma requires the velocity distribution of the electrons to be taken into consideration as discussed in the next section.

3–2 Spitzer-Härm theory of thermal conductivity: small temperature gradients

In the kinetic theory of plasma the electrons are represented through their velocity distribution function $f(\mathbf{r},\mathbf{v},t)$. By definition the electron density $n(\mathbf{r},t)$ at point $\mathbf{r}$ is given by : $n(\mathbf{r},t) = \int f(\mathbf{r},\mathbf{v},t)\,d^3\mathbf{v}$ where $d^3\mathbf{v}$ represents a three dimensional volume element in velocity space. For equilibrium conditions $f(\mathbf{r},\mathbf{v},t)$ is a Maxwellian distribution function. A temperature gradient in the plasma distorts the velocity distribution and a heat flux $\mathbf{Q}$ appears which is given by[35] :

$$\mathbf{Q} = \int f(\mathbf{r},\mathbf{v},t)\,\frac{m_e v^2}{2}\,\mathbf{v}\,d^3\mathbf{v} \quad . \tag{3-8}$$

Equation $(3-8)$ is similar to equation $(3-2)$ but here an average over the velocity distribution $f(\mathbf{r},\mathbf{v},t)$ is taken. The evolution of the distribution function is described by the Boltzmann equation:

$$\frac{\partial f}{\partial t} + \mathbf{v}\cdot\frac{\partial f}{\partial \mathbf{r}} + \frac{e\mathbf{E}}{m_e}\cdot\frac{\partial f}{\partial \mathbf{v}} = \left(\frac{\partial f}{\partial t}\right)_{\text{coll}} \quad , \tag{3-9}$$

where $(\partial f/\partial t)_{\text{coll}}$ is a Fokker-Planck[36] collision term which represents the electron-ion and electron-electron interactions in the plasma. $\mathbf{E}$ is a self-consistent electric field , related to the temperature gradient by the expression for the current density in a plasma :

$$\mathbf{J} = \sigma\mathbf{E} + \alpha\nabla\mathbf{T} = 0 \quad , \tag{3-10}$$

where σ and α are appropriate coefficients[36]. The temperature gradient produces a current in the plasma and as a result a secondary electric field $\mathbf{E}$ builds up which draws a return current such as to maintain a zero net current. The net current has to be equal to zero as otherwise an electrostatic field would rise without limit.

The thermal conductivity of a plasma using the kinetic theory was first calculated by Spitzer and Härm[36]. In their treatment they assumed a small temperature gradient which produces a small perturbation on the velocity distribution function which they write in the form :

$$f(\mathbf{v}) = f^0(\mathbf{v}) + f^1(\mathbf{v}) \quad \text{with} \quad f^1 << f^0 \tag{3-11}$$

where $f^0(\mathbf{v})$ is the unperturbed Maxwellian velocity distribution and $f^1(\mathbf{v})$ is a small perturbation due to the temperature gradient. After substitution in the Boltzmann equation $(3-9)$ and neglecting second order terms, a second order differential equation for the perturbation function $f^1(\mathbf{v})$ was obtained. The equation was solved numerically and values were obtained for $f^1(\mathbf{v})$ in terms of the parameter λ_e/L_T where λ_e is the mean free path of the electrons and L_T the temperature gradient scale length. Using these values of $f^1(\mathbf{v})$ the heat flux carried by the distribution function was then evaluated from equation $(3-8)$ (only the perturbation contributes to the heat flux). Comparison with equation $(3-1)$ then yielded the following expression[37] for the thermal conductivity K.

$$K = 2 \times 10^5 \Big(\frac{2}{\pi}\Big)^{3/2} \frac{c^4 k (kT_e)^{5/2}}{m_e^{1/2} e^4 Z \ln\Lambda} \Big(\frac{0.095(Z+0.24)}{(1+0.24Z)}\Big) \qquad \text{(SI units)} \quad . \qquad (3-12)$$

where Z is the average charge of the ions, c the speed of light and $\ln\Lambda$ is the Coulomb logarithm (see eq. $(2-7)$ of chapter 2).

Substituting the physical constants, this can also be expressed as :

$$K = 1.86 \times 10^{-10} \frac{T_e^{5/2}}{Z \ln\Lambda} \Big(\frac{Z+0.24}{1+0.24Z}\Big) \qquad \Big(\text{W/°K m}\Big) \qquad (3-13)$$

The Spitzer-Härm theory was derived under the assumption that $f^1(\mathbf{v}) << f^0(\mathbf{v})$. However, Gray and Kilkenny[38] have pointed out that the perturbation function $f^1(\mathbf{v})$ increases with λ_e/L_T and at some velocity, depending on λ_e/L_T, $f^1(\mathbf{v})$ can become greater than $f^0(\mathbf{v})$. Then, the assumption that $f^1(\mathbf{v})$ is a small perturbation is no longer valid. Also, since the function $f^1(\mathbf{v})$ can take negative values the distribution function $f(\mathbf{v})$ may then become negative. This is clearly unphysical. It comes about because higher order terms are neglected. However, they also pointed out that a negative value for $f(\mathbf{v})$ would not matter in the velocity range whrere the heat flux is very small. Their analysis then showed that the heat flux was carried mainly by electrons whose velocity is between 2.3 to 3 times the thermal velocity and that the distribution function $f(\mathbf{v})$ became negative in this velocity range for $\lambda_e/L_T \;>>\; .02$.

Plasmas produced by high-power lasers frequently exhibit very sharp temperature gradients over distance comparable to the mean free path of electrons. In the next section,

we discuss how the heat flux is usually treated in a ser-heated plasma with steep temperature gradients and also discuss the theoretical work which are aimed at improving the understanding of electrons thermal transport in such situation.

3-3 Thermal transport in laser produced plasmas : large temperature gradients

The Spitzer-Härm heat conduction law is not a correct description of heat transport when too many of the heat-carrying electrons have mean free paths exceeding the local temperature gradient scale length. In a laser heated plasma this condition predominates in the high density region, immediatly beyond the laser energy deposition zone. The Spitzer-Härm conductivity greatly overestimates the heat flux under such circumstances. In computer hydrodynamic simulations of laser-plasma experiments, it has been customary to artificially limit the heat flux to a maximum value which corresponds to free particle flow. The heat flux is then described by a law of the type:

$$Q = \min\left(Q_{SH}, Q_{FS}\right) \quad , \qquad (3-14-A)$$

or

$$Q = \left(Q_{SH}^{-1} + Q_{FS}^{-1}\right)^{-1} \quad , \qquad (3-14-B)$$

where Q_{SH} is the Spitzer-Härm heat flow and Q_{FS} is the "free-streaming flux" :

$$Q_{FS} = F\, n_e k T_e V_{te} \quad , \qquad (3-15)$$

representing the energy carried by a flow of free streaming electrons. F is called the flux limiter and is a parameter less than unity, which is adjustable in the numerical simulation. Heuristic arguments suggest[39] that $F \sim 0.2-0.6$. However[40-41] in numerical simulations, a better fit to many experimental results is obtained if F is reduced to about 0.03 . This has been interpreted as an indication that electron thermal transport is strongly inhibited in laser-produced plasmas. Some mechanisms have been proposed to explain such inhibition (see next section). Since the "free-streaming limit" is essentially a crude attempt to estimate an upper bound to the heat flux when the classical theory of Spitzer-Härm breaks down, it was also suggested[42] that a correct treatment of electron thermal transport for large

temperature gradients might reveal a much lower conductivity than as previously been supposed.

A more accurate treatment of heat transport in steep temperature gradients was given by Bell, Evans and Nicholas[43]. In their work, the Boltzmann equation (eq. $(3-9)$) was solved numerically, by expressing the distribution function $f(\mathbf{v})$ as an expansion of Legendre polynomials. They then calculate the heat flux , using equation $(3-8)$, for a one-dimensional static plasma (no ion motion) with prescribed temperatures T_1 and T_2 across a large temperature gradient. Their results show, as expected, that in the presence of a steep temperature gradient the heat flux at any point is not simply a function of the local plasma state (as assumed in the classical conduction theory of Spitzer-Härm) but is also determined by the state of the surrounding plasma over a region which is several mean free path thick. Also, on the main body of the heat front, the heat flux is an order of magnitude less than that given by the Spitzer-Härm theory. This is equivalent to a free streaming heat flux with a flux limiter $F = 0.1$. Similar work[44–46] of other groups have led to the same general conclusion. Thus a more correct treatment indeed shows a reduction in the heat flux compared to the Spitzer-Härm theory or the classical free-streaming flux limiter $F \sim 0.2-0.6$. However , this is still much larger than the phenomenological free-streaming flux (see above) with $F \sim .03$ which reproduces experimental results better.

3-4 Thermal transport inhibition mechanisms

Two mechanisms have been proposed[41] to account for a reduction of the heat flux in laser-produced plasmas. These are self-generated magnetic fields and ion acoustic turbulence.

It should be noted that in our experiment using moderate laser intensities and long pulse irradiation the temperature gradient is not expected to be large compare to the mean free paths of the electrons. Therefore in Chapter 4 which describes a simple analytical model of the ablation process, the classical expression for the plasma thermal conductivity (eq. $3-12$) will be used. Self-generated magnetic fields and ion acoustic turbulence are not included in this simple model. They are described here for completeness.

3–4–A Self-generated magnetic field

Megagauss self-generated magnetic fields B have been observed in laser produced plasmas[47–48]. The heat flux is not modified when the temperature gradient is parallel to the magnetic field[35]. However electron thermal transport across the field lines will be reduced when the electron Larmor radius $\rho_L \equiv e\, m_e V_{te}\,/(eB)$ is less than the collisional mean free path λ_e. Under these conditions the step-size for random walk of the electrons across a field line becomes ρ_L instead of λ_e and the cross-field heat flux is reduced by the factor $R = [1 + (\lambda_e/\rho_L)^2]^{-1}$. For example, in plasmas where $Z = 4$, $B = 1$ MG, $n_e = 10^{21}$ cm^{-3} and $kT_e = 1$ keV, $R \sim 0.05$ which shows that this effect becomes significant.

3–4–B Ion acoustic turbulence

In the presence of large coherent fluctuations in the ion charge density (ion turbulence), electrons will be scattered from the coherent ion charge bunches. This effectively increases the electron-ion collision frequency[38] ν_{ei} . Since the plasma thermal conductivity is inversely proportional to ν_{ei} (see eq. $(3-5)$), these fluctuations reduce the heat flux.

It has been proposed[38,49–50] that the electron heat flux itself could give rise to ion turbulence via the ion-acoustic instability. The process can best be understood with reference to Figure $(3-1)$. In this figure we have represented, in the frame of reference in which the mean particle velocity is zero, the reduced distribution $F(v_\parallel) \equiv \int f(v)\, dv_\perp$ ($v_\parallel$ is the velocity in the direction of the heat flux) for the ions and the electrons. The ions are taken to be considerably colder than the electrons, so their distribution $F_i(v_\parallel)$ is narrow. The electron distribution $F_e(v_\parallel)$ is distorted for $v_x < 0$ because heat is being carried in the $-x$ direction by electrons with speeds $|v_x| > v_{te}$. To avoid a net current flow, this current of high velocity electrons is balanced by a return current of low velocity electrons which causes a shift in the peak of the distribution function. The shift in the peak is given by[38] :

$$v_D \simeq 0.43 \frac{\lambda_e}{L_T} v_{te} \quad . \qquad (3-16)$$

The ion acoustic wave velocity is approximately

$$v_{ia} \simeq \left(\frac{ZkT_e + kT_i}{m_i} \right)^{1/2} \quad , \qquad (3-17)$$

and if $ZT_e >> T_i$ this can be well above the thermal ion velocity v_{ti} which is

$$v_{ti} = \left(\frac{kT_i}{m_i}\right)^{1/2} \quad . \qquad (3-18)$$

Thus there are insufficient ions moving at the wave velocity to cause significant ion Landau damping (Landau damping or Landau growth of waves arises from an exchange of energy between the wave and the particles travelling with velocities close to the phase velocity of the wave). Conversely if $v_D >> v_{ia}$, the slope of the electron velocity distribution is positive near the ion acoustic velocity v_{ia} and this causes unstable amplification of the ion waves by Landau growth. From equation $(3-16)$ and $(3-17)$ the criterion for instability is :

$$v_{ia} \simeq \left(\frac{ZkT_e}{m_i}\right) < v_D \simeq 0.43\frac{\lambda_e}{L_T}v_{te} \qquad (3-19)$$

or

$$\frac{\lambda_e}{L_T} > 2.3\left(\frac{Zm_e}{m_i}\right)^{1/2} \simeq 0.05 \quad (\text{ for } \quad Z=1) \qquad (3-20)$$

In most laser produced plasmas this threshold is exceeded and ion acoustic turbulence is certainly excited. However from the point of view of transport inhibition one must also know the effect of a given amount of ion turbulence on the plasma transport coefficients. Many authors have suggested that the turbulence has little effect on electron thermal transport[51]. Other authors find that significant inhibition can occurs[52–53]. This is clearly an area where more theoretical work is needed.

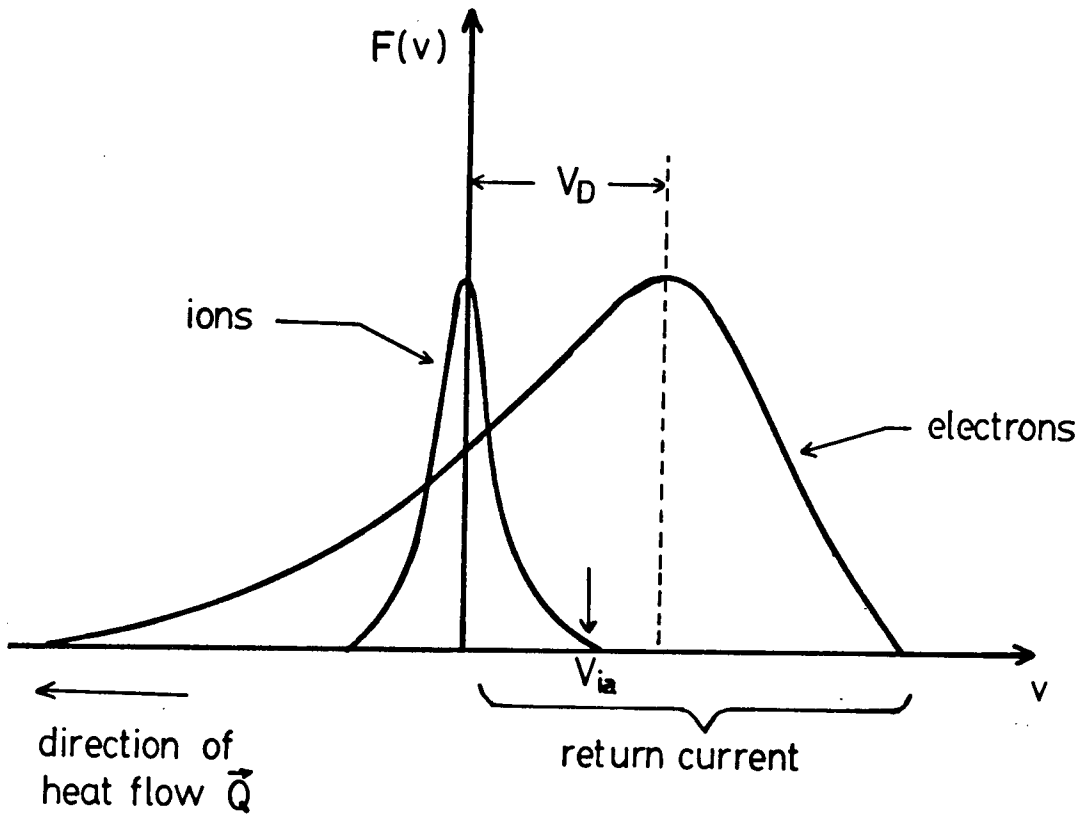

Figure 3-1 Electron and ion distributions in the presence of an electron heat flux **Q**. When $V_D >> V_{ia}$ and $ZT_e >> T_i$, the ion -acoustic instability grows rapidly (see text).

Chapter 4

Scaling laws for the mass ablation rate and ablation pressure: one dimensional steady-state ablation theory

In this chapter, using a simple analytical model, we study the plasma flow which develops in the irradiation of a solid with a high power laser. We will be particularly interested in finding how the plasma temperature, the mass ablation rate and the ablation pressure generated by the ablation process at the solid surface vary with the laser intensity and wavelength. Such dependences on the laser parameters are generally referred to by the inclusive term "scaling laws". In Chapter 6 and 8, these theoretically determined scaling laws will be compared with experimental results.

Several analytical studies of laser-driven ablation of solid exist and references 15, 67 and 68 review the subject. The principal goal of these analytical models is to shed light on the dominant physical processes, which are sometimes obscured in computer hydrodynamic simulations. The most crucial assumption which affects the scaling laws, made in these models[15], concerns the absorption regime (strong or weak inverse bremsstrahlung absorption) which determines the electron density where most of the laser energy absorption occurs. In this chapter we use the analytical model of Manheimer and Colombant[56], which assumes laser energy deposition at the critical density n_{cr}, to establish scaling laws in the weak inverse bremsstrahlung absorption regime and the model of Mora[57], which assumes laser energy deposition at a density n_0 which is less than the critical density n_{cr}, to establish scaling laws in the strong inverse bremsstrahlung absorption regime. In Section $4-1$ we give a physical description of the plasma flow stucture to be analysed. Section $4-2$ contains a description of the analytical model, together with a derivation of the scaling laws and a discussion of the model assumptions.

4–1 Structure of the laser induced plasma flow

When intense laser light is focussed on a solid in vacuum a thin layer at the surface of

the solid is vaporized and ionized, producing a high density plasma. The very rapid temperature increase at the solid surface causes the laser-produced plasma to expand or "blow-off" towards the laser beam.

The dispersion relation of an electromagnetic wave in a plasma (see eq. $(2-1)$ of Chapter 2) does not allow wave propagation in a plasma region where the electron density is higher than the critical density. As the laser radiation propagates through the "blow-off" plasma towards the solid, it encounters regions of increasing plasma density . It will penetrate up to a maximum electron density n_0 (with corresponding mass density ρ_0, see eq. $4-4$) which for strong inverse bremsstrahlung absorption conditions can be much less than the critical density (see for example Figure $2-2$ of Chapter 2). We call the layer where the electron density $n_e = n_0$ the "absorption surface". The thermal gradient which exists between the hot plasma at the absorption surface and the cold solid, will drive a flow of energy towards the solid by electron thermal conduction. (At high laser intensity a significant portion of the energy can also be transported by fast, non-thermal electrons or in the case of high Z plasma, by radiation. However we will limit our description to cases where these two mechanisms are not important). This will cause more material to be heated up and ablated from the solid and there will be a continuous flow of new material from the ablation surface as long as the laser irradiation process continues. This flow of material carries away momentum with it and by Newton's third law of motion there is a corresponding force exerted on the remaining solid. This force,designated as ablation pressure, drives a shock wave into the solid and compresses and accelerates sucessive layers of the solid material as new layers of the solid are ablated[57-63]. A schematic of this global structure is shown in Figure $4-1$. It represents a snapshot of the density and temperature profiles, in the solid and the "blow-off" plasma. We can distinguish four different regions:

i) the plasma corona which extends from the absorption surface ($\rho = \rho_0$) into the vacuum,

ii) the conduction zone bounded by the ablation surface and the absorption surface,

iii) the shock-compressed and -heated solid, and

iv) the unperturbed solid material ahead of the shock front.

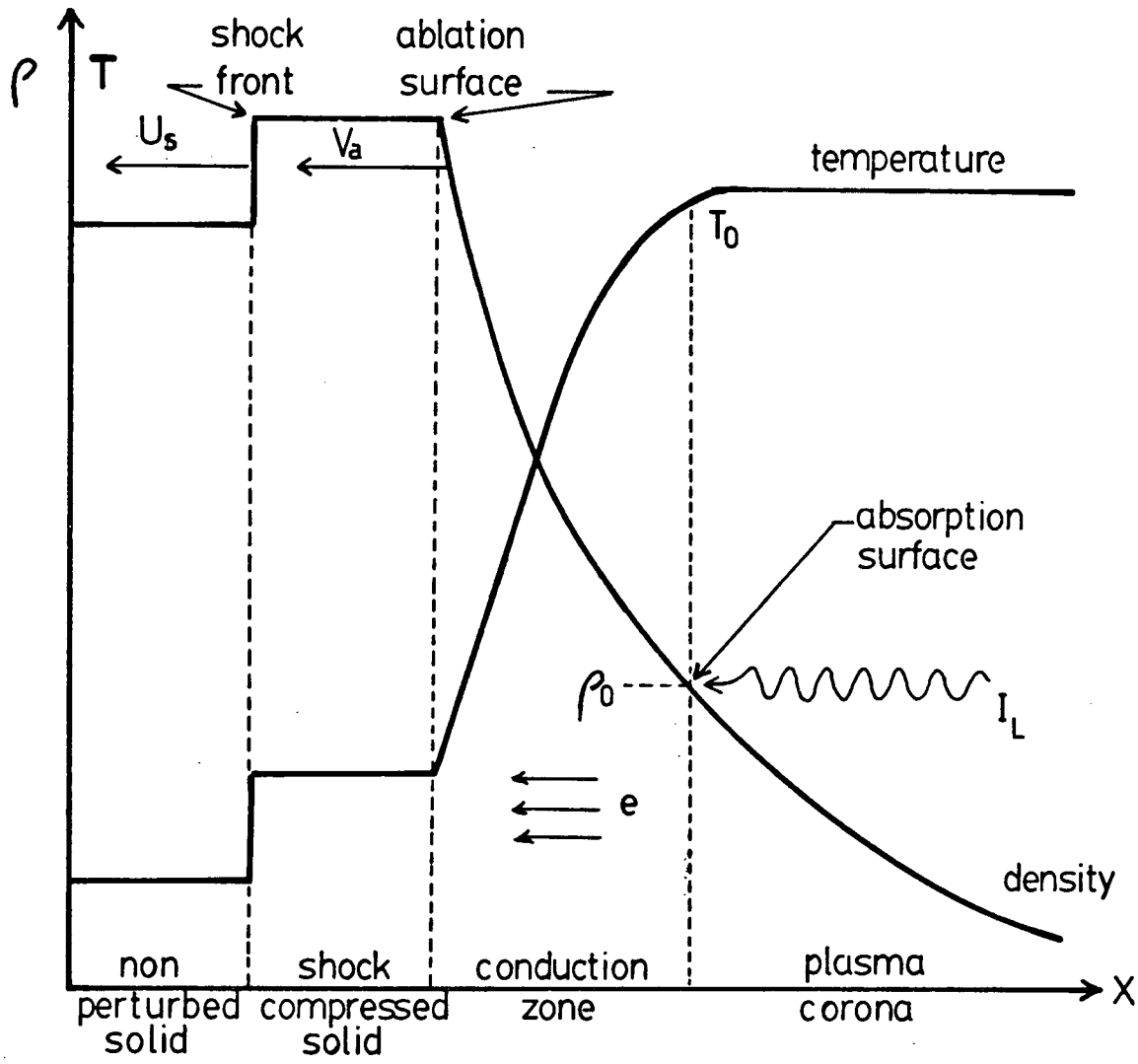

Figure 4-1 Structure of the steady-state plasma flow: density and temperature profiles.

Figure $4-2$ shows an $x-t$ diagram of the flow stucture identifying different density surfaces associated with the shock front, the ablation surface and the absorption surface. The laser is turned on at $t=0$ and its intensity is assumed to remain constant thereafter. After some initial transients, for $t > t_1$, the distance x_0 between the absorption surface and the ablation surface remains constant indicating that a steady state regime has been reached in the conduction zone. That this is to be expected can be seen as follows. If the thickness of the conduction zone starts to increase (the laser intensity being constant), there will be less energy reaching the surface of the solid. Therefore less plasma is produced and the thickness of the conduction zone will start to decrease. If instead, the thickness of the conduction zone starts to decrease (again for constant laser intensity), the reverse process will take place. The thickness of the conduction zone is therefore self-regulated and adjusts itself to the laser intensity. In Figure $4-2$ we have also depicted the trajectory of a particle of the solid. Initially at rest, it is first accelerated by the shock wave. At a later time it is overtaken by the ablation surface, heated and accelerated in the conduction zone. Finally it is ejected with large velocities away from the solid surface.

In the following section we will show how the characteristics of the laser radiation, its intensity and wavelength, and the properties of the solid material affect the rate at which material is ablated from the solid and the ablation pressure which is generated by this process at the solid surface.

4–2 One dimensional steady-state ablation theory

4–2–A Conservation equations and model assumptions

The basic properties of the plasma flow occurring as a result of the irradiation of a solid with intense laser light can be described by applying the conservation equations for mass, momentum and energy. To obtain simple analytical solutions for these equations we will assume that:

i) The plasma flow from the solid can be described using one-dimensional planar geometry.

ii) The flow in the conduction zone has reached a steady state and thus the width the zone is constant and equal to x_0.

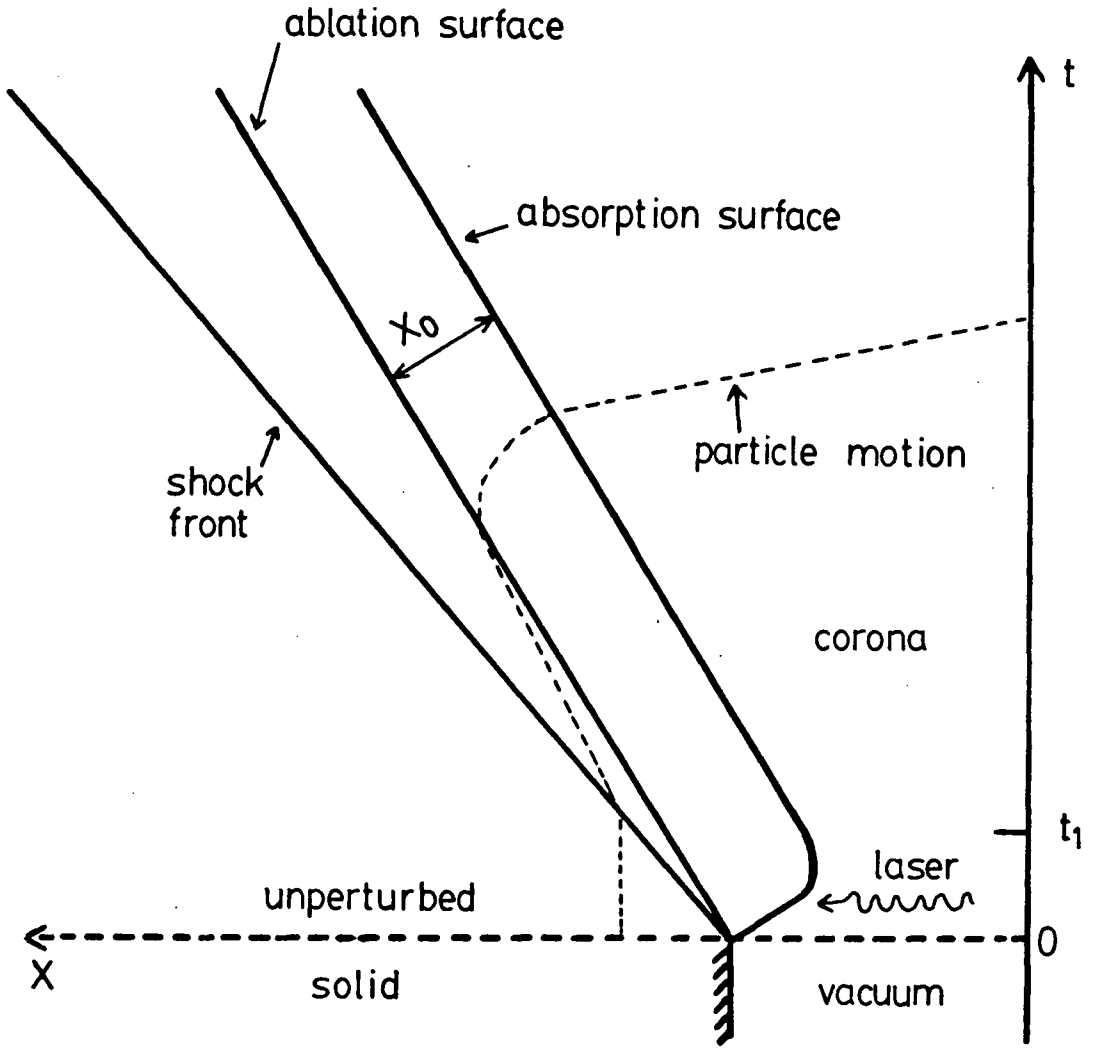

Figure 4-2 Space-time diagram for the densities associated to the shock front, the ablation surface and the absorption surface. The laser pulse is a step function starting at $t = 0$. For $t > t_1$ the conduction zone has reached a steady state.

Conditions for the applicability of these two assumptions will be given in section 4 – 2 – E .

In one-dimensional form, the conservation equations for mass, momentum and energy can be written[64] as :

$$\frac{\partial \rho}{\partial t} + \frac{\partial}{\partial x}(\rho V) = 0 \quad , \tag{4-1}$$

$$\frac{\partial}{\partial t}(\rho V) + \frac{\partial}{\partial x}(P + \rho V^2) = 0 \quad , \tag{4-2}$$

$$\frac{\partial}{\partial t}(\frac{3}{2}\rho C^2 + \frac{\rho V^2}{2}) + \frac{\partial}{\partial x}[\rho V(\frac{V^2}{2} + \frac{5}{2}C^2) + Q] + I_A \delta(x - x_0) = 0 \quad , \tag{4-3}$$

where:

- V is the plasma flow velocity ;

- ρ represents the mass density, given by :

$$\rho = n_i A m_p + n_e m_e \simeq \frac{n_e A m_p}{Z} \quad , \tag{4-4}$$

  where n_i is the ion density, n_e the electron density, A the atomic mass number of the ion and Z its average electric charge, m_e is the electron mass and m_p the proton mass;

- C represents the sound speed in a plasma , given by :

$$C = (\frac{Z+1}{A m_p} k T_e)^{1/2} \quad ; \tag{4-5}$$

- P is the plasma pressure which is defined through the equation of state :

$$P = n_e k T_e + n_i k T_i = \rho(\frac{Z+1}{A m_p})kT = \rho C^2 \quad , \tag{4-6}$$

where we have assumed that the electron temperature T_e is equal to the ion temperature T_i . This simplifying assumption, which is certainly reasonable in the high density conduction zone, will not affect the general application of the results to be derived[15–60];

- Q represents the heat flux ; it is given by equation $(3-1)$ and $(3-12)$ of chapter 3 which we rewrite in the form :

$$Q = -K_0 T^{5/2} \frac{dT}{dx} \quad ; \qquad (4-7)$$

- $I_A \delta(x - x_0)$ is a delta function which represents the absorption of laser energy at the absorption surface located at $x = x_0$ It is assumed that this energy is rapidly distributed in the plasma by two heat flux Q_{in} and Q_{out}, originating at $x = x_0$, and flowing towards and away from the solid.

In our description of the plasma flow, the flow structure is divided into the three regions identified on Figure $4-1$. These are the plasma corona, the conduction zone and the shock compressed target. Solutions for the conservation equations $(4-1)$ to $(4-3)$ can be found in each of these regions. Appropriate boundary conditions must then be used to connect the solutions between the different regions. We will limit our treatment only to the flow solutions which are essential to derive scaling laws for the mass ablation rate and the ablation pressure. For this purpose it will be sufficient to solve the conservation equations only in the plasma corona and the conduction zone.

4–2–B Flow solutions in the plasma corona : isothermal expansion

The coronal plasma is expanding into a vacuum and therefore it cannot reach a steady state[56]. This expansion will be described by the time dependent conservation equations $4-1$ to $4-3$. To obtain simple analytical solutions we will assume that the plasma is isothermal throughout the expansion region. This implies that the plasma thermal conductivity must be sufficient to maintain the plasma temperature constant against cooling by

expansion. Since the plasma temperature is high in the plasma corona and since the thermal conductivity is an extremely sensitive function of temperature ($\alpha T_e^{5/2}$) this assumption is not unreasonable.

We will use one-dimensional planar geometry to describe the expansion of the plasma. We introduce a spatial coordinate system x' attached to the unperturbed plasma (see Figure $4-3$). At $t = 0$ the plasma occupies the half-space $-\infty < x' < 0$ and starts to expand. We assume that $T(x') = T$ =constant so that $\frac{\partial P}{\partial x'} = (\frac{Z+1}{Am_p})kT\frac{\partial \rho}{\partial x'} = C^2\frac{\partial \rho}{\partial x'}$ and therefore equations $(4-1)$ and $(4-2)$ can be solved for the dynamical variables of plasma density ρ and velocity V'. These two equations do not contain any characteristic length or characteristic time. The time t and the coordinate x' can appear in the solutions of such a problem only in the combination x'/t. It is therefore convenient to use the variable $\xi = x'/t$. Thus,

$$\frac{\partial}{\partial x'} = \frac{d}{td\xi} \quad \text{and} \quad \frac{\partial}{\partial t} = \frac{-\xi}{t}\frac{d}{d\xi} \quad ,$$

and substitution in equations $(4-1)$ and $(4-2)$ gives:

$$(V' - \xi)\frac{d\rho}{d\xi} + \rho\frac{dV}{d\xi} = 0 \quad , \tag{4-8}$$

and

$$(V' - \xi)\frac{dV}{d\xi} + \frac{C^2}{\rho}\frac{d\rho}{d\xi} = 0 \quad . \tag{4-9}$$

The two partial differential equations $(4-1)$ and $(4-2)$ have thereby been reduced to two ordinary differential equations which can be solved for V' and ρ to give:

$$V' = C + \frac{x'}{t} \quad , \tag{4-10}$$

and

$$\rho = \hat{\rho}\exp -(1 + \frac{x'}{Ct}) \quad , \tag{4-11}$$

$\hat{\rho}$ being the density of the unperturbed plasma.

The solution $(4-11)$ for the density profile is represented in Figure $4-3$. It shows an exponential density profile which extends to infinity in the vacuum region and includes

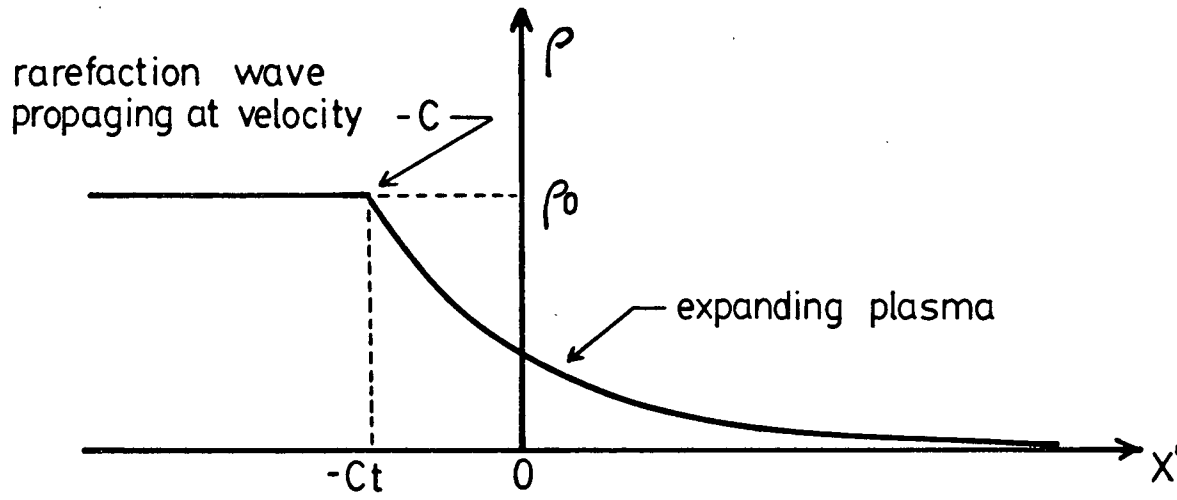

Figure 4-3 Density profile for isothermal plasma expansion.

a rarefaction wave which propagates into the unperturbed plasma at the sound velocity $-C$. Let us rewrite these equations in a new coordinate system x attached to the ablation surface and in which the absorption surface is located at the position $x = x_0$ (see Figure 4−1). The transformation equation from the coordinate system x' to the coordinate system x is $x' \longrightarrow (x - x_0) - C_0 t$, where the subscript "0" is used to denote values for the variables at the absorption surface (where $x = x_0$). In this new frame of reference the solutions $(4-10)$ and $(4-11)$ take the form :

$$V(x) = C_0 + \frac{x - x_0}{t} \quad , \qquad (4-12)$$

and

$$\rho(x) = \rho_0 \exp\left(\frac{x_0 - x}{C_0 t}\right) \qquad (4-13) \quad .$$

These solutions imply that for the isothermal rarefaction wave in the coronal plasma to stay in equilibrium with a steady state conduction zone, the plasma flow velocity at the boundary between these two regions must be equal to the local sound speed $V(x_0) = C_0$.

Let us now calculate the heat flux necessary to maintain isothermal conditions in the expanding coronal plasma. Equation $(4-3)$ describe the energy balance in this region. The first term represents the rate of energy flux in the rarefaction wave. The second term an enthalpy flux coming from the conduction zone and the third term the heat flux Q_{out} supplied by the absorption of laser energy at the absorption surface $x = x_0$ (third term). To evaluate Q_{out} we integrate the energy equation $(4-3)$ from $x = x_0$ to infinity. Making use of the flow solutions $(4-12)$ and $(4-13)$ we get:

$$Q_{out} = \frac{\partial}{\partial t}\int_{x_0}^{+\infty}\left(\frac{3}{2}\rho C^2 + \frac{1}{2}\rho V^2\right)dx + \left[\rho V\left(\frac{5}{2}C^2 + \frac{V^2}{2}\right)\right]_{x_0}^{+\infty} = \rho_0 C_0^3 \qquad (4-14)$$

This result will be used later in the laser energy balance equation.

4–2–C Flow solutions in the conduction zone: steady state flow

To describe the flow in the conduction zone we choose the same frame of reference in which the solutions $(4-12)$ $(4-13)$ are written. In this frame of reference, for steady state condition, the conservation equations $(4-1)$ to $(4-3)$ become:

$$\frac{\partial}{\partial x}(\rho V) = 0 \quad , \qquad (4-15)$$

$$\frac{\partial}{\partial x}(P + \rho V^2) = 0 \quad , \qquad (4-16)$$

and

$$\frac{\partial}{\partial x}\left[\rho V\left(\frac{V^2}{2} + \frac{5}{2}C^2\right) + Q_{in}\right] + I_A\delta(x - x_0) = 0 \qquad (4-17) \quad .$$

Integrating equations $(4-15)$ and $(4-16)$ give :

$$\rho V = \rho_0 C_0 = \dot{m} \quad , \qquad (4-18)$$

and

$$\rho C^2 + \rho V^2 = 2\rho_0 C_0^2 = P_A \quad . \qquad (4-19)$$

Here we have made use of the fact that the plasma flow velocity must be equal to the sound speed at the absorption surface to connect smoothly with the solutions in the coronal region of the flow (see eq. $(4-12)$). Equation $(4-18)$ shows that the mass flux is constant throughout the conduction zone and equal to to the mass ablation rate $\dot{m}$. Equations $(4-18)$ and $(4-19)$ can be solved for the plasma flow velocity to give:

$$V = C_0 - (C_0^2 - C^2)^{1/2} \qquad (4-20)$$

The total outward flow of plasma energy $(1/2)\rho V^3 + (5/2)\rho VC^2$ (see eq. $(4-17)$) through the absorption surface is $3\rho_0 C_0^3$, (obtained by setting $V = C_0$ at the absorption surface). This flow is balanced, as indicated by equation $(4-17)$, by an inward heat flux Q_{in} which provides the energy for the ablation process. We have already shown (see eq. $(4-14)$) that there is an outward heat flux Q_{out} equal to $\rho_0 C_0^3$ which maintains isothermal conditions in the coronal region. Therefore energy balance requires that the absorbed laser intensity is equal to:

$$I_A = Q_{in} + Q_{out} = 4\rho_0 C_0^3 = 4(\frac{Am_p}{Z})n_0 C_0^3 \quad . \qquad (4-21)$$

4–2–D Scaling laws

Using equations $(4-5)$,$(4-18)$,$(4-19)$ and $(4-21)$, the following expressions for the plasma temperature, the mass ablation rate and the ablation pressure are obtained:

$$T_0 = 4^{-2/3}(\frac{A}{Z})^{1/3}\frac{m_p^{1/3}}{k}n_0^{-2/3}I_A^{2/3} \quad , \qquad (4-22)$$

$$\dot{m} = 4^{-1/3}(\frac{Am_p}{Z})^{2/3}I_A^{1/3}n_0^{2/3} \quad , \qquad (4-23)$$

and

$$P_A = 4^{-2/3}(\frac{Am_p}{Z})^{1/3}I_A^{2/3}n_0^{1/3} \qquad (4-24)$$

The density n_0 will depend on the absorption regime. Two different cases can be considered.

i) **Weak inverse bremsstrahlung absorption : $n_0 = n_{cr}$**

For long laser wavelength and high intensity, inverse bremsstrahlung absorption is relatively negligible (see section 2 – 1 of chapter 2) and absorption of the laser energy occurs mainly at the critical density through resonant absorption (section 2 – 3). In this case n_0 is equal to the critical density which is given by:

$$n_0 = n_{cr} \equiv \frac{4\pi^2 c^2 m_e \epsilon_0}{e^2 \lambda_L^2} \qquad (4-26)$$

substitution in equations (4 – 22), (4 – 23) and (4 – 24) yields:

$$T(\mathrm{eV}) = 5.9 \times 10^2 (\frac{A}{Z})^{1/3} I_A^{2/3} \lambda_L^{4/3} \quad , \qquad (4-27)$$

$$\dot{m}(\mathrm{g\,cm^{-2}\,s^{-1}}) = 7.1 \times 10^4 (\frac{A}{Z})^{2/3} I_A^{1/3} \lambda_L^{-4/3} \quad , \qquad (4-28)$$

$$P_{Abl}(\mathrm{Mbar}) = 5.1 (\frac{A}{Z})^{1/3} I_A^{2/3} \lambda_L^{-2/3} \qquad (4-29)$$

where the units of I_A and λ_L are respectively 10^{13} W/cm^2 and μm .

ii) **Strong inverse bremsstrahlung absorption : $n_0 < n_{cr}$**

For short laser wavelength and low intensity, inverse bremsstrahlung absorption is high and the energy can be totally absorbed before the critical density (see Figure 2 – 2 of chapter 2). It is possible to evaluate the maximum density n_0 beyond which very little laser energy is transmitted (Mora[57]). The absorption of laser energy through the plasma is (eq. (2 – 10) of chapter 2):

$$A = 1 - \exp[-\int_{x_0}^{+\infty} a_\omega(x)\,dx] \qquad (4-30)$$

The absorption coefficient a_ω for inverse bremsstrahlung is given by the expression (2 – 8) of chapter 2 which we rewrite in the form :

$$a_\omega(x) = \alpha n_{cr} T_e^{-3/2} (\frac{n(x)}{n_{cr}})^2 (1 - \frac{n(x)}{n_{cr}})^{-1/2} \qquad (4-31)$$

where α is a constant which can be obtained by comparison with eq. $(2-8)$. Using the expression for the density profile, equation $(4-13)$, for an isothermal expansion in the plasma corona $(T = T_0)$, together with equation $(4-4)$, equation $(4-30)$ can be rewritten as:

$$A = 1 - \exp\{-\alpha n_{cr} T_0^{-3/2} (\frac{n_0}{n_{cr}})^2 \int_{x_0}^{+\infty} \left(1 - \frac{n_0}{n_{cr}} \exp -\frac{(x-x_0)}{C_0 t}\right)^{-1/2} \exp -\frac{2(x-x_0)}{C_0 t}\, dx\} \tag{4-32}$$

Assuming $(n_0/n_{cr})\exp -\frac{(x-x_0)}{C_0 t} << 1$ we can easily evaluate the integral to get:

$$-\alpha T_0^{-3/2} n_{cr} (\frac{n_0}{n_{cr}})^2 \frac{C_0 t}{2} = \ln(1-A) \quad . \tag{4-33}$$

To evaluate the density n_0, we can assume[57] that $A = 0.86$, noting that a change of its numerical value will affect the absolute value of n_0 but not its scaling with other parameters. Thus from equation $(4-33)$

$$n_0 = \frac{2 n_{cr}^{1/2} T_0^{3/4}}{\alpha^{1/2} (C_0 t)^{1/2}} = \frac{2 n_{cr}^{1/2} T_0^{3/4}}{\alpha^{1/2} L^{1/2}} \quad . \tag{4-34}$$

The density gradient scale length $L = C_0 t$ for short laser pulse is roughly equal to $C_0 \tau_L$, where τ_L is the laser pulse length. On the other hand , if the laser pulse length is so long that $C_0 \tau_L$ becomes larger than the diameter of the focal spot D_{spot}, the spherical divergence of the plasma flow will limit L to a length of the order of D_{spot} [16]. Therefore

$$L \simeq \min\,(C_0 \tau_L, D_{\rm spot}) \tag{4-35}$$

Finally substitution of equation $(4-34)$ in equations $(4-22)$, $(4-23)$ and $(4-24)$ yields the scaling laws for strong inverse bremsstrahlung absorption :

$$T(\mathrm{eV}) = 89 (Z \ln\Lambda)^{2/9} (\frac{A}{Z})^{2/9} L^{2/9} \lambda_L^{4/9} I_A^{4/9} \quad , \tag{4-36}$$

$$\dot{m}(\mathrm{g\,cm^{-2}\,s^{-1}}) = 4.5 \times 10^5 (Z \ln\Lambda)^{-2/9} (\frac{A}{Z})^{7/9} L^{-2/9} \lambda_L^{-4/9} I_A^{5/9} \quad , \tag{4-37}$$

and

$$P_{Abl}(\text{Mbar}) = 6.6(Z \ln \Lambda)^{-1/9}(\frac{A}{Z})^{7/18} L^{-1/9} \lambda_L^{-2/9} I_A^{7/9} \qquad (4-38)$$

where the units of I_A are 10^{13} W/cm^2 and the units of λ_L and L are μm .

4-2-E Discussion of model assumptions

In this section we examine the model assumptions (one-dimensional flow and steady-state conduction zone) and derive criteria which delineate the regions of parameter space where they can be applied.

i) One-dimensional flow

In the model it was assumed that the plasma flow can be described using one-dimensional planar geometry. This will be true only if the lengths of interest are small compared to the focal spot size, a distance beyond which the flow will definitely be divergent[16]. In particular the scaling laws were determined from the values of the hydrodynamic variables at the absorption surface. Therefore a reasonable criteria for a one-dimensional description to be valid would be that the distance from the ablation surface to the absorption surface (length of the conduction zone) must be much smaller than the laser focal spot diameter. The length of the conduction zone can be obtained by integrating the energy equation $(4-17)$ for $x < x_0$. We find

$$\dot{m}(\frac{5}{2}C^2 + \frac{V^2}{2}) + Q_{\text{in}} = 0 \quad , \qquad (4-39)$$

where the constant of integration is equal to zero since the outward flux of kinetic energy and enthalpy is balanced by the inward heat flux (the amount of energy transmitted to the solid through the shock wave is small compared to the energy in the conduction zone). Using expression $(4-20)$ for the plasma flow velocity and expression $(4-7)$ for the heat flux, we can rewrite equation $(4-39)$

$$dx = \frac{2K_0 T^{5/2}\, dT}{\dot{m}[5C^2(T) + (C_0 - (C_0^2 - C^2(T))^{1/2})^2]} \quad . \qquad (4-40)$$

Numerical integration of this equation from $T = 0$ at the ablation surface to $T = T_0$ at the absorption surface gives[60] :

$$x_0 = 0.15 \frac{K_0 T_0^2}{\rho_0} \left(\frac{A m_p}{(Z+1)k} \right)^{3/2} \qquad (4-40)$$

This can be rewritten using equations $(4-4)$, $(4-5)$, $(4-21)$ and $(3-13)$ as :

$$x_0 = 2.59 \times 10^{37} \frac{Z^{4/3}}{(Z+1)^{7/2}} \left(\frac{Z+0.24}{1+0.24Z} \right) \frac{A^{7/6}}{\ln \Lambda} \frac{I_A^{4/3}}{n_0^{7/3}} \qquad \text{(SI units)} \quad . \qquad (4-41)$$

Let us evaluate this expression for typical conditions in our experiments, namely:

$$I_A = 10^{13}\ \mathrm{W/cm^2},\ A = 27,\ Z = 11 \quad ;$$

$$n_0 = 0.27\, n_{cr} \quad \text{and} \quad \ln \Lambda = 2.4 \quad \text{for} \quad \lambda_L = 0.266\, \mu m \quad ;$$

$$n_0 = 0.36\, n_{cr} \quad \text{and} \quad \ln \Lambda = 2.9 \quad \text{for} \quad \lambda_L = 0.355\, \mu m \quad ;$$

$$n_0 = 0.55\, n_{cr} \quad \text{and} \quad \ln \Lambda = 3.7 \quad \text{for} \quad \lambda_L = 0.532\, \mu m \quad ;$$

where n_0 is given in Figure $2-2$ of Chapter 2. This yields

$$x_0 \sim 9.6\, \mu m \quad \text{at} \quad 0.266\, \mu m \quad ;$$

$$x_0 \sim 16.3\, \mu m \quad \text{at} \quad 0.355\, \mu m \quad ;$$

and

$$x_0 \sim 32\, \mu m \quad \text{at} \quad 0.532\, \mu m \quad .$$

Thus x_0 is strongly dependent on the laser wavelength. Since our laser focal spot diameter is 80 μm for 90 % energy content (see section $5-2$ of chapter 5) the one-dimensional flow assumption is only marginally satisfied for our experimental conditions.

ii) **Steady state flow in the conduction zone**

The plasma flow structure and the hydrodynamic variables ρ, v, T all depend on the laser intensity and therefore a complete steady state cannot exist when using a laser pulse whose intensity varies with time. However if the laser intensity does not change sharply on a time scale shorter than the times it takes the plasma flow to adjust to intensity changes then the flow is at all times in a " quasi-steady-state" i.e. in equilibrium with the changing laser intensity. Time-avaraged values of the measured ablation parameters can then be related to the time-averaged value of the laser intensity. A more precise criteria for this situation to exist[55,60] is that the laser intensity should not change significantly in the time it takes a fluid element to flow from the ablation surface to the absorption surface. This flow time is given by:

$$\tau_f = \int_0^{z_0} \frac{dx}{V(x)} \quad . \qquad (4-42)$$

Using equation $(4-20)$ for $V(x)$ and $(4-40)$ for dx ,we fin by numerical integration of equation $(4-42)$:

$$\tau_f = 0.1 \frac{I_A}{\rho_0^2} \left(\frac{Am_p}{(Z+1)k} \right)^{7/2} K_0 \quad . \qquad (4-43)$$

Using equations $(4-4)$ and $(3-13)$ we can rewrite this expression

$$\tau_f = 1.30 \times 10^{29} \frac{Z}{(Z+1)^{7/2}} \left(\frac{Z+0.24}{1+0.24Z} \right) \frac{A^{3/2}}{\ln \Lambda} \frac{I_A}{n_0^2} \qquad \text{(SI units)} \qquad (4-44)$$

Evaluating this expression for the same experimental parameters that we used to evaluate expression $4-41$ yields

$$\tau_f = 230\,ps \quad \text{at} \quad 0.266\,\mu m \quad ;$$

$$\tau_f = 350\,ps \quad \text{at} \quad 0.355\,\mu m \quad ;$$

and

$$\tau_f = 600\,ps \quad \text{at} \quad 0.532\,\mu m \quad .$$

Since our laser pulse is near-gaussian with a full-width at half-maximum intensity of 2ns (see Section $5-3$ of Chapter 5), a steady state regime will exist for most of the interaction in our experiment.

Chapter 5

Experimental facility and diagnostics

In this chapter we describe the experimental facility, experimental conditions and diagnostics which were used in our experiments. The laser system and the experimental arrangement are described in Section 5 – 1. Target irradiation conditions are detailed in Section 5 – 2. In Section 5 – 3 we describe various diagnostics used. Finally in Section 5 – 4 we describe the procedure used in the fabrication of multilayer targets used in some of our experiments.

5–1 Neodymium-glass laser system and the experimental arrangement

The experimental facility is based on a Quantel neodymium-glass laser system (model NG-34), which includes a Nd-YAG (neodymium-yttrium aluminum garnet) oscillator, a Nd-YAG preamplifier and two Nd-glass amplifiers. The aperture of the final amplifier rod is 25 mm in diameter. The laser oscillator is passively Q-switched with a dye-cell and provides a single laser pulse at 1.064 μm in the TEM_{00} mode.The temporal pulse shape is approximately gaussian with a full width at half maximum (FWHM) intensity of 2 ns. The laser system also includes three KDP (potassium dihydrogen phosphate) crystals for harmonic generation at 0.532, 0.355 and 0.266 μm. The system is capable of delivering 12 joules at 1.064 μm, 6 joules at 0.532 μm, 2 joules at 0.355 μm and 1.5 joule at 0.266 μm. A schematic of the laser system and an oscilloscope trace of the oscillator laser pulse are shown in Figure 5 – 1.

A schematic of the experimental set-up is shown in Figure 5 – 2. The collimated laser beam (25 mm diameter) of 0.532, 0.355 or 0.265 μm wavelength is brought to the target chamber through a series of three or more dichroic mirrors. The laser light is then focussed on target using $f/10$ optics. The use of dichroic mirrors, together with the chromatic aberration of the focussing lens, reduces the intensity of unwanted harmonic laser radiation on target to negligible level (less than one part in 10^5). As shown in Figure 5 – 2, a beam

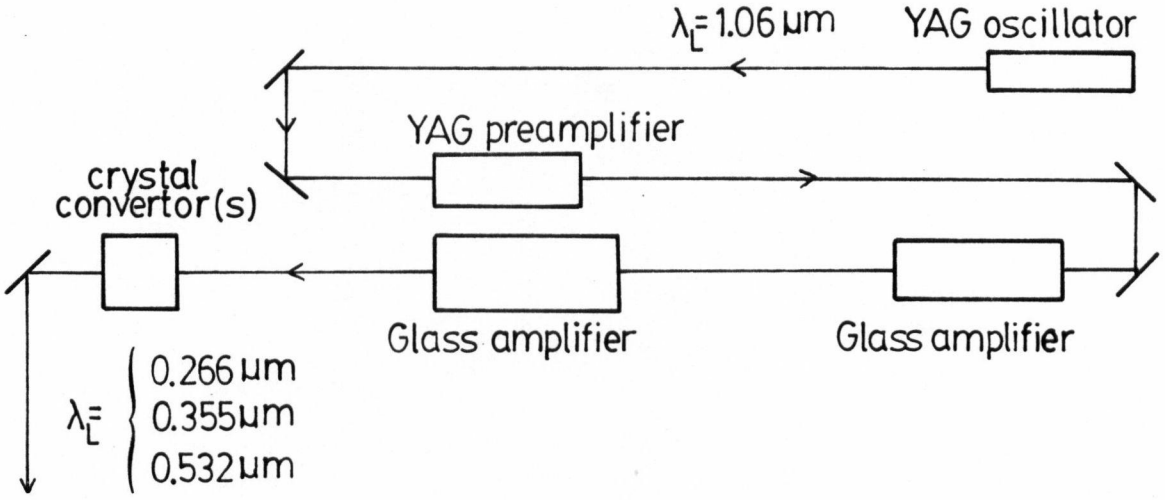

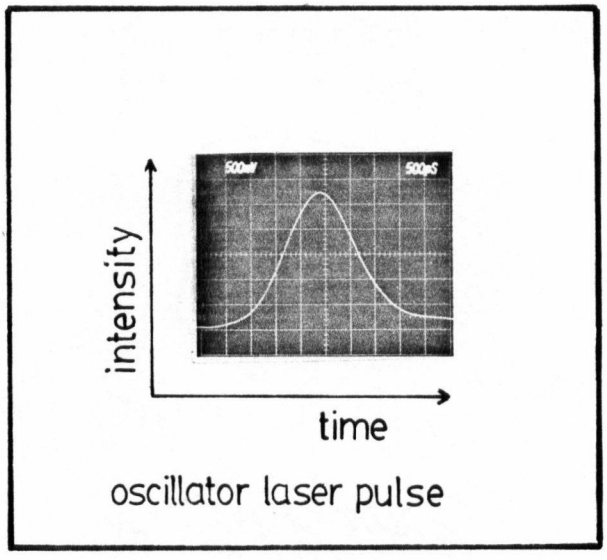

Figure 5–1 Schematic of the laser system and oscilloscope trace of the oscillator laser pulse.

splitter is inserted in the laser beam path for diagnostic purposes. It reflects part of the incident laser light towards a Gentec laser energy meter (model ED-200) which measures the incident laser energy,and part to a fast photodiode (Hamamatsu model R1193U, 350 ps rise time) which monitors the laser pulse shape. The same beam splitter is used to sample part of the backscattered light, which is monitored with similar energy and power detectors. The wavelength of the back scattered light was identified by placing different interference filters in front of the photodiode monitor. The overall transmission of the relay optics for the incident laser beam was measured for each laser wavelength. Also shown on Figure $5-2$ is the optical arrangement used to image the laser focal spot onto the photocathode of a streak camera. Details of this measurement will be given in Section $5-2$.

The target chamber is a cylindrical vacuum vessel two feet high and two feet in diameter. It is equipped with various ports to allow laser beam input, access for optical diagnostics and electrical connections. It can be evacuated with a forepump to less than 100 mTorr (1 Torr=132 Pascals) in a few minutes. When necessary a vacuum of the order of 10^{-5} Torr (monitored with an ionization gauge) can be attained within several hours using a 15 cm aperture diffusion pump attached to the chamber.

The targets were mounted near the center of the vacuum chamber on a target wheel placed at the focus of the lens. The target wheel was driven by a stepping motor which could be operated from outside the chamber. It was possible in this way to perform a large number of laser shots on different targets without having to break the vacuum seal. The target normal was oriented 10° from the laser beam axis to prevent direct specular reflection feeding back into the laser chain. It also rendered the axis of symmetry of the plasma "blow-off" accessible to measurements.

5–2 Irradiation conditions

In order to maximize the laser intensity, the laser light was sharply focussed onto the target. To position properly the focussing lens, the backscattered laser energy was monitored as the position of the lens was varied. For a constant laser energy the power density on target is highest at the best focus and the backscattered laser energy will consequently be maximum for this lens position. Typical results for the 0.532 μm experiment are shown in Figure $5-3$. For this particular measurement, the incident laser energy was 1.2 joule

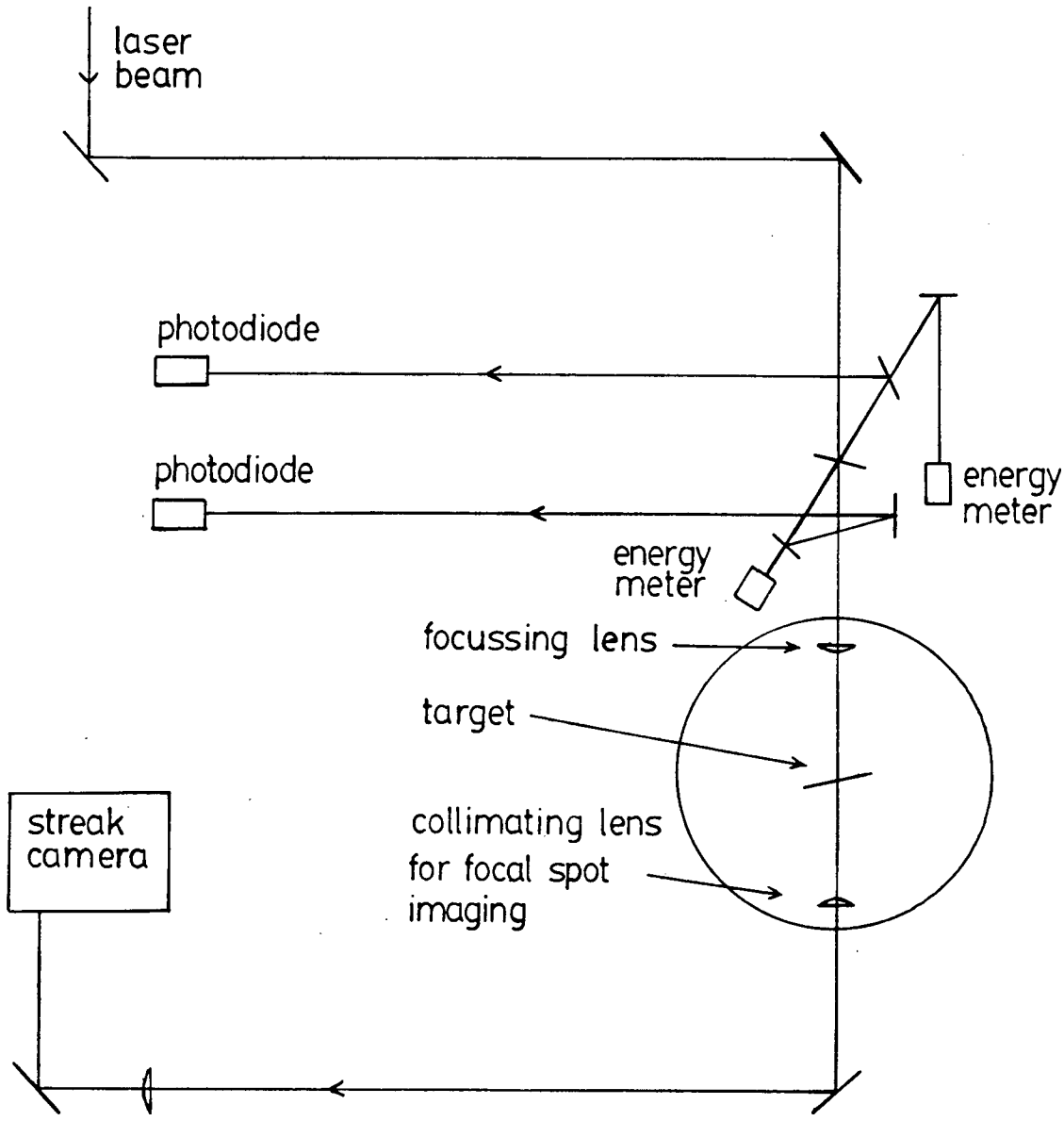

Figure 5–2 Experimental set-up.

and 130 μm thick glass slides were used as targets. The same procedure was used to focus laser radiation of 0.355 and 0.266 μm on targets.

Characterization of a laser-plasma interaction experiment requires the measurement of the spatial and temporal distributions of the laser energy at the target. This was made by imaging the laser focal spot onto the photocathode of a streak camera (Hamamatsu Temporal Disperser System , model C1370–01) which yielded either a time-resolved, one-dimensional image or a time-integrated, two-dimensional spatial distribution of the laser intensity at focus. The focal spot was imaged using both a single and a double-lens imaging system (see Figure 5 – 2). It is important that the imaging optic does not introduce aberrations on a scale larger than the details we want to measure. To establish the spatial resolution and magnification of our imaging system, we imaged a reticle placed at the target plane inside the target chamber. The resulting image indicated a spatial resolution better than 10 μm with a depth of field of 100 μm. With lens configurations we obtained overall magnifications ranging from 30 to 45. Figure 5 – 4, shows the intensity distribution across the diameter of the focal spot as a function of time. This corresponds to a 0.355 μm laser pulse of 0.8 joule. Figure 5 – 5 shows a time integrated two dimensional image showing the focal intensity distribution. This corresponds to a 0.532 μm laser pulse of 3.4 joules. Detailed analysis in similar measurements showed that 90% of the laser energy is contained within a spot of 80 μm diameter and 60% of the energy within a spot of 40 μm diameter. Time resolved (30 ps resolution) measurements showed spatial intensity modulations (4 μm resolution) of less than 30 %, and time integrated measurements showed modulations of less than 10%. The laser pulse length was close to 2 ns (FWHM). Variations up to 30% were observed in the focal spot size and laser pulse length when the laser energy on target was changed. Changes in the spot size were attributed to a thermal induced lensing effect ocurring in the laser rods since the laser energy on target was varied by changing the flashlamp pumping of the laser amplifier rods. On the other hand, the non-linear property of the frequency conversion crystal introduced distortion in the laser pulse shape for high laser intensity. The incident irradiances Φ_L specified throughout this work were defined according to the following formula

$$\Phi_L = \frac{E_L}{\tau_L \pi (D^2/4)} \quad , \qquad (5-1)$$

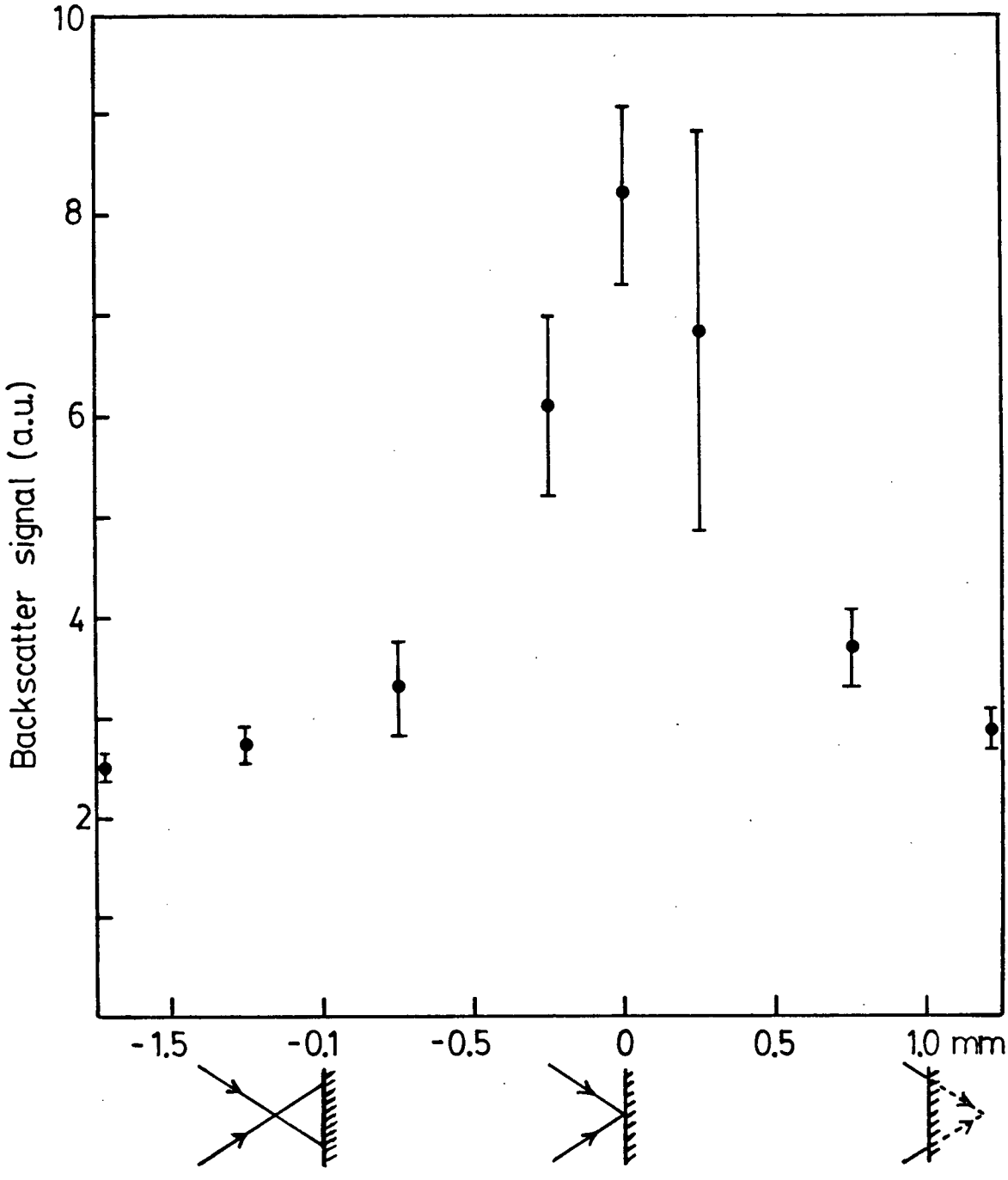

Figure 5–3 Backscatter signal as function of the lens position, $\lambda_L = 0.532\,\mu\text{m}$ $E_L = 1.2\text{J}$.

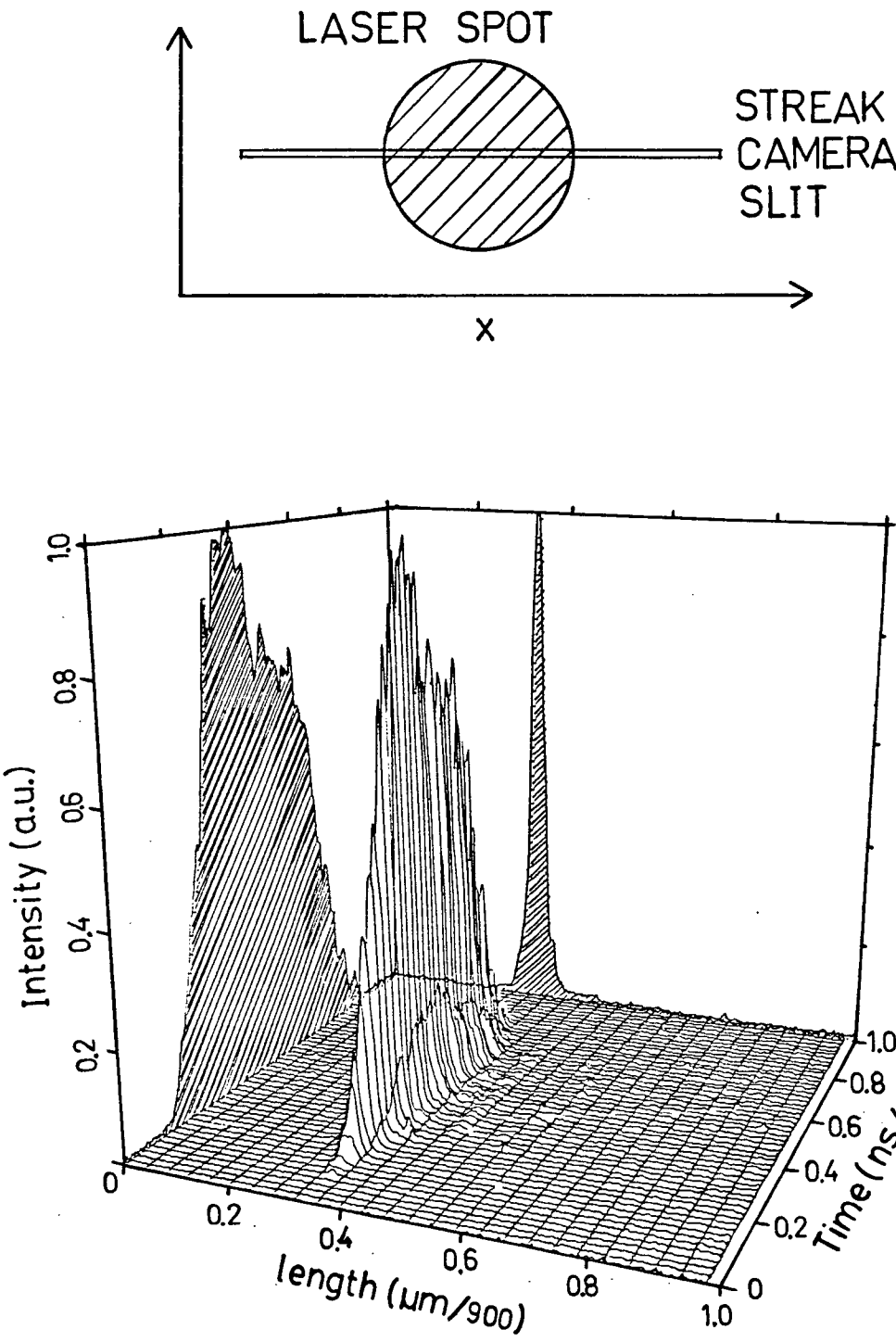

Figure 5–4 Intensity distribution across the diameter of the focal spot as a function of time for 0.355 μm laser light, $E_L = 1.2$ J.

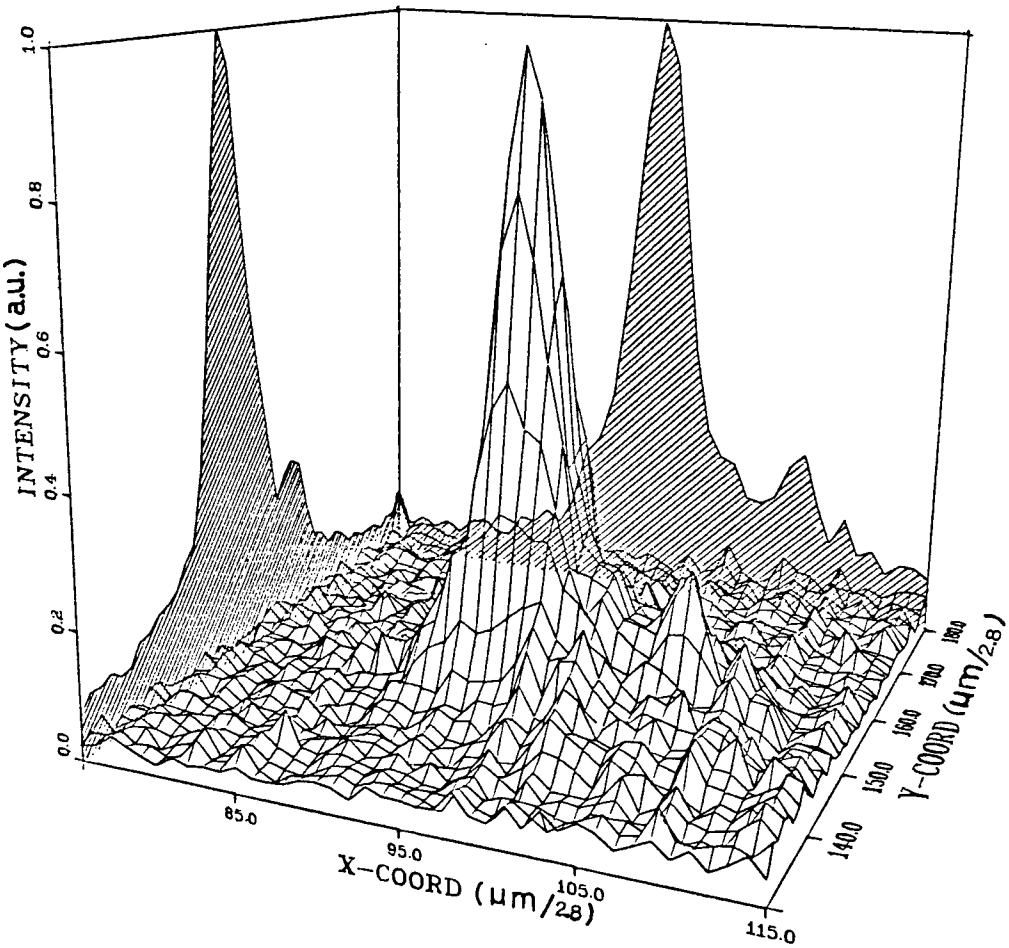

Figure 5–5 Time integrated two-dimensional image of the focal spot intensity distribution for 0.532 μm laser light, $E_L = 3.4$ J.

where E_L is the incident laser energy, τ_L the laser pulse length taken at FWHM and D the focal spot diameter containing 90 % laser energy.

5–3 Diagnostics

To facilitate the experimental investigation a comprehensive system of diagnostics was developed in-house. These include an integrating-sphere photometer (Section 5 – 3 – A), Faraday cups* (5 – 3 – B), differential calorimeters* (5 – 3 – C), an X-ray crystal spectrometer (5 – 4 – D), an X-ray film calibration technique (5 – 3 – E), X-ray pinhole cameras (5 – 3 – F) and a multichannel X-ray detector (5 – 3 – G). In particular the X-ray film calibration technique[69] and the multichannel X-ray detector[70] constitute new and original developments and are described in detail.

5–3–A Integrating-sphere

The simplest way to determine the fractional absorption of laser energy by the target is to measure the laser energy that is reflected or scattered from the target. It is easy to measure the energy reflected back through the focussing lens. However in laser produced plasmas , a large fraction of the unabsorbed laser light may be scattered in a rather diffused manner. Hence, a precise measurement of the energy reflected from the target requires a detector with a 4π collection angle. An integrating-sphere (or Ulbricht photometer) is ideal for this purpose. It consists essentially of a hollow sphere with its inner surface coated with a diffuse reflecting layer.

A diagram of the photometer developed for our experiments is shown in Figure 5 – 6. It is made of two aluminum hemispherical cavities of 7.6 cm radius. The surface of the cavity was coarsely sand-blasted and then coated with a diffusing paint (Eastman Kodak white reflectance coating[71] CAT 118 1759). The reflection coefficient[72] of the paint ranges from 94% to 99% between 2500 and 9000 Å. Separate apertures are provided for the incoming beam, the target holder and the radiation detectors. Their overall area is less than 10% of the total surface area of the sphere. Radiation scattered from the target is multiply

* A description of the Faraday cup (Section 5 – 3 – B) and differential calorimeter detectors (section 5 – 4 – C) has been given in Reference 59. These two detectors were developed by A.Ng and P.Celliers.

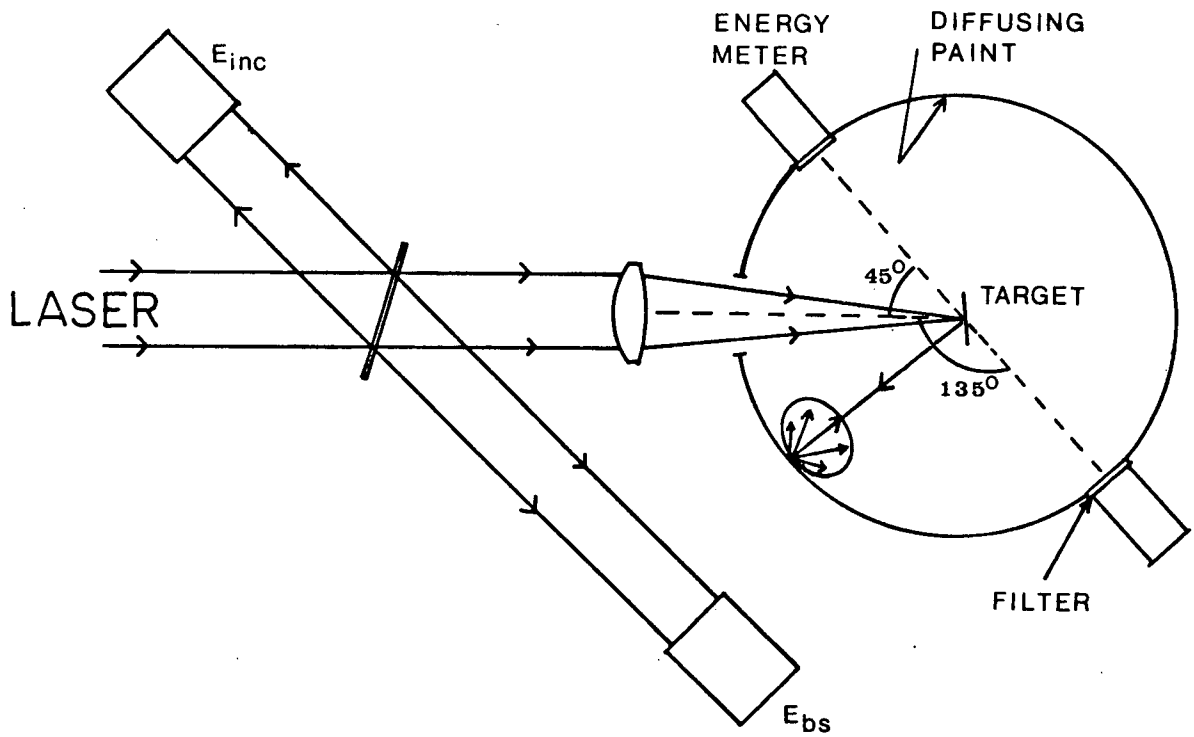

Figure 5–6 Experimental arrangement for laser energy absorption measurement.

reflected by the diffuse reflector surface and monitored by two calorimeters (Gentec model ED-200) positioned at angles of 45°and -135° with respect to the laser beam and in the plane of incidence. They are covered with a glass slide which blocks the plasma particles and X-rays and transmits only the laser light reflected by the sphere (most of the radiation energy emitted by the plasma is in the soft X-ray energy range, therefore mainly laser light with negligible plasma radiation is seen by the detectors).

An attractive feature of the Ulbricht photometer is that the measured intensity is independent of the angular distribution of the source[73]. The calibration of the sphere is therefore a straightforward procedure in which the target is removed and the laser light directly illuminates the rear wall of the sphere. The sphere efficiency, defined as E_{det}/E_{in} where E_{det} is the laser energy detected by the two detectors in the sphere and E_{in} is the input laser energy, is typically of the order of 4%. Absorption measurements using the integrating sphere are presented in Chapter 6.

5–3–B Faraday cup

A set of Faraday cups were used to determine the velocity of the ions in the expanding plasma. This is done by measuring the time of flight of the ions from the target to the Faraday cup detector which is positioned a known distance from the target. A schematic of a Faraday cup with its electrical connections is given in Figure 5 – 7 – A.

As shown in this figure the plasma which enters the detector first passes through a grid connected to ground and then encounters another grid which is biased at -215 V. This biased control grid rejects the electrons which do not have enough kinetic energy to overcome the grid potential. The ion stream then enters the cup through a 7 mm hole and strikes the collecting surface of the detector which is connected, via a 50 ohm coaxial cable, to an oscilloscope. A current pulse is produced which is proportional to the current density of the ion stream. The geometry of the cup serves to restrict the escape of secondary electrons which are generated when the ions strike the rear end of the cup. Any secondary electrons escaping from the cup are reflected by the negatively biased grid at the entrance. Figure 5 – 7 – B shows an example of an ion current trace for an aluminum target irradiated with 0.355 μm laser light at 10^{13} W/cm^2. The detector was positioned along the target normal, 35 cm away from the target. The ringing at the beginning of the trace is

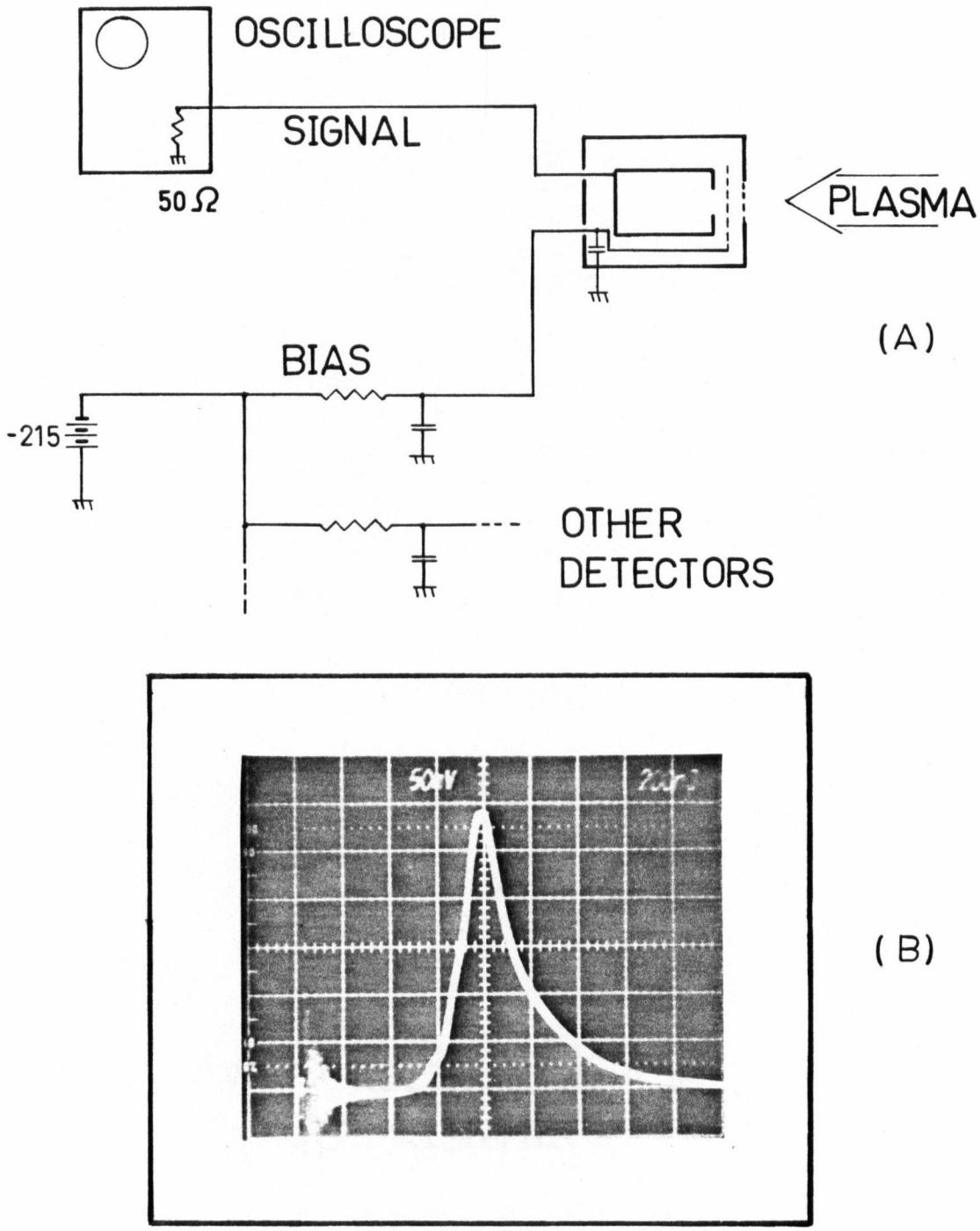

Figure 5–7 (A) Faraday cup electrical connections. (B) Oscilloscope display of a Faraday cup signal.

produced by the X-ray burst at the time the laser light is incident on the target, ejecting secondary electrons from the collector surface. This provides an excellent zero time marker for the time of flight analysis. Measurements obtained with these detectors are described in Chapter 8.

5-3-C Differential calorimeter

A set of differential calorimeters was used to measure the energy of the expanding plasma. The differential calorimeter consist of two minicalorimeters placed side by side and connected in a differential configuration (see Figure $5-8$).

One minicalorimeter measures all incident ion, electron, X-ray and light energy. The other minicalorimeter is covered with a glass slide and collects only the visible light energy. The difference in the signal of the two minicalorimeters constitutes the output of the detector. Evaluation of the X-ray contribution to the signal is then necessary in principle to obtain the particle energy. For our experimental conditions the X-ray contribution to the detector signal was assumed to be small and was neglected. The active element in each calorimeter is a Peltier effect thermoelectric juction in which a temperature gradient accross the device produces a voltage difference which can be recorded. The thermoelectric junction was attached on one side to an aluminum block which serves as heat sink, and on the other side to a small aluminum plate which serves as an absorber for incident plasma energy. The device is calibrated by discharging a known amount of electrical energy through a resistor embedded in the aluminum absorber plate. Measurements made with the differential calorimeters are discussed in Chapter 8.

5–3–D X-ray crystal spectrometer

An X-ray crystal spectrometer was developed to monitor X-ray line radiation from highly ionized silicon plasma. The instrument was used in an investigation of electron thermal transport (see Chapter 7), and was also used in a new calibration technique for X-ray films (see Section $5-3-$E). A schematic of the X-ray crystal spectrometer is shown in Figure 5–9. In this figure we show the use of X-ray film (covered with a step-wedge X-ray filter for intensity calibration purpose) as radiation detector; we have also used other detectors such as a PIN diode (see section $5-3-$E) and a plastic scintillator coupled to

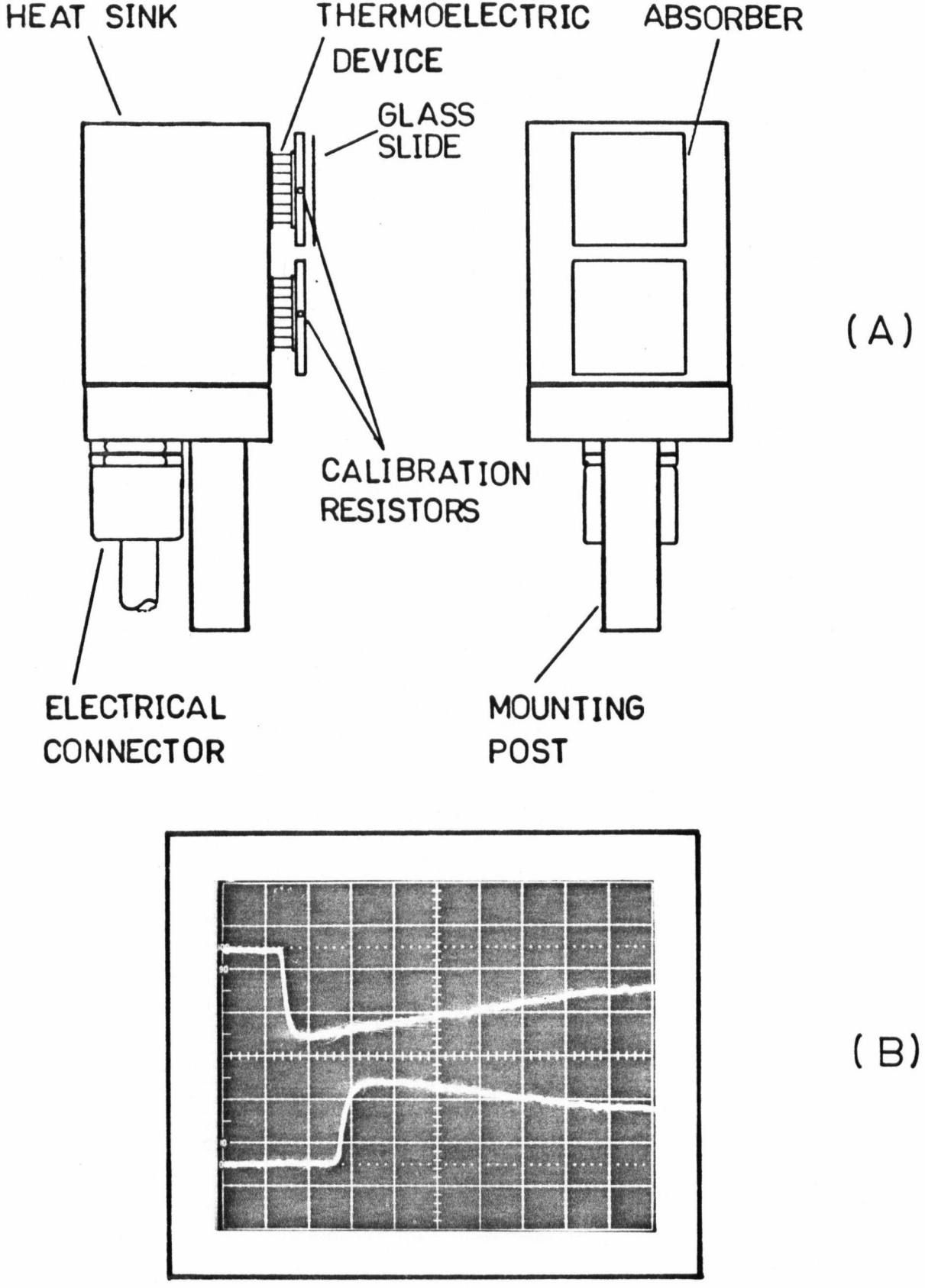

Figure 5–8 (A) Schematic of a differential calorimeter. (B) Oscilloscope display of a differential calorimeter signal.

a photomultiplier tube (see Chapter 7). Typical spectra obtained with the instrument can be seen in Figures 5 – 10, 5 – 15 and 7 – 2.

The key components of the spectrometer are a beryllium entrance window which protects the crystal from the plasma "blow-off", a flat potassium acid phthalate (KAP) crystal and an X-ray detector. The target-to-crystal distance was typically 12 cm with the crystal-to-detector distance of the order of 10 cm. The crystal length is 5 cm (2.5 cm wide and 3 mm thick). It is inclined 13.2° with respect to the line of sight to the target. Radiation from the target can fall on the crystal at angles of incidence varying from 10.9° to 16.6°. At each point on the crystal the local glancing angle of incidence and the Bragg diffraction condition

$$\lambda = 2d \sin \theta \qquad (5-2)$$

determine a unique value of photon wavelength that will be diffracted towards the X-ray detector with high efficiency. The 001 crytal planes, which have an interplanar distance of 13.31 Å, are used to reflect the X-rays. The reflection coefficient[96] of the crystal is of the order of 7×10^{-5} in the wavelength range covered by the instrument (from 5 to 7.5 Å). No slit was necessary between the target and the spectrometer, and good spectral resolution could be obtained because of the small size of the source (typically less than 100 μm).

5–3–E An in-situ X-ray film calibration technique

X-ray films have been widely used for the study of laser-produced plasmas[74–80], both in X-ray imaging and spectroscopy. They offer the advantages of excellent spatial resolution and good dynamic range. However, for quantitative measurements the response of the film has to be known and a characteristic curve relating film optical density to exposure has to be determined. The exact shape of this characteristic curve depends on many factors. First, it is wavelength dependent[81] so that calibration must be performed in the spectral region that the film is to be used for. It may also be affected by the film development procedures. The type of chemicals used, processing times and temperatures have to be well controlled to obtain consistent and reproducible results. Furthermore, it is well known that even for the same exposure the optical density of the film when measured with microdensitometers will depend on the type and the setting of the instrument[82]. Finally, changes in sensitivity between film batches and possible changes in film composition by manufacturers[83] can

modify the characteristic curve as well. Because of these considerations, users of X-ray films in general have to perform their own calibrations.

Film calibration is usually carried out in an independent measurement. A characteristic curve relating optical density to exposure is determined using a standard radiation source such as a fluorescent radiation source[81,83–84]. This is then used to analyse film exposure obtained in other measurements. Because of the aforementioned factors, extreme care must be exercised to ensure the applicability of the characteristic curve. Thus, an *in-situ* calibration technique would be most advantageous, since it would also eliminate the need of additional calibrations. We here describe an *in-situ*, relative X-ray film calibration technique. The technique is based on film exposure measurements of an X-ray spectrum transmitted through a step-wedge absorption filter. To demonstrate the technique we will discuss the construction of a characteristic curve for Kodak SC5 film using laser-produced silicon and aluminum plasmas as radiation sources. Results of the method showed good agreement with that obtained using an X-ray PIN diode as the recording device.

5–3–E–i *Calibration technique and characteristic curve*

In principle, the technique is a direct extension to the X-ray domain of the neutral-density step-filter technique used for film calibration in the visible spectrum[85]. The only difference is that transmission through X-ray absorption filters is wavelength dependent and the spectral distribution of the source needs to be known. Accordingly, the radiation to be studied is first spectrally resolved. The radiation is then passed through a step-wedge absorption filter and recorded on film. The wavelength of each spectral line can be identified and the attenuation in intensity through each channel of the step-wedge filter calculated from tabulated data in the literature. Hence, for an N-channel filter, there will be N different exposures on film for each line, from which a characteristic curve can be composed. The process can be repeated for each spectral line and a set of characteristic curves corresponding to different wavelength can be obtained. In general, these lines all lie within a very narrow spectral range so that the curves can be combined to form one single characteristic curve which is applicable throughout the spectral region of interest. Such a combination process is not absolutely necessary. It will, however, reduce the number of

channels in the step-wedge filter required to provide film exposures covering its full dynamic range since different spectral lines will have different intensities.

A schematic of the experimental set-up is shown in Figure 5 – 9. Laser radiation of wavelength 0.53 μm and pulse duration 2 ns (FWHM) was focussed on planar, solid targets with $f/10$ optics. The angle of incidence was 10° off target normal and the laser intensity on target was about 10^{13} W/cm^2. Targets used include aluminum foils, glass slides and layered targets of polystyrene-on-glass. The X-ray emission from the laser-produced plasma was analysed with a slitless, flat KAP crystal spectrometer (see section 5 – 3 – D) at 15° off target normal. X-rays diffracted by the crystal were recorded on film through a step-wedge absorption filter as shown on Figure 5 – 9. A three-channel step-wedge filter was used for the study of X-rays from silicon plasmas in glass or layered targets. The absorption filter used in each channel is listed in Table 5–1. In this experiment, Kodak SC5 X-ray film[86] was used.

Table 5–1

List of foils used for three-channel step-wedge filter.

channel	filter(s)
1	10 μm Be
2	10 μm Be + 2μm Al
3	10 μm Be + 5μm Al

A typical X-ray spectrum obtained from a single laser shot on a planar glass target is presented in Figure 5 – 10. This shows the silicon spectrum from 5.1 to 7.1 Å. The three intensity bands normal to the dispersion axis correspond to the different exposures due to the three-channel filter. The transmission of the exposed film was measured with a microdensitometer[87]. Linearity of the instrument was verified using a set of calibrated neutral density filters. A microdensitometer scan, made over each exposure band on the film, is shown in Figure 5 – 11. We have arbitrarily defined the signal obtained when no film was placed between the light source and the photomultiplier in the microdensitometer as 100% transmission. The zero level was established by placing an opaque cover in the

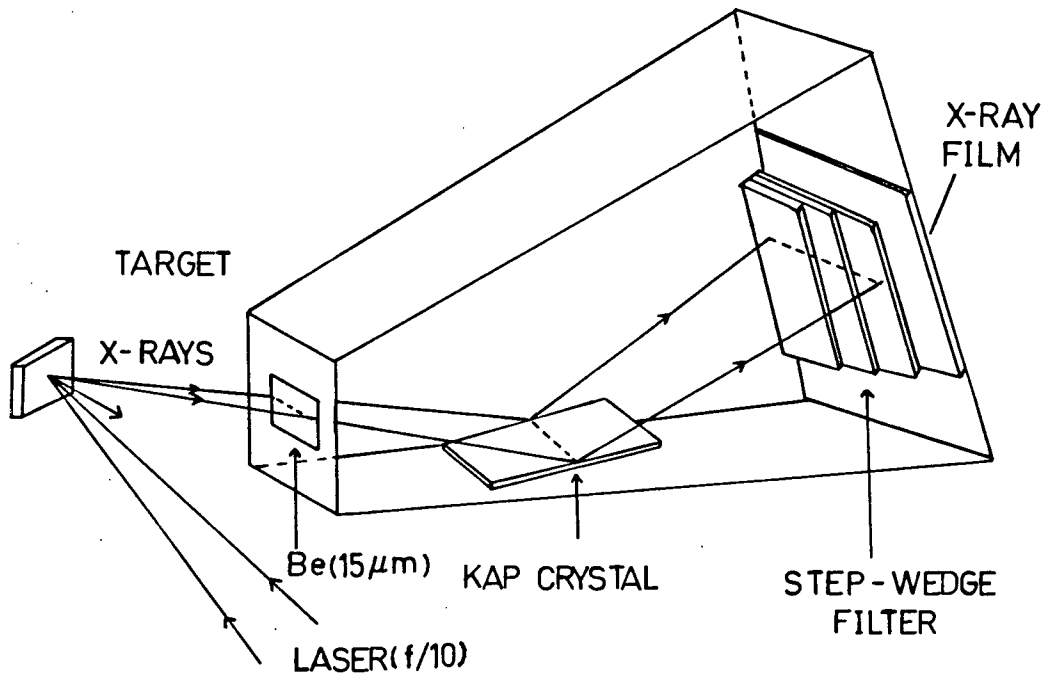

Figure 5-9 Experimental arrangement used in the X-ray film calibration technique.

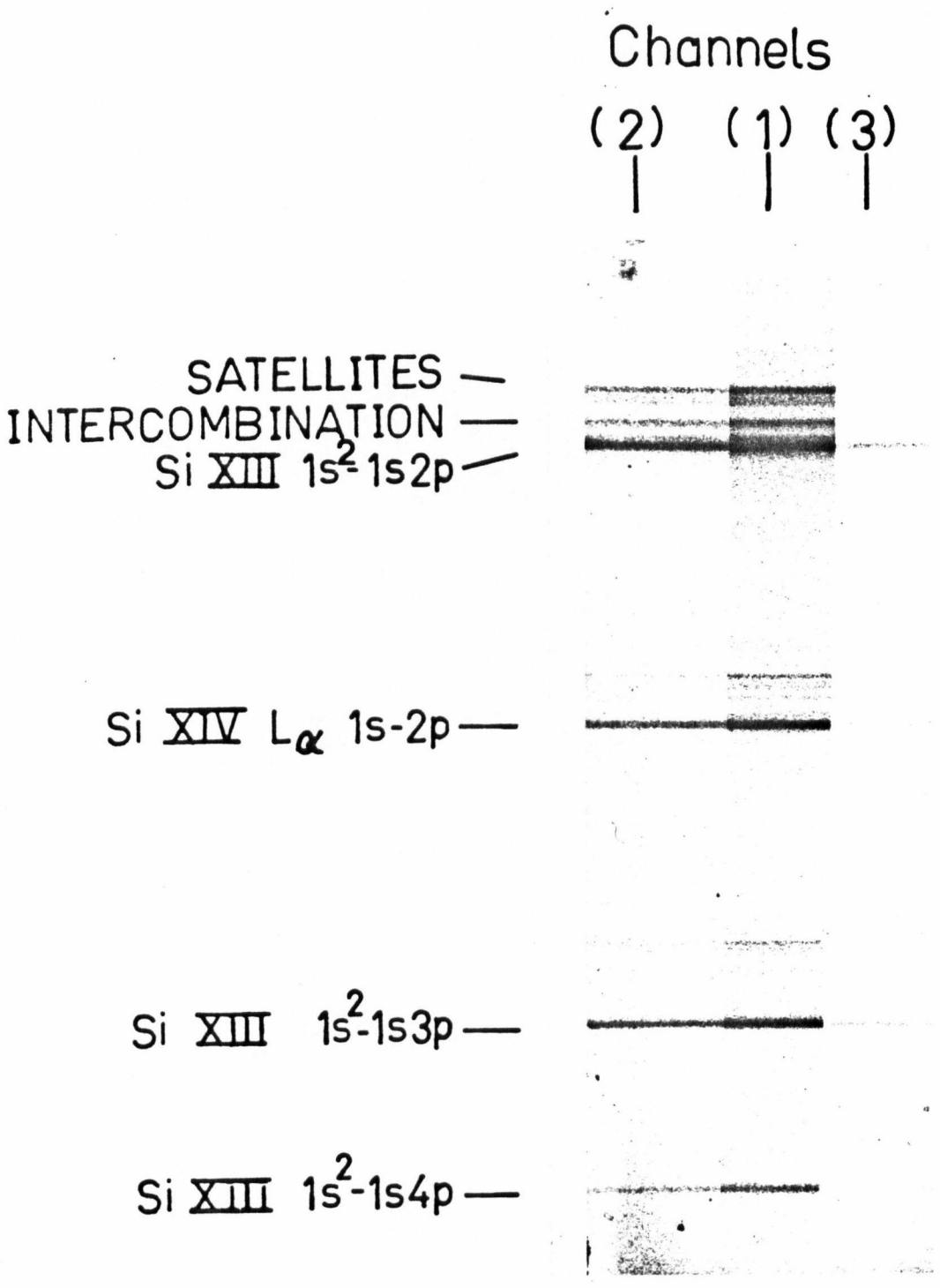

Figure 5–10 Silicon X-ray spectrum obtained with a three-channel step-wedge filter : (1) 10 μm Be, (2) 10 μm Be + 2 μm Al, (3) 10 μm Be + 5 μm Al.

microdensitometer beam path. Transmission through the unexposed part of the film was about 55%.

Four silicon lines have been used for compiling the film characteristic curve. These are (i) Si XIII $1s^2(^1S_0) - 1s4p(^1P_1)$, (ii) Si XIII $1s^2(^1S_0) - 1s3p(^1P_1)$, (iii) Si XIV L_α and (iv) Si XIII $1s^2(^1S_0) - 1s2p(^1P_1)$. For each of these, three different values of film transmission corresponding to three different levels of exposure can be obtained. The relative exposure for a given line depends on the attenuation of intensity of the filters in the various channels. The list of silicon lines used, their wavelength λ and the transmission factor $\exp \sum_i [-\mu_i(\lambda)\rho_i\tau_i]$ in each channel are given in Table 5–2. Here $\mu_i(\lambda)$ is the mass absorption coefficient[88], ρ_i the density and τ_i the thickness of the filter used in each channel. Film transmission as a function of relative exposure can be determined for each spectral line. The results are shown in Figure 5 – 12, unit exposure corresponds to that in Channel 1 (10 μm beryllium filter). As mentioned earlier, because of their difference in intensity, each spectral line give a set of points covering different sections of the characteristic curve. Given that the lines all lie within a narrow spectral range (5.40 to 6.65 Å) it is reasonable to assume that the characteristic curve remains unchanged in this this interval. So, irrespective of their wavelength, the set of data points are shifted along the relative exposure axis to form a single continuous line with a characteristic elongated S-shape. The final curve thus obtained is shown on Figure 5 – 13.

Accuracy of the composite curve depends on the number of channels used in the step-wedge X-ray filter and on the number of spectral lines available for analysis. It also depends on the accuracy of the values of the thicknesses of the X-ray absorption filters and their corresponding mass absorption coefficients and on the accuracy of the microdensitometer used.

5–3–E–ii *Evaluation of technique*

In general, once the characteristic curve is obtained it can be used to determine the relative intensity distribution of the X-ray spectrum recorded by the film. The technique therefore serves as an ***in-situ*** calibration which is obtained simultaneously with the data.

The calibration technique was used in a preliminary investigation of electron thermal energy transport in laser produced plasmas. The principle of the latter measurement

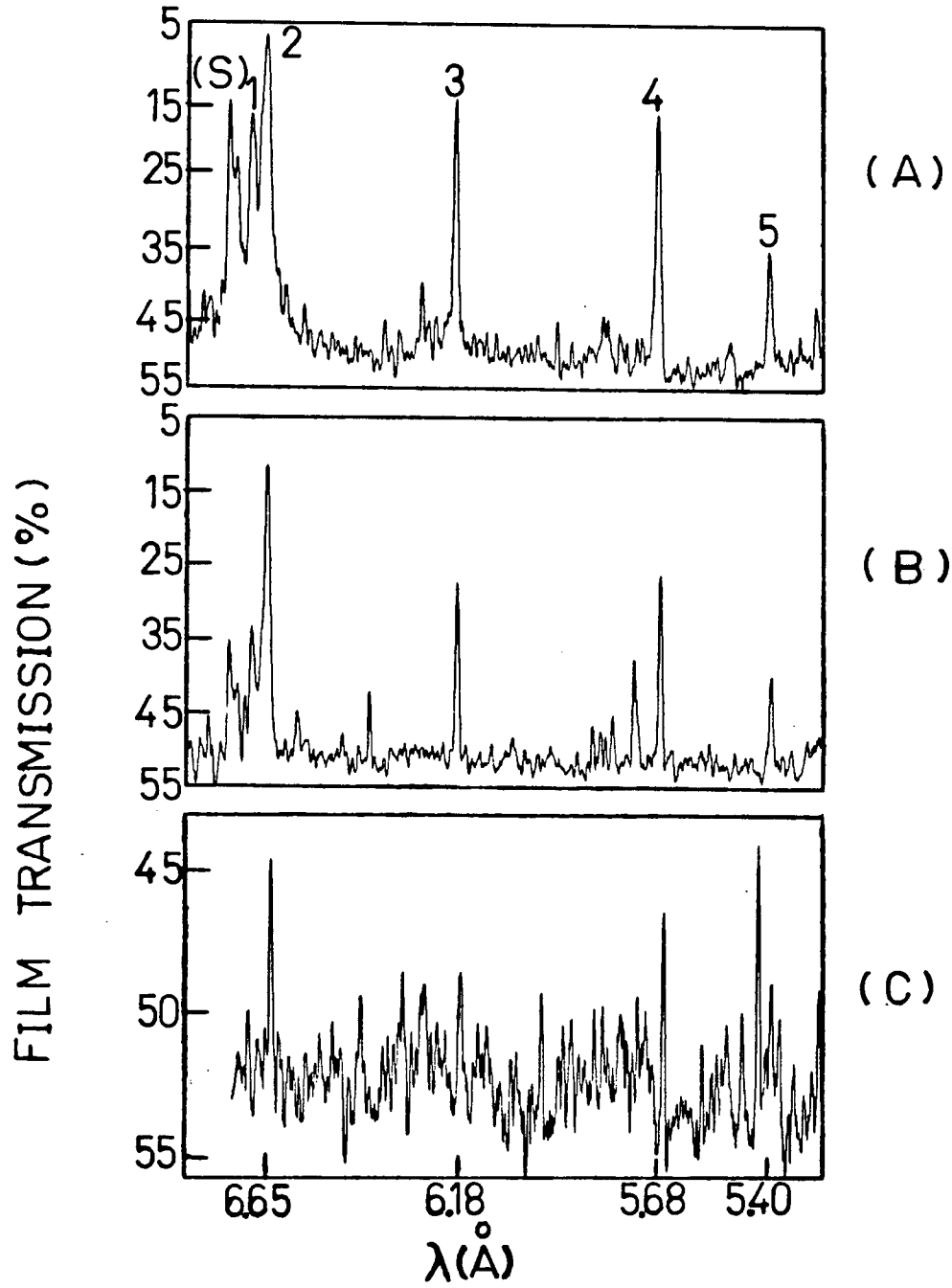

Figure 5–11 Silicon spectrum transmitted through different filters : (a) 10 μm Be, (B) 10 μm Be + 2 μm Al, (C) 10 μm Be + 5 μm Al. (S) satellites, (1) Si XIII $1s^2(^1S_0) - 1s3p(^3P_1)$. (2) Si XIII $1s^2(^1S_0) - 1s2p(^1P_1)$. (3) Si XIV L_α. (4) Si XIII $1s^2(^1S_0) - 1s3p(^1P_1)$ and (5) Si XIII $1s^2(^1S_0) - 1s4p(^1P_1)$.

Table 5–2

List of silicon lines used for constructing the calibration curve and their transmission factors through the different channels

Spectral line	λ(Å)	Transmission: $\exp \sum_i [-\mu_i(\lambda)\rho_i\tau_i]$		
		channel 1 10 μm Be	channel 2 10 μm Be + 2 μm Al	channel 3 10 μm Be + 5 μm Al
Si XIII $1s^2 - 1s4p$	5.405	0.915	0.382	0.103
Si XIII $1s^2 - 1s3p$	5.681	0.903	0.331	0.074
Si XIV L_α	6.182	0.878	0.249	0.038
Si XIII $1s^2 - 1s2p$	6.649	0.848	0.185	0.019

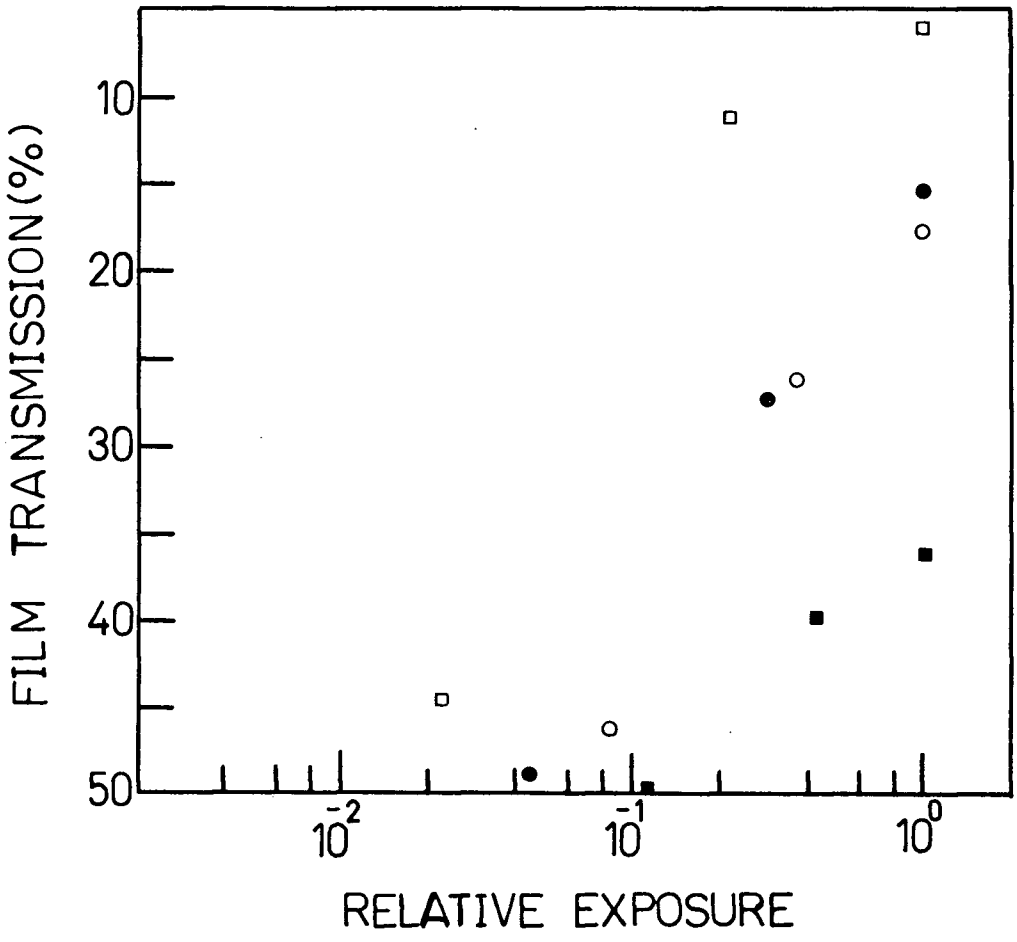

Figure 5–12 Film transmission % for the four silicon lines used. Exposure is normalized to the exposure in channel (1) 10 μm Be; (□) Si XIII $1^2 - 1s2p$; (●) Si XIV L_α;(○) Si XIII $1^2 - 1s3p$; (■) Si XIII $1s^2 - 1s4p$.

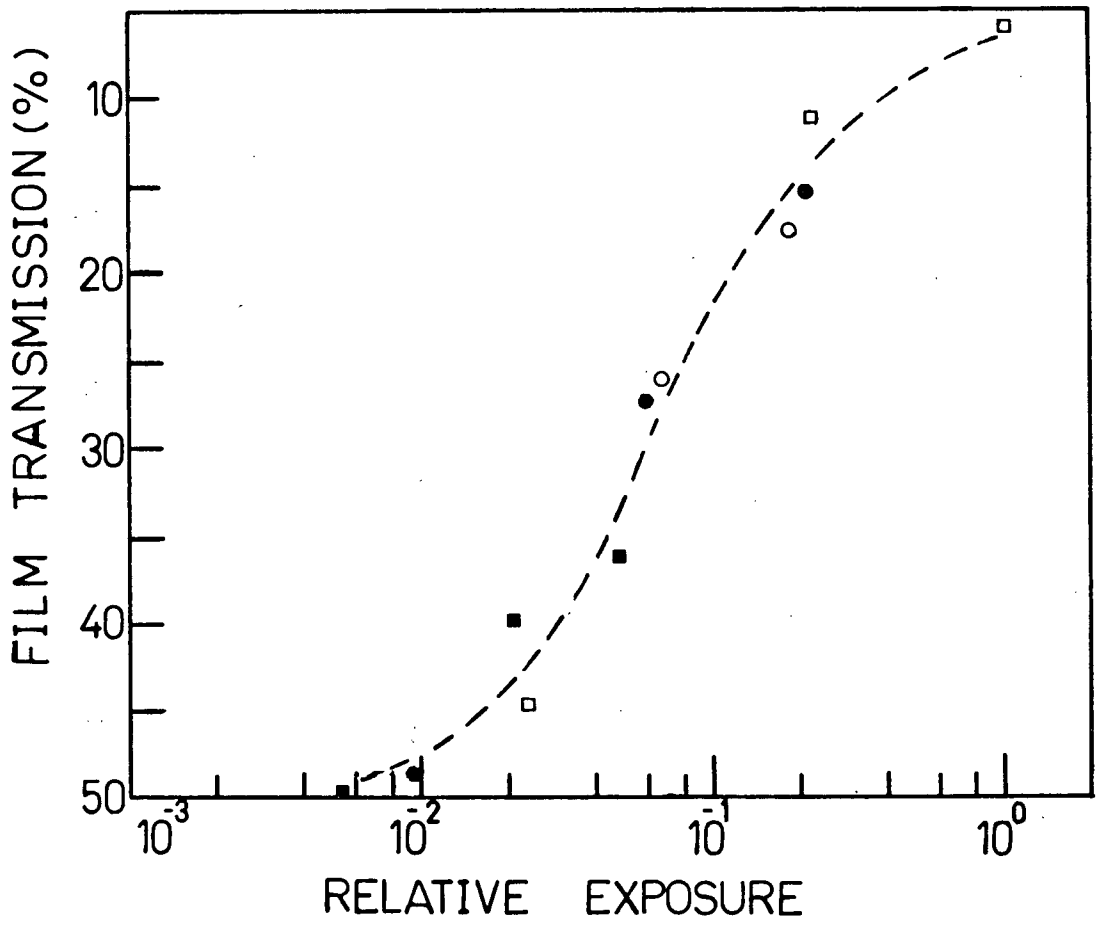

Figure 5–13 Relative intensity calibration obtained with a silicon spectrum.

together with more complete results are given in Chapter 7. Here we briefly describe this measurement as an independent evaluation of the film calibration technique. Glass slide targets coated with different thicknesses of polystyrene were irradiated with 0.53 μm laser light. In this experiment we monitored the silicon spectrum (5.1 to 7.1 Å) emitted. As the CH layer thickness was increased, intensities of the silicon lines decreased and eventually disappeared. The experimental set-up was similar to that in Figure 5 – 9. In addition to using the X-ray film to record the silicon spectrum, an X-ray PIN diode[89] was also used to provide an independent measurement. However, the PIN diode only monitered the group of silicon lines centered around 6.7 Å. These included the Si XIII $1s^2(^1S_0) - 1s2p(^1P_1)$ resonance line at 6.65Å, the intercombination line at 6.69 Åand the satellite lines from 6.6 to 6.74 Å (see Figure 5 – 10). The integrated intensity of this group of silicon lines measured by the X-ray film and the diode as a function of CH layer thickness is presented in Figure 5 – 14. Intensities recorded by the film were analysed using the calibration technique described above. The results show good agreement with that obtained using the diode.

As pointed out above, accuracy of the film characteristic curve obtained using this technique depends on the number of channels used in the step-wedge X-ray filter and the number of spectral lines available for analysis. As a further demonstration of the technique, we have also obtained a relative intensity calibration using a four-channel filter and six spectral lines from aluminum plasmas. For this measurement, the absorption foils used in each channel of the step-filter are shown in Table 5–3 and the spectral lines used, their wavelengths and the transmission factor in each channel are listed in Table 5–4. A typical aluminum spectrum recorded on film is presented in Figure 5 – 15. Figure 5 – 16 shows the film transmission as a function of relative exposure for each spectral line, with the relative exposures normalized to unity. A composite curve can then be obtained as shown in Figure 5 – 17. Evidently, this provides a more detailed measurement of the film characteristic curve. It is in good agreement with that obtained trom the silicon line spectrum (Figure 5 – 13).

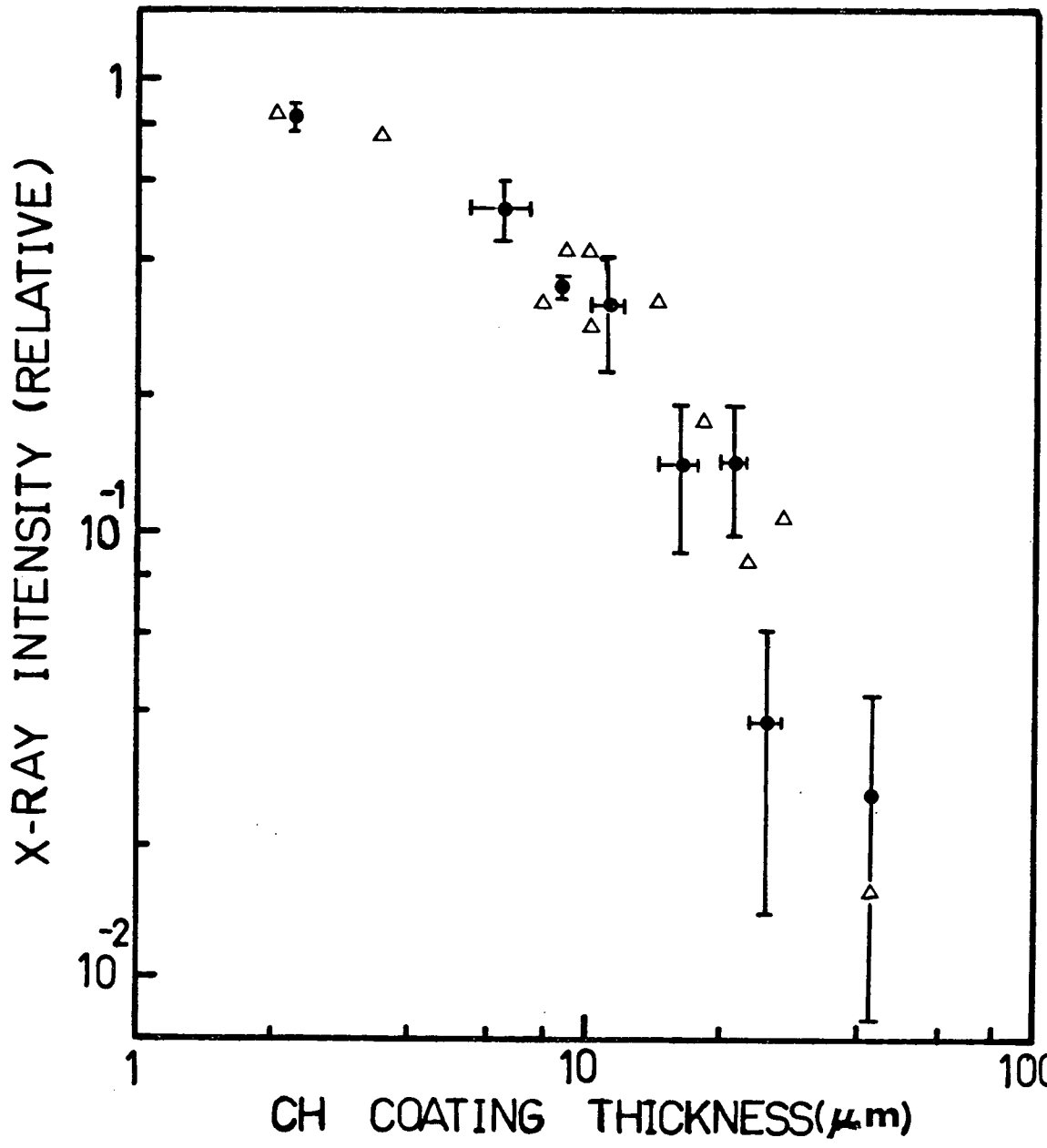

Figure 5–14 Intensity of a group of silicon lines as a function of CH thickness.

Table 5–3

List of foils used for four-channel step-wedge filter.

channel	filter(s)
1	15 μm Be
2	15 μm Be + 2μm Al
3	15 μm Be + 4μm Al
4	15 μm Be + 6μm Al

Finally, this technique can also give an absolute film calibration since the film exposures are correlated with signals from PIN diodes whose absolute response can be calibrated independently.

5–3–F X-ray pinhole camera

X-ray images of the laser-target interaction in our experiment were obtained using pinhole cameras. In an X-ray pinhole camera a small hole in an otherwise opaque substrate is used to provide two-dimensional imaging. The geometric resolution of a pinhole camera is given by[90]

$$d = D(1 + 1/M) \qquad (5-3)$$

where d is the spatial resolution of the pinhole camera, D is the diameter of the pinhole, and M is the magnification (the camera magnification is given by the ratio of the image distance from the pinhole to the object distance to the pinhole).

Figure 5 – 18 shows an X-ray pinhole photograph of the plasma produced in our experiments. This particular image was obtained by irradiating 50 μm thick aluminum foil target with 1.45 joule of 0.355 μm laser light. The pinhole camera was positioned at 5° from target normal. Imaging was obtained using a 15 μm diameter pinhole covered with a 10 μm beryllium filter. Kodak SC5 X-ray film, calibrated with the technique described in section 5 – 3 – E was used for the measurement. The image magnification on the film was

Table 5–4

List of aluminum lines used for constructing the calibration curve and their transmission factors through the different channels.

Spectral line	λ(Å)	Transmission: $\exp\sum_i[-\mu_i(\lambda)\rho_i\tau_i]$			
		channel 1 15 μm Be	channel 2 15 μm Be + 2 μm Al	channel 3 15 μm Be + 4 μm Al	channel 4 15 μm Be + 6 μm Al
Al XIII L_γ	5.739	0.854	0.314	0.116	0.043
Al XIII L_β	6.052	0.833	0.261	0.082	0.026
Al XII $1s^2 - 1s5p$	6.175	0.821	0.237	0.068	0.020
Al XII $1s^2 - 1s4p$	6.314	0.8312	0.223	0.061	0.017
Al XII $1s^2 - 1s3p$	6.635	0.786	0.178	0.040	0.009
Al XIII L_α	7.172	0.727	0.122	0.020	0.003

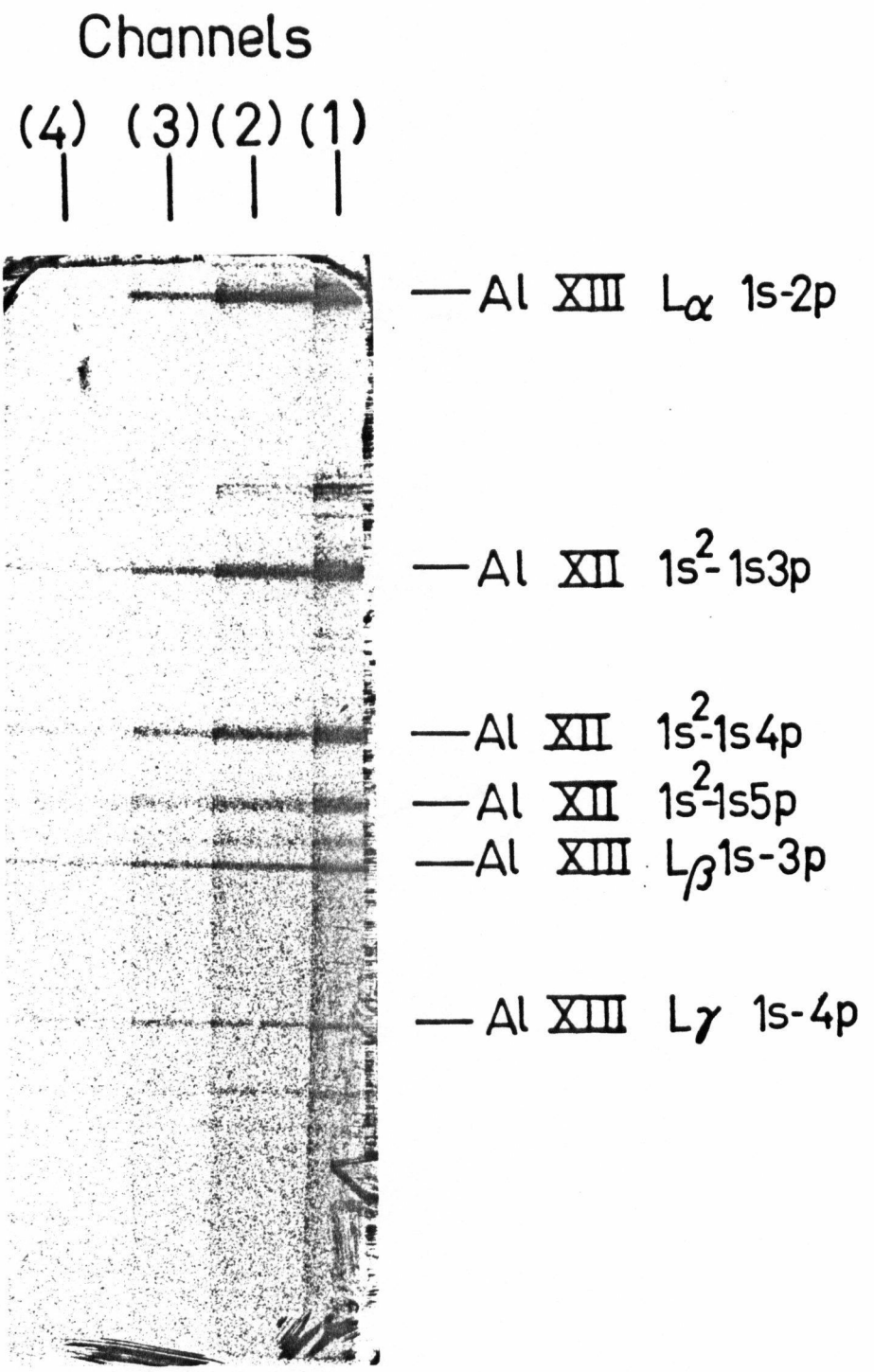

Figure 5–15 Aluminum X-ray spectrum obtained with a four-channel step-wedge filter.

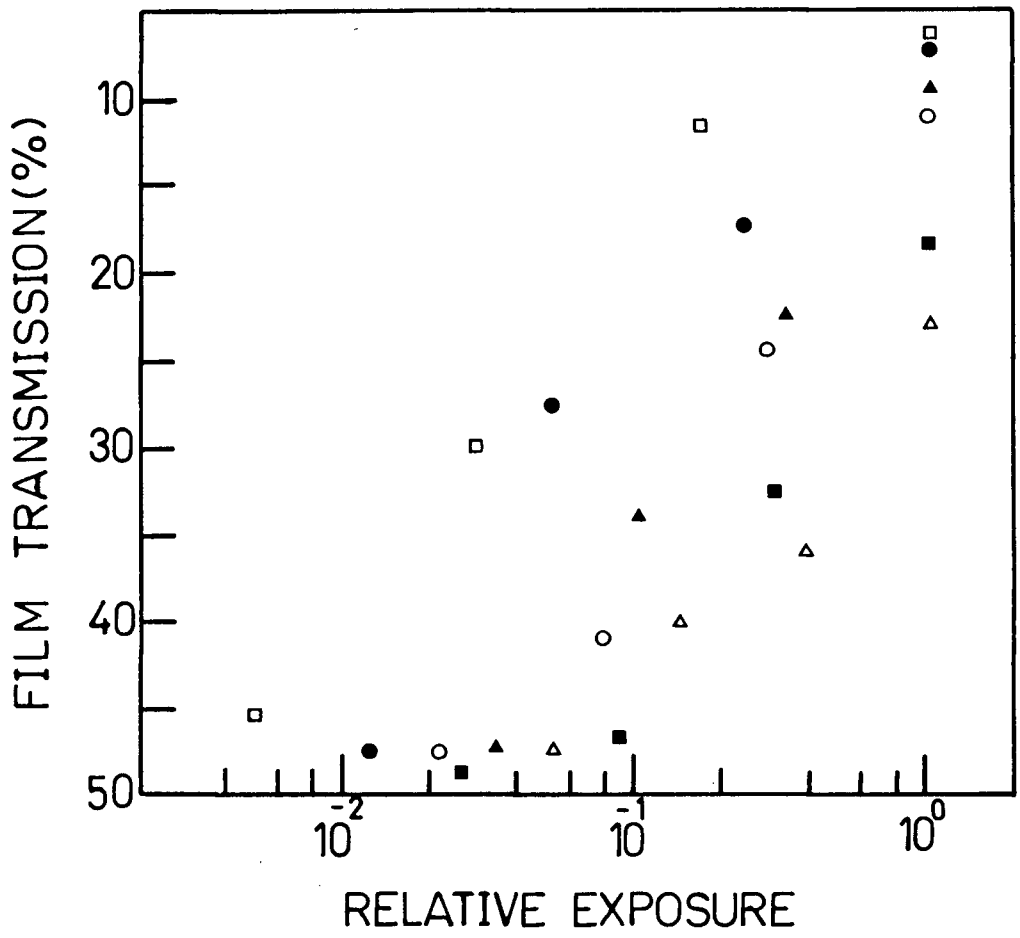

Figure 5–16 Film transmission (%) for each channel for the six aluminum lines used. Exposure is normalized to the exposure in channel (1) 15 μm Be; ( ) Al XIII L_α; ( ) Al XII $1^2 - 1s3p$; ( ) Al XII $1s^2 - 1s4p$; ( ) Al XIII L_β; ( ) Al XII $1s^2 - 1s5p$; ( ) Al XIII L_γ.

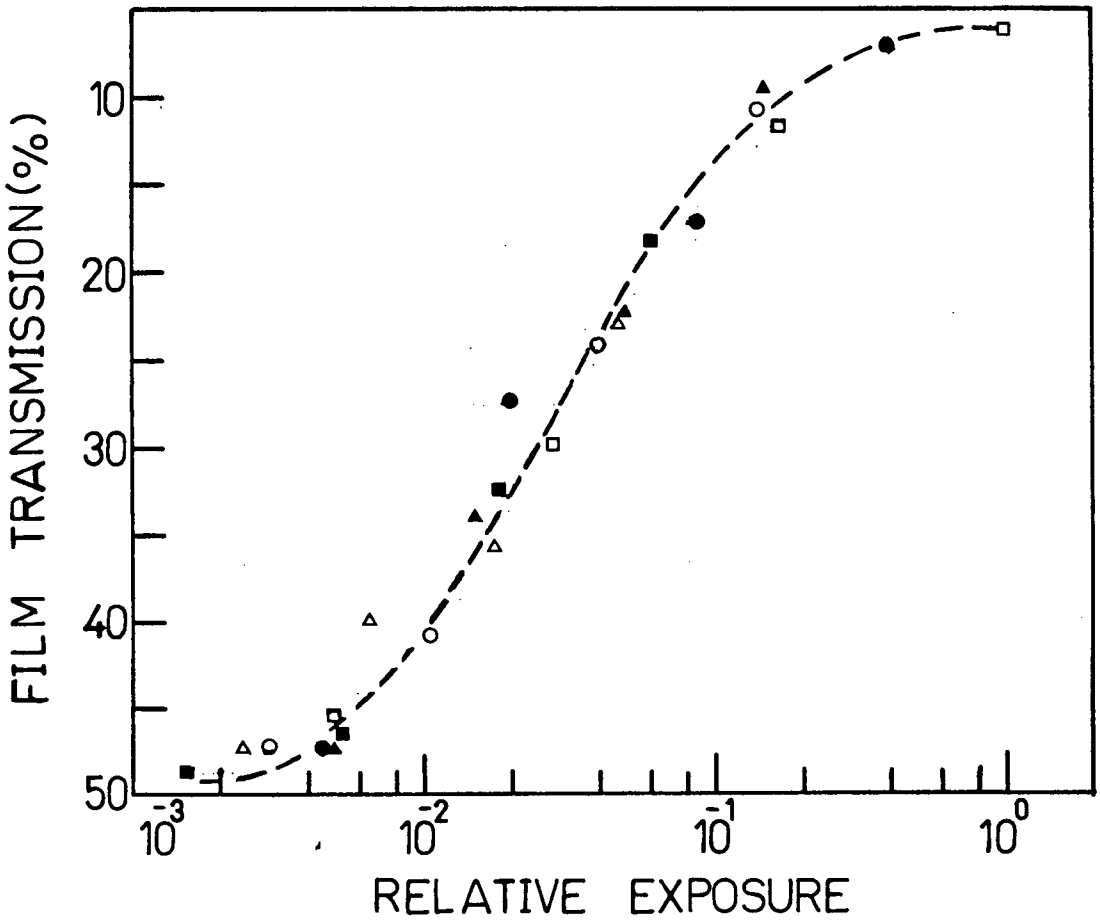

Figure 5–17 Relative intensity calibration curve obtained with an aluminum spectrum.

5.7 . This together with the pinhole size yielded a spatial resolution of 18 μm. Only X-ray with energies greater than 1 Kev (12.4 Å) were transmitted by the X-ray filter. The X-ray image of Figure 5 – 18 shows a circular uniform region of X-ray emission. Also shown on this Figure is a microdensitometer scan of the image across its diameter. Analysis shows that the diameter of the X-ray emission region at the 0.1 intensity points is approximately 32 μm. This indicates that the X-ray emission is mainly coming from that part of the target irradiated by the high intensity central region of the focal spot. For the quantitative analysis of the X-ray image it was necessary to use the X-ray film in its linear response region. When the X-ray film is operated in its saturation region even the low intensity X-ray radiation emitted by the peripheral plasma appears on the X-ray image. This can be seen in Figure 5 – 19. This pinhole photograph was obtained for experimental conditions very similar to that of Figure 5 – 18, except in this case, the camera magnification was only 2.1, increasing the X-ray intensity on the film. From the microdensitometer scan of the X-ray image the maximum size of the X-ray emission region is estimated to be 155 μm in diameter.

In figure 5 – 20 a series of X-ray images of the plasma using two pinhole cameras is shown. For this series of pictures, thin strips (1 mm wide) of aluminum foils of different thicknesses were irradiated with 3 joules of 0.532 μm laser light. One pinhole camera was facing the plasma at target normal, while the other camera was viewing the target edge-on. The front side camera had a 15 μm pinhole and a 5 μm aluminum filter and the other one had a 10 μm pinhole and a 10 μm beryllium filter. In both cases the camera magnification was approximately two. To obtain a high contrast image the Kodak SC5 X-ray film employed was used in its saturation region. In this series of pictures we clearly see a plasma developing at the back of the target even for aluminum foil as thick as 9 μm. This was attributed to the rapid two dimensional expansion of the foil (because of the small focal spot used in our experiments) after it has been traversed by a shock wave. The laser light can then propagate into the rarefied target material which is transformed into a hot X-ray emitting plasma. For most of our experiments 50 μm thick aluminum foil were used to eliminate the effect of target disassembly on the measurements.

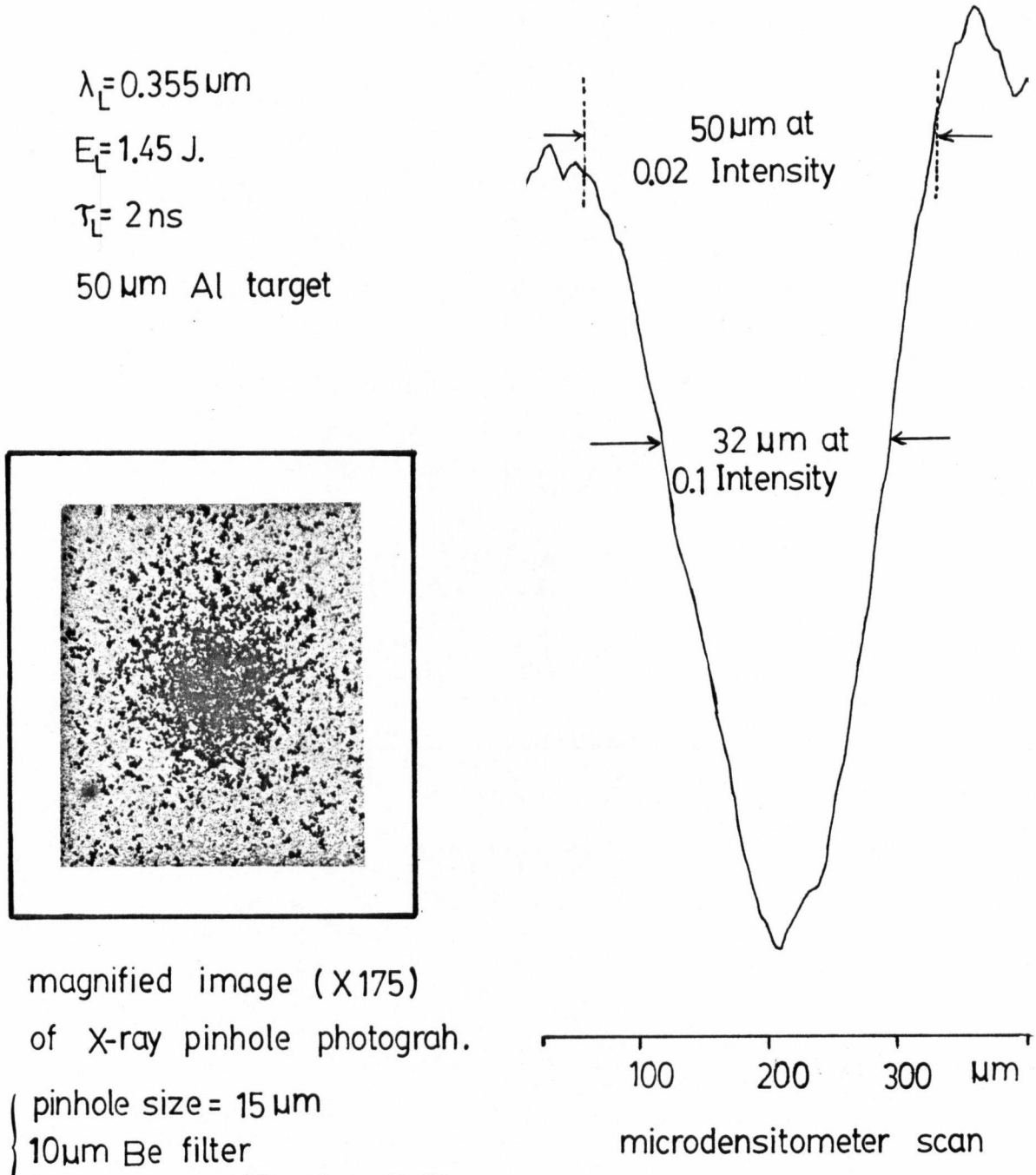

Figure 5–18 X-ray pinhole photograph of the plasma.

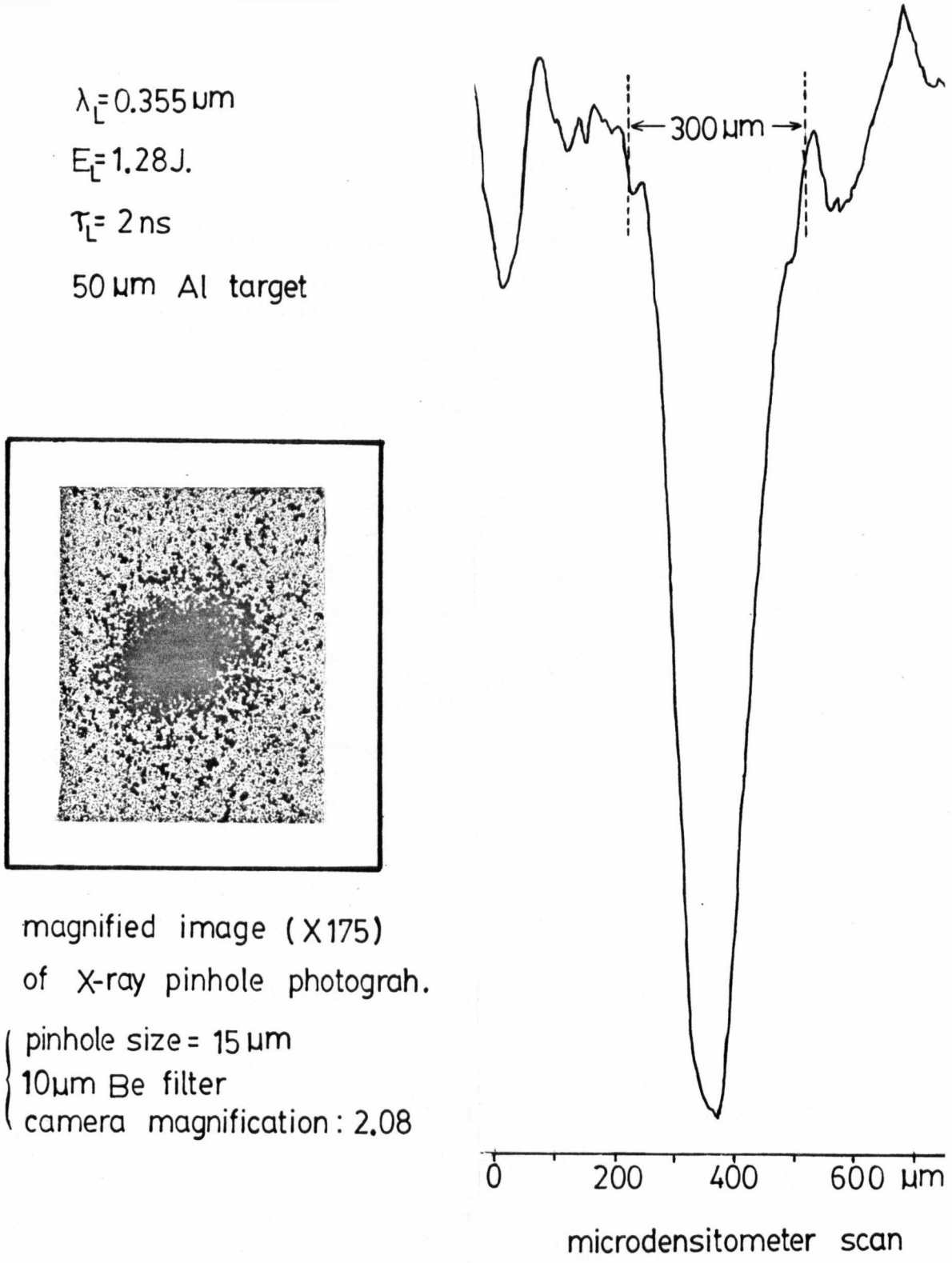

Figure 5–19 X-ray pinhole photograph of plasma. The film is saturated showing the full size of the X-ray emission region.

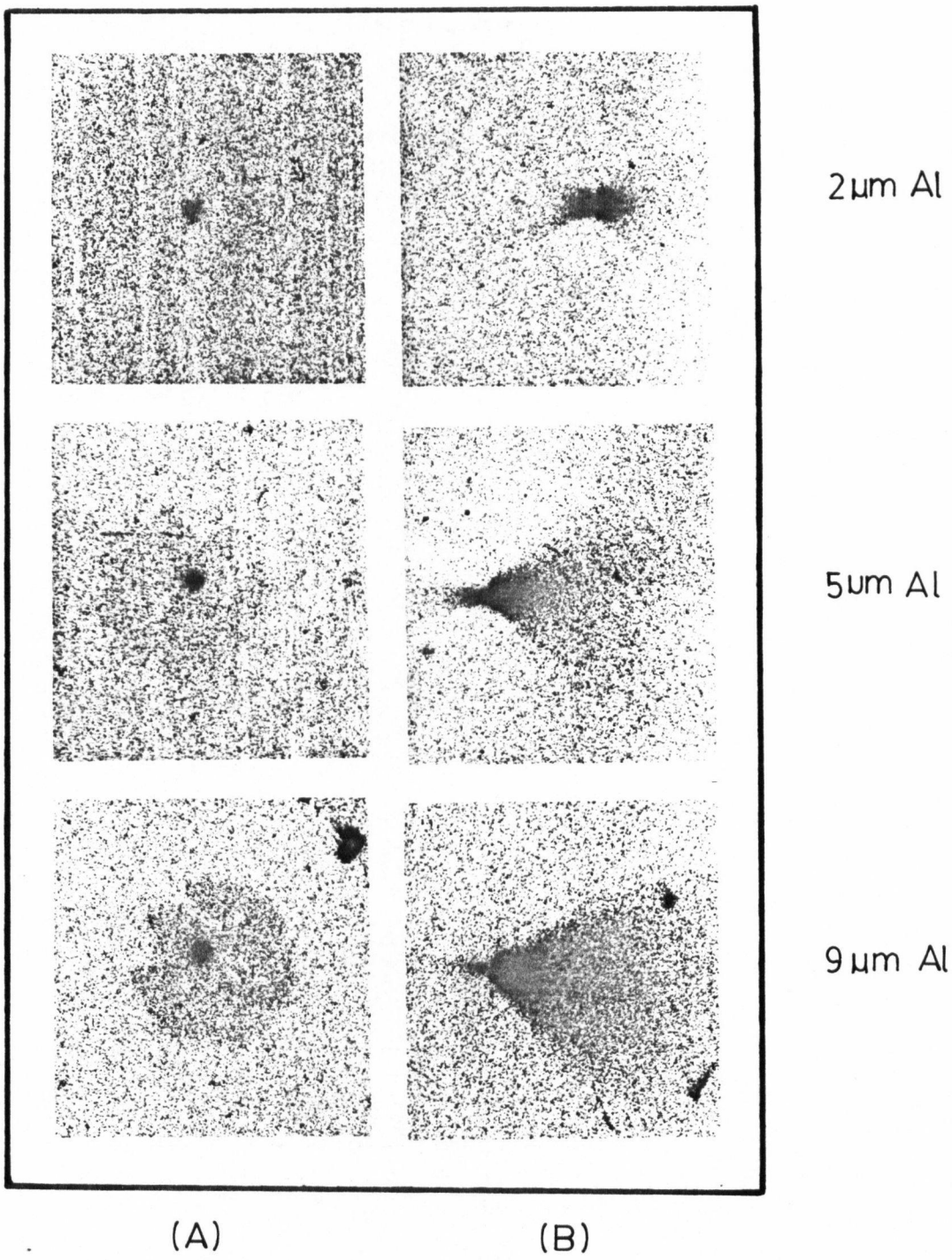

Figure 5–21 Series of X-ray pinhole photograph obtained by irradiating thin strip (1mm wide) of aluminum foils of different thicknesses. (A) camera facing tha plasma at target normal, (B) camera viewing the target edge-on. The laser is coming from the right. $\lambda_L = 0.532\,\mu$m, $E_L = 3$J.

5–3–G Multichannel X-ray detector

In experimental studies of laser plasma interactions, it is of great interest to monitor the plasma electron temperature in every laser shot on a target. Such a diagnostic may provide information on laser absorption and plasma heating mechanisms. For these high temperature plasmas the X-ray continuum has been commonly used to determine the electron temperature[91]. Typically, the X-rays emitted are measured using either a single detector (such a PIN diode or a scintillator-photomultiplier combination) scanning the X-ray spectrum for different shots, or an array of detectors, each of which monitors simultaneously X-rays of a particular energy. The single detector method is relatively simple and inexpensive, but data must be taken over many laser shots in order to obtain a spectrum. The multi-detector array method, on the other hand, can yield an electron temperature measurement in a single shot and can be used for an on-line diagnostic system. Yet, such an array also has several disadvantages, namely, (i) the large number of individual detectors and recording devices implies complexity and high system cost, and (ii) the size of the array makes the measurement particularly sensitive to angular anisotropy of X-ray emission from the plasma.

We have developed a simple electron temperature monitor[70] which consists of a step-wedge X-ray filter and a charge-coupled device (CCD), modified to be sensitive to X-rays. This monitor offers the advantages of (i) compactness, (ii) simplicity of operation, (iii) versatility in the number and configuration of different X-ray channels and (iv) relatively low cost.

$5-3-G-i$ *System design*

The electron temperature monitor is basically a multichannel X-ray analyser. The different energy channels are defined by the steps of a step-wedge X-ray filter. Such a filter can be fabricated by stacking foils (beryllium or aluminum, for example) of varying length and thicknesses (Figure $5-21-A$). This filter is then matched to the X-ray sensor, an EG&G Reticon RL512S[92]. To achieve the desired X-ray sensitivity in the energy range of 1-10 KeV, the thickness of the SiO_2 layer over the silicon diode elements is limited to 1 μm. The Reticon is a self-scanning array of 512 discrete photodiode elements. Center-to-center spacing of the diode elements is 25 μm, and the aperture height of each element is 2.5 mm.

The large aperture height is chosen to provide high output. The X-ray response[92] of such an array is shown in Figure 5 – 21 – B. The internal functions of the Reticon array can be divided into two essential parts: the photodiode array and the shift registers. The charge produced on each photodiode element is proportional to the integrated radiation intensity impinging on the photodiode sensitized surface. Under normal operation (video mode) the accumulated charge on each photodiode element is transferred simultaneously into its associated shift register element by a transfer pulse ("start pulse" in the EG&G literature[92] from an external clock). The charges in the shift register elements are then scanned out serially after the trailing edge of the transfer pulse. An integration circuit[92] (EG&G RC 1024) further provides a sample-and-hold output waveform with improved dynamic range.

Since the CCD is self-integrating, its dark current will cause saturation of the light sensitive elements in approximately 0.5 second. The device has to be continuously cleared to eliminate such saturation. In order to process single-shot events (eg. laser shots) an additional circuit is required to provide synchronization between the laser pulse, the video output of the array and the recording instrument. The synchronization circuit* is shown in Figure 5 – 22 – A and the associated timing diagram in Figure 5 – 22 – B. It is allowed to run in a continuously scanning mode with a scan frequency of 250 kHz. The timing of the laser pulse is asynchronous with the scanning of the Reticon array. A photodiode picks up part of the laser light and sets a latch "A" whose output raises the data input of the D-type flip-flop "B". Simultaneously, the charges produced by impinging X-rays from the laser-induced plasma are stored in the diode array elements for time interval Δt_1. These charges are then transferred into the associated registers by the transfer pulse (time interval Δt_2). The trailing edge of the transfer pulse is used to clock the flip-flop "B" and to reset the latch "A". At the same time the internal circuitry of the Reticon board activates the scanning clock and the video information is scanned out (time interval Δt_3). Flip-flop "B" is reset by the end-of-line (EOL) pulse generated by the Reticon board. Hence, a pulse which is time coincident with the video output appears as the output of "B" in the scan period immediately after the laser pulse. This synchronization pulse is at present used to trigger a storage oscilloscope which displays the video waveform from the array.

* Designed by K. Fong

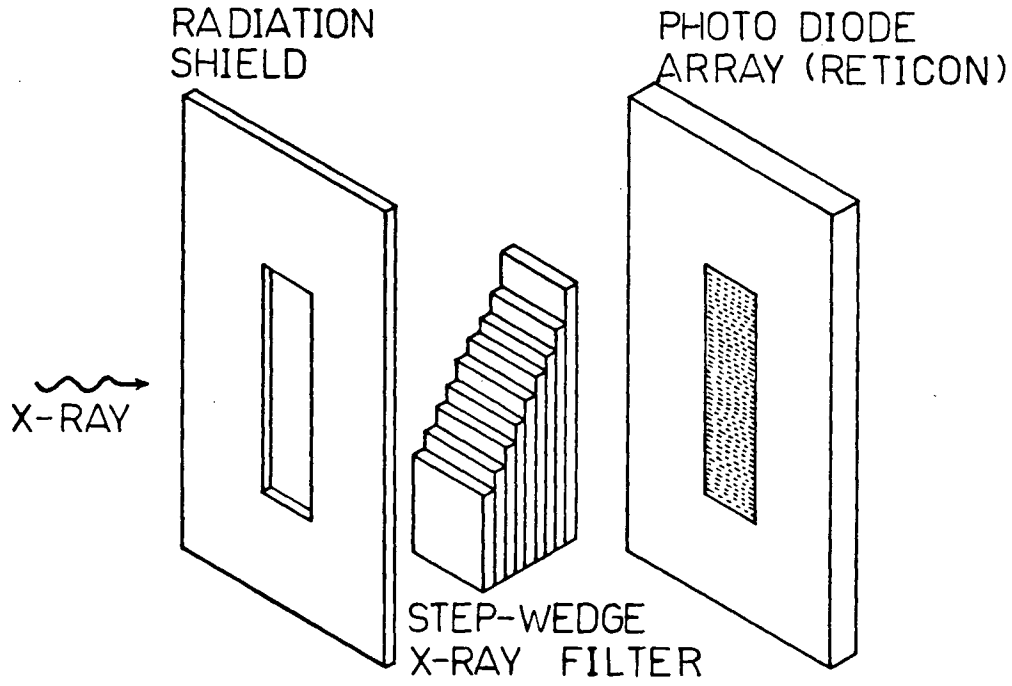

(A)

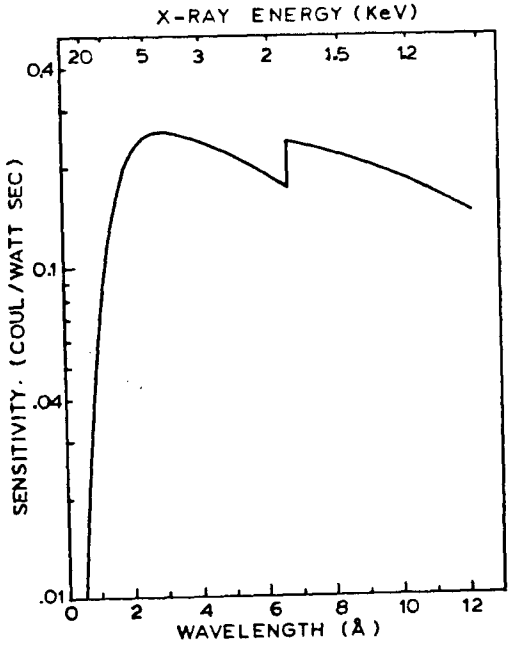

(B)

Figure 5-21 (A) Schematic diagram of the electron temperature monitor. (B) Theoretical X-ray response of the Reticon array.

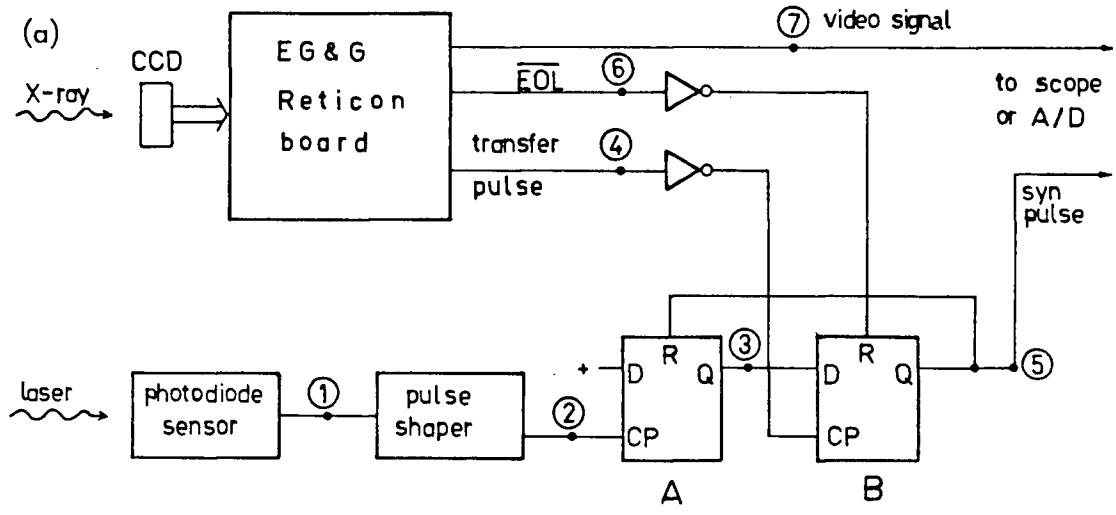

(A)

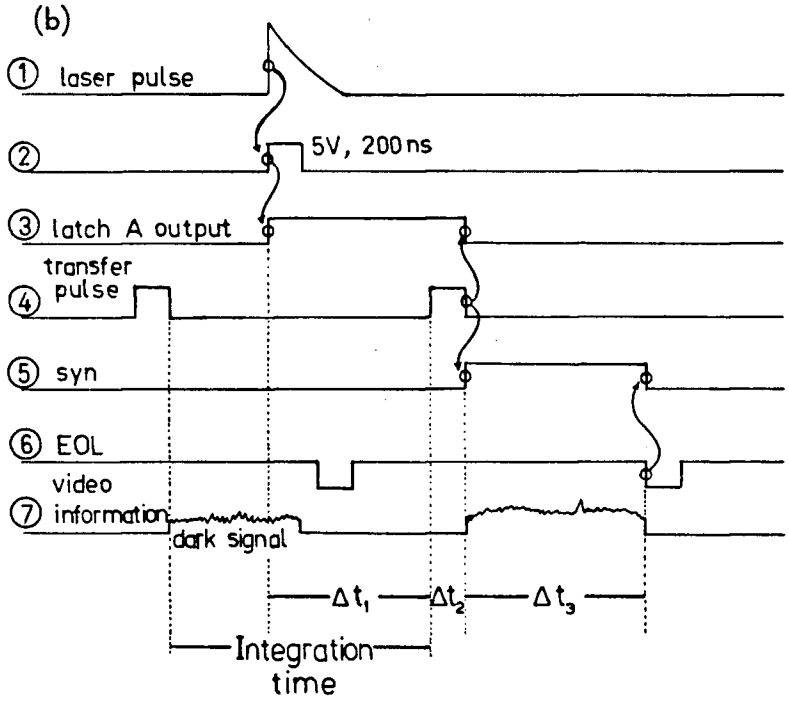

(B)

Figure 5–22 (A) Block diagram of synchronization circuit. (B) Timing sequence of synchronozation circuit.

5 – 3 – G – *ii System calibrations*

Two calibrations have to be made before the system can be used for electron temperature measurements: (i) relative response of the Reticon photodiode elements and (ii) linearity of the response. These calibrations were performed using X-rays produced from the irradiation of aluminum foil targets (25 μm thick) with 0.53 μm laser radiation of 2 ns (FWHM) pulse duration. Laser intensities on target were varied between 10^{12} and 10^{13} W/cm^2.

For the calibration of the relative X-ray response of the Reticon elements, the step-wedge was replaced with a single beryllium filter 10 μm thick, which corresponds to a cut-off energy ϵ of 1 keV (ϵ is defined by $K(\epsilon)d = 1$, where $K(\epsilon)$ is the absorption coefficient as a function of ϵ and d the absorber thickness). Results of the measurement are shown in Figure 5 – 23 – A in which the output signal from each element is displayed. The rising and falling edges correspond to the first and last exposed elements, respectively. The radiation shield (see Figure 5 – 21 – A) blanks off approximately 30 elements at each end of the linear array. Evidently, the response is flat to within $\pm 5\%$ accross the entire length of the array used.

To measure the linearity of response, a 9-channel step-wedge filter was used in the electron temperature monitor. The filter was obtained by stacking on top of a beryllium support foil (10 μm thick) one 5 μm and eight 2 μm thick aluminum foils. The resulting X-ray filters in the different channels are listed on Table 5-5.

Table 5–5

X-ray filters for various channels of
the electron temperature monitor

Channel No.	1	2	3	4	5	6	7	8	9
Al filter (μm)	5	7	9	11	13	15	17	19	21
Be filter (μm)	10	10	10	10	10	10	10	10	10

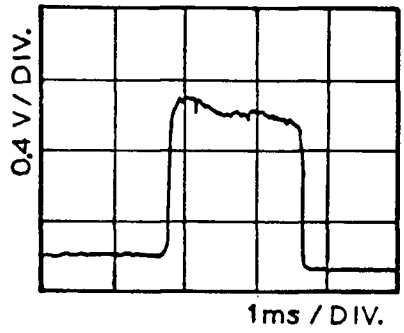

(A)

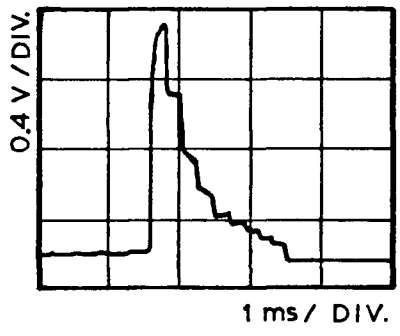

(B)

Figure 5–23 (A) Relative response of diode elements of the Reticon array. (B) Output waveform for a nine-channel electron temperature monitor.

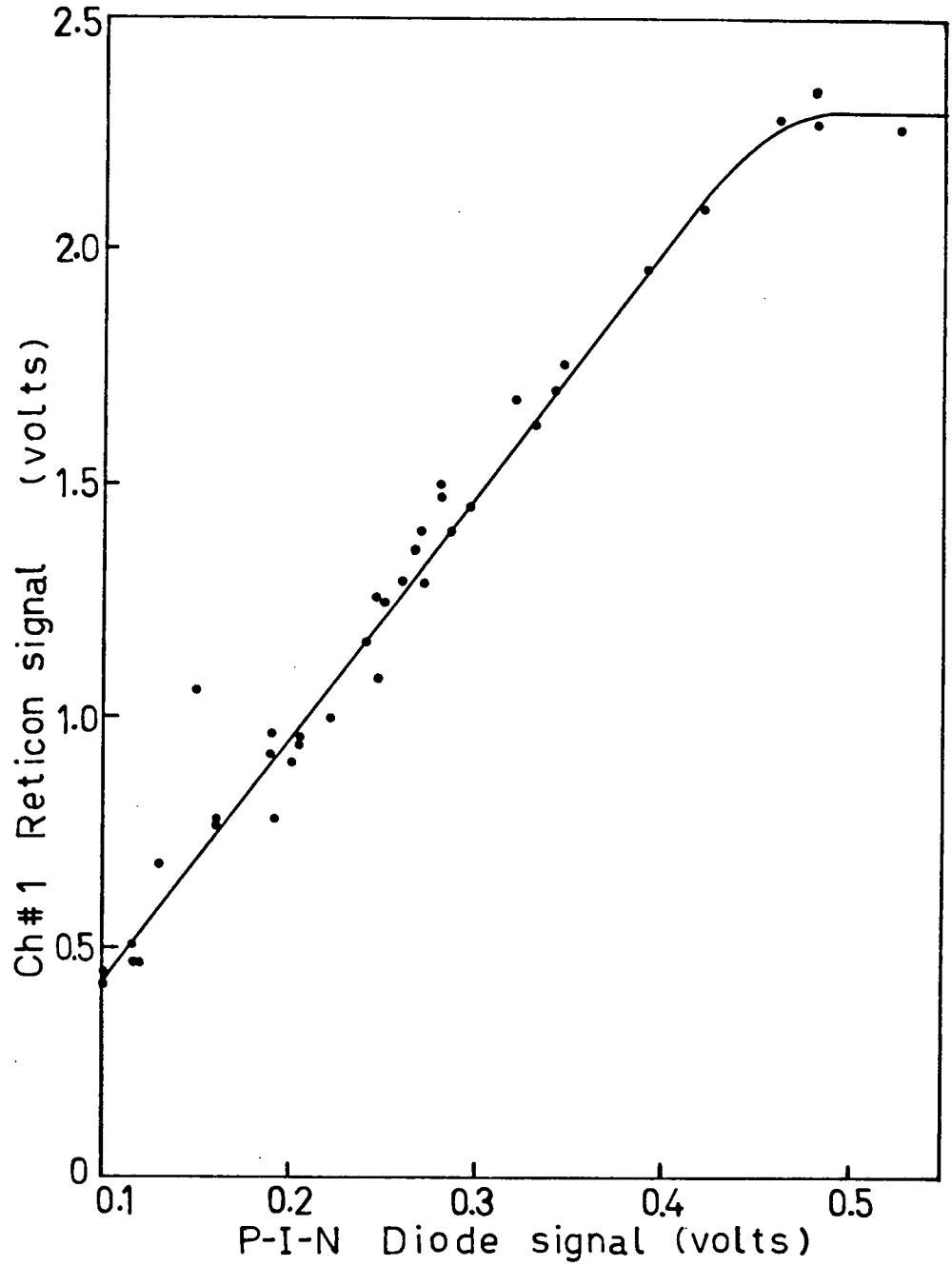

Figure 5–24 Linearity of response of the Reticon detector.

Each channel extends over approximately 50 photodiode elements in the Reticon array.

A typical output waveform, representing the X-ray signals in the nine channels of the monitor, is shown in Figure 5−23−B. The X-ray emission was also measured simultaneously by three PIN diodes (Quantrad 100-PIN-250) with aluminum filters of 18.5, 37.5 and 50 μm respectively. These PIN diodes are linear for output signals up to 30 volts. The linearity of the 9-channel system is demonstrated in Figure 5 − 24 in which the output signals from channel 1 are plotted against that from the PIN diode with a 50 μm aluminum filter. The response of the array is therefore linear for output signals up to 2.3 volts. With an observed noise level of 10 mv due to transient switching noise this corresponds to a dynamic range of 230 to 1. In our experiment the detector was used to measure the dependence of the electron plasma temperature on laser intensity. The results of these measurements are given in Chapter 6.

5–4 Multilayer target fabrication

In Chapter 7 we discuss an investigation of electron energy transport using multilayer targets. The target fabrication procedure is described here.

5 − 4 − A *Fabrication of CH-glass multilayer targets*

For the fabrication of plastic film (CH) targets, we used a technique described in reference 94. It is schematically represented on Figure 5 − 25. The plastic solution was prepared by dissolving polystyrene[95] into toluene. Glass slides (130 μm thick) were held vertically in the solution by spring clips. The solution was then allowed to drain away through the tap (Figure 5 − 25). The initial level of the film solution in the funnel was arranged to be well above the top of the glass slides so that steady flow conditions were achieved before the meniscus reached the specimen. The rate of fall of liquid level down the length of the glass slide is approximately constant and this results in a fairly uniform film. Various film thicknesses ranging from less than a 1 μm to more than 100 μm were obtained by changing the concentration of the film solution and repeating the coating procedure. Rapid drying of the film coating with a heat gun was found to be a good technique to obtain good quality

coating. The film thicknesses were then measured using a Talysurf stylus instrument, or for the thicker film a digital micrometer.

5 – 4 – B *Fabrication of Mg-, Sn-, Ag- and Au-glass multilayer targets*

The metallic coating targets were made by an evaporation technique. The coating thickness was monitored during the evaporation process using a crystal thickness monitor. It was difficult to obtain film thicker than 3 μm during one evaporation run and repeated procedure was necessary to produce the thicker film necessary for some of our targets.

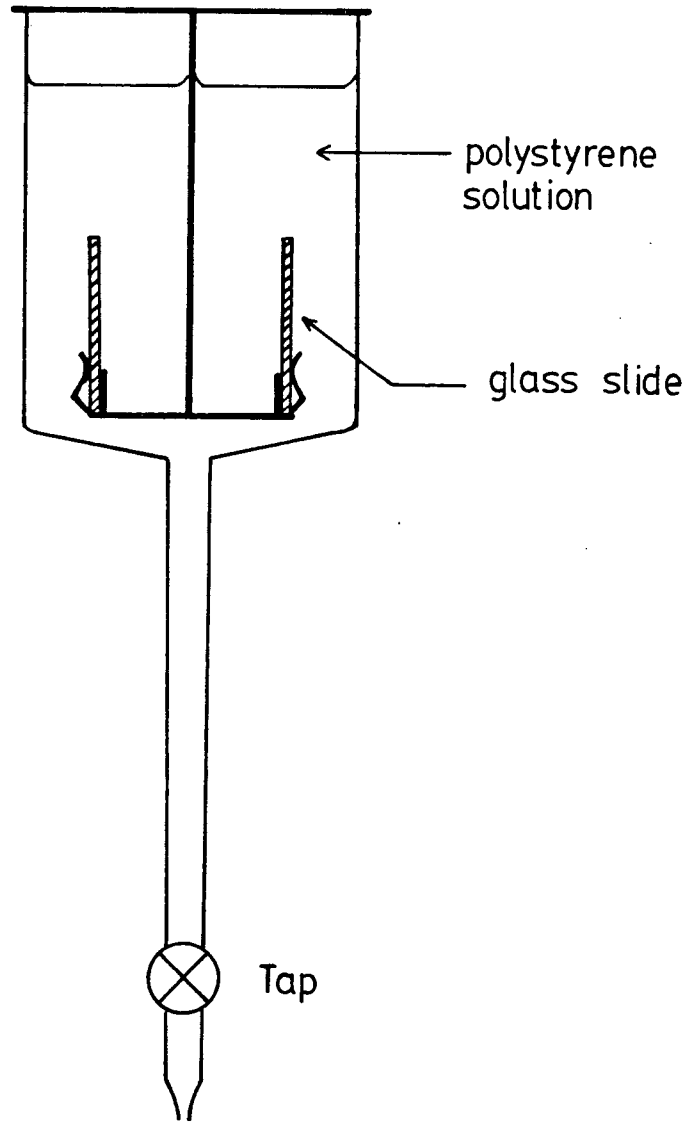

Figure 5-25 Experimental arrangement used in the fabrication of CH-multilayer targets.

Chapter 6

Experimental measurements of laser energy coupling to targets

6–1 Absorption measurements

In our experiment the absorption of laser light by the target was determined by measuring the incident and scattered light, the difference being the absorbed laser energy. The experimental arrangement has been shown in Figure 5 – 6 of Chapter 5. The incident laser energy was measured using a Gentec laser energy meter (model ED-200). The scattered light measurement consisted of measuring both the light scattered back through the focussing lens and the light scattered diffusely in a 4π geometry. The backscatter energy was monitered by a Gentec energy meter and the diffuse scattered light by a calibrated integrating sphere which enclosed the target. A description of the integrating sphere has been given in section 5 – 3 of Chapter 5.

Targets consisting of 50 μm thick aluminum foils, 25 μm thick gold foils and 130 μm thick polystyrene (CH) foils were irradiated with laser pulses of 2 ns (FWHM) at 0.532, 0.355 and 0.266 μm wavelength. The targets were sufficiently thick to prevent target disassembly while the absorption is still in progress (see Section 5 – 3 – F). The laser light was focused on target using $f/10$ optics, at an angle of incidence of 10° from target normal. At focus, 90 % of the laser energy was contained in a spot of 80 μm diameter. The laser beam was linearly polarized with its electric field inclined at 45° with respect to the plane of incidence.

In Figure 6 – 1 we have plotted the percentage of energy absorption as a function of the incident laser intensity. The error in the absorption measurement is estimated to be less than 4 %. In this figure data points with error bars represent averages of multiple shots at nearly identical irradiance. (All error bars given in this thesis correspond to standard deviation in a single set of measurements). Data points with no error bars represent single laser shot measurements. The data show very high level of absorption for all laser wavelengths, laser intensities and targets of different Z. For 0.266 and 0.355

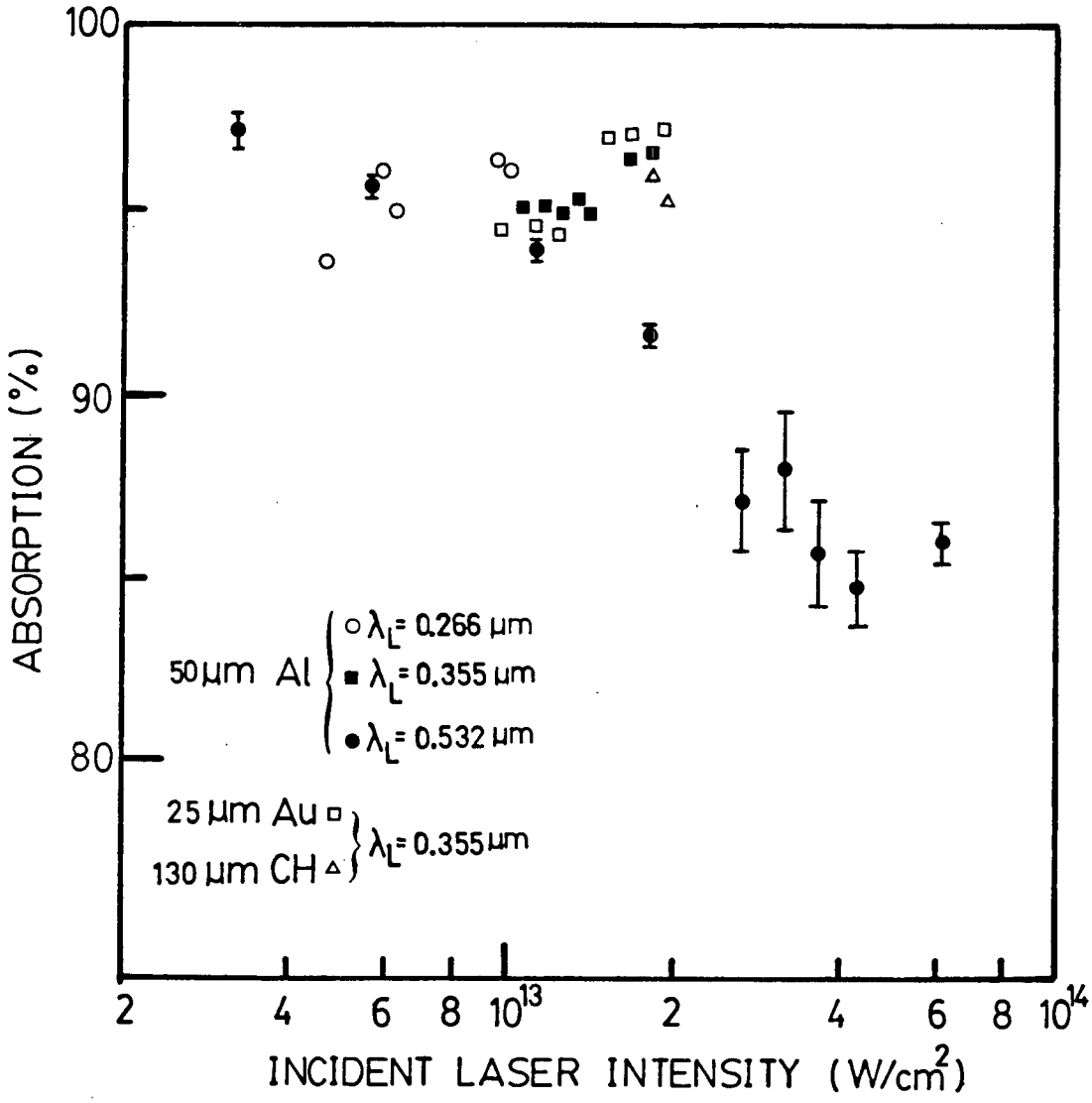

Figure 6-1 Absorption fraction as function of laser intensity for different laser wavelengths.

for all laser wavelengths, laser intensities and targets of different Z. For 0.266 and 0.355 μm laser radiation and aluminum targets we observed $\sim$ 95 % absorption for intensities between 10^{12} - 2×10^{13} W/cm^2 . The same absorption level was also measured at 0.355 μm when instead polystyrene (CH) foils or gold foils were used as target. At 0.532 μm and for aluminum targets, $\sim$ 95% absorption was also observed for incident laser intensities less than 10^{13} W/cm^2. However, for higher intensities the absorption started to decrease and at 5×10^{13} W/cm^2 it was around 85 %.

All of these observations are consistent with inverse bremsstrahlung being the dominant absorption mechanism. As discussed in Chapter 2 no other absorption mechanism can produce such high level of absorption. In Section $2-1$ of Chapter 2, using equation $(2-13)$, the absorption was estimated to be 100 % for our experimental conditions. In this calculation we assumed a plasma with a constant temperature and constant density gradient scale length. No scattering of the laser light was taken into account. These assumptions are not completely realistic and may explain the reason for the lower absorption fraction ($\sim$ 95%) observed in our experiment. We recall that inverse bremsstrahlung absorption in an exponential density profile (see equation $2-13$ of chapter 2) is stronger for short laser wavelengths, low plasma temperature (low laser intensity) and high Z plasmas. For laser intensities higher than 10^{13} W/cm^2 we have indeed observed stronger absorption for 0.266 and 0.355 μm than for 0.532 μm. At 0.532 μm, we have also observed a decrease in the absorption for increasing laser intensity (increasing plasma temperature). No dependence on the target Z value was observed at 0.355 μm because the absorption was nearly complete even for low Z plasmas.

In the next section we discuss measurements of the plasma electron temperature which provided further evidence that inverse bremsstrahlung is the dominant absorption mechanism in our experiment.

6–2 Plasma electron temperature

The absorbed laser energy is thermalized in the plasma. Therefore more information can be gained about the absorption mechanisms by measuring the plasma temperature and its dependence with the laser parameters. The plasma electron temperature can be obtained by measuring the X-ray line or continuum emission from the plasma[119]. In our experiment

suggested by Jahoda et al [91]. In this technique the X-ray continuum transmitted through different X-ray filters is measured and the result is compared to calculated curves for different plasma temperatures. Details of these calculations are described in Appendix A.

The dependence of the plasma electron temperature on laser intensity was measured in a series of experiments in which aluminum targets were irradiated with laser pulses of 2 ns at 0.532 μm at irradiances of 3×10^{12} - 1.1×10^{13} W/cm^2. The measurements were made using the multichannel X-ray detector described in Section 5 – 3 – G of Chapter 5. The detector was used in a 9 channels configuration where the X-ray filters for each channel consisted of a 10 μm beryllium support foil plus aluminum foils ranging in thickness from 5 μm to 21 μm in steps of 2 μm. Using this detector it was possible to monitor the plasma electron temperature for every laser shot on target. In the analysis of the results it was assumed that the observed signals were solely due to continuum emisssion with no significant X-ray line contribution. This assumption is not unreasonable because all the X-rays lines emitted by the aluminum plasma (Figure 5 – 15 of Chapter 5 shows the most energetic lines of the spectrum) have energies below the lowest cut-off energy (energy for e^{-1} transmission) of the filters used and are therefore strongly attenuated. Because of the high intensities of certain lines it may still be possible that some of the X-ray line radiation contributed significantly to the signals in the 5 μm and 7 μm aluminum filter channels. However, since the transmitted spectrum is determined from a large number of channels this would have little effect on the final result.

Figure 6 – 2 shows a typical distribution of the relative intensity of X-ray continuum transmitted through different filters in the nine-channel detector. Laser intensity on target for this shot was 1.3×10^{13} W/cm^2. The plasma electron temperature was determined by comparing the distribution with theoretical curves for different temperatures. As shown in this figure the best-fit theoretical curve yields an electron temperature of 550 eV. Uncertainties in the curve fitting limit the accuracy of the temperature measurement to $\pm$50 eV. The measured temperature represents a spatially and temporally integrated value. Since the X-ray continuum emission increases with the plasma temperature and density, this measurement is weighted towards the peak of the laser pulse and towards the higher plasma density region. In Figure 6 – 3 we have plotted the measured plasma electron

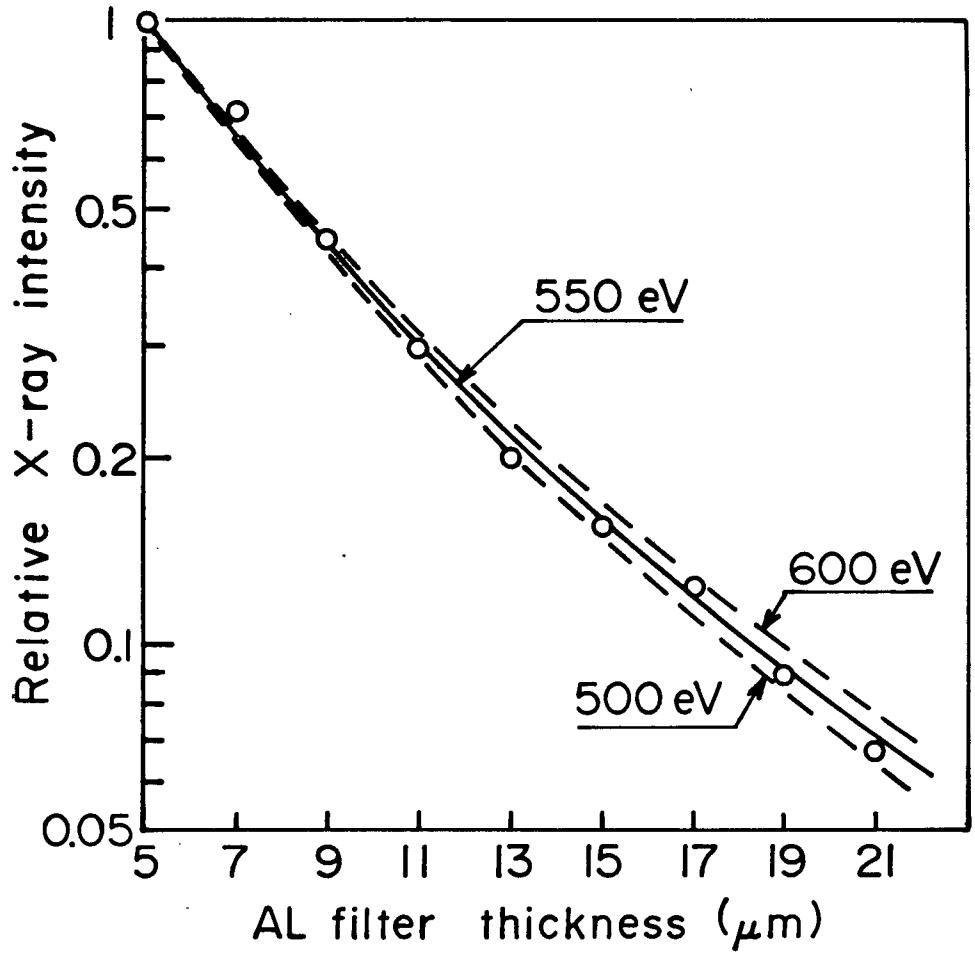

Figure 6–2 Relative intensity of X-ray continuum transmited through different filters.

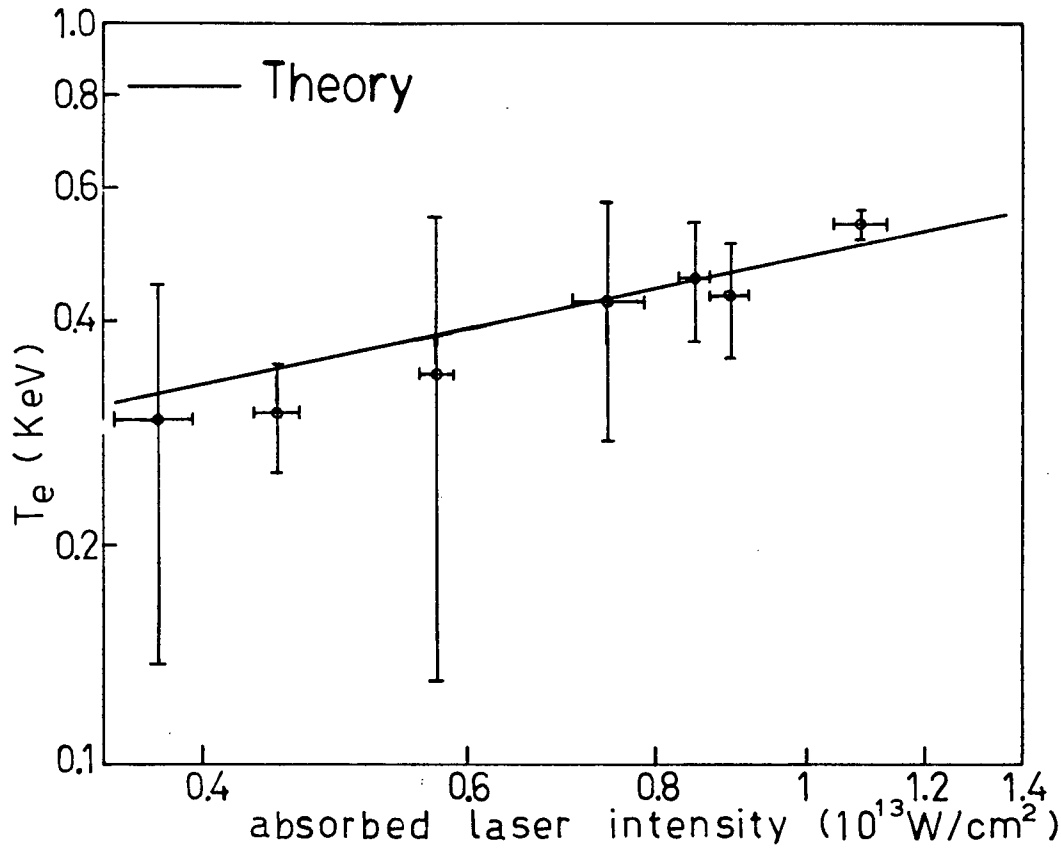

Figure 6–3 Scaling of electron temperature as laser intensity for 0.532 μm radiation.

plasma density region. In Figure 6 – 3 we have plotted the measured plasma electron plasma temperature as a function of the absorbed laser intensity. Each data point in this figure represents an average of many laser shots. The corresponding standard deviations are indicated. In this figure we have also plotted (solid line) the dependence of the electron temperature with absorbed laser intensity as predicted by equation (4 – 36) of Chapter 4 which was derived for a strong inverse bremsstrahlung absorption regime. This line is in good agreement with our data and further verifies that inverse bremsstrahlung is indeed the dominant absorption mechanism.

As discussed in Chapter 2, inverse bremsstrahlung absorption produces a thermal distribution of electrons while other absorption mechanisms, such as resonance absorption and various laser-driven plasma instabilities, produce a small population of very energetic electrons. These energetic electrons produce "harder" X-rays than thermal electrons and therefore will show their signatures in the X-ray spectrum. To asses the existence of other absorption mechanisms in our experiment the measurement of the X-ray continuum was extended to include the more energetic part of the X-ray spectrum. For this measurement the X-ray emission was monitored using a set of three X-ray PIN diodes[89]. (The multi-channel X-ray detector could not be used for this measurement as its sensitivity rapidly drops for X-rays with energies higher than 5 keV). Results of the measurement are shown in Figure 6 – 4 which includes X-ray emissions obtained at 5° and 30° from target normal. This corresponds to aluminum targets irradiated with 0.532 μm laser light for an average absorbed irradiance of 3×10^{13} W/cm^2. The X-ray spectrum in Figure 6 – 4 was measured from many laser shots at nearly identical irradiance and the data points represent the average values with the corresponding standard deviations.

The X-ray spectrum obtained indicates the presence of two electron temperature distributions. The dominant component represents the thermal plasma with a temperature of 550 ± 50 eV. However X-ray emissions near target normal (data points for −5° with electron-sweeping magnets in front of the diode) show a "hot" component of about 1.5 keV. The presence of energetic electrons is also evident from the data points for −5° without the sweeping magnet. Equation (2 – 25) of Chapter 2 gives the predicted temperature of the electrons produced by resonance absorption. For our experimental conditions (T_e=500 eV, $I_A = 3 \times 10^{13}$ W/cm^2 and $\lambda_L = 0.532\,\mu m$) it gives $T_{hot} = 1.6$ keV which is in good

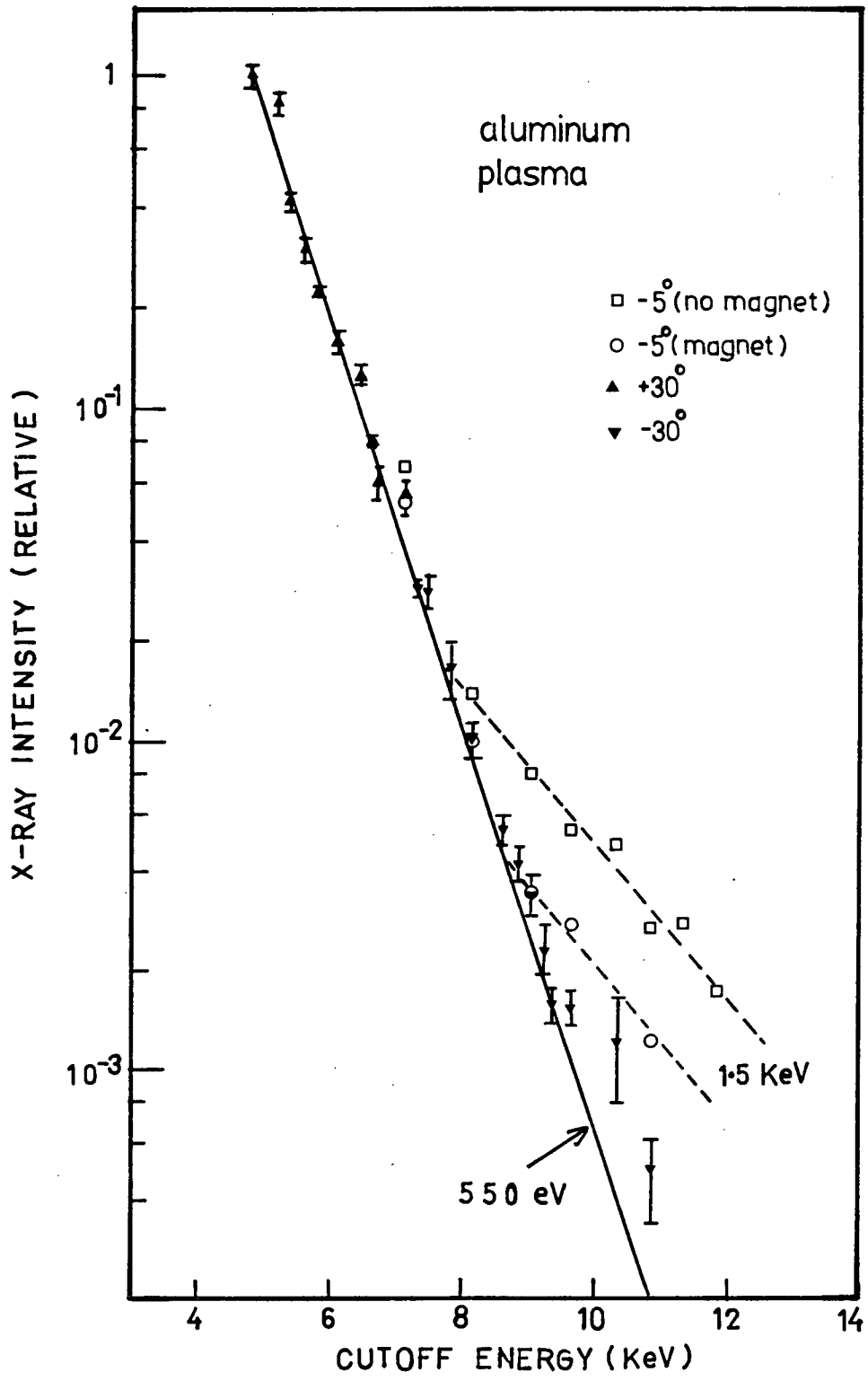

Figure 6–4 X-ray continuum spectrum for 0.532 μm radiation, $I_A = 3 \times 10^{13}$ W/ cm^2.

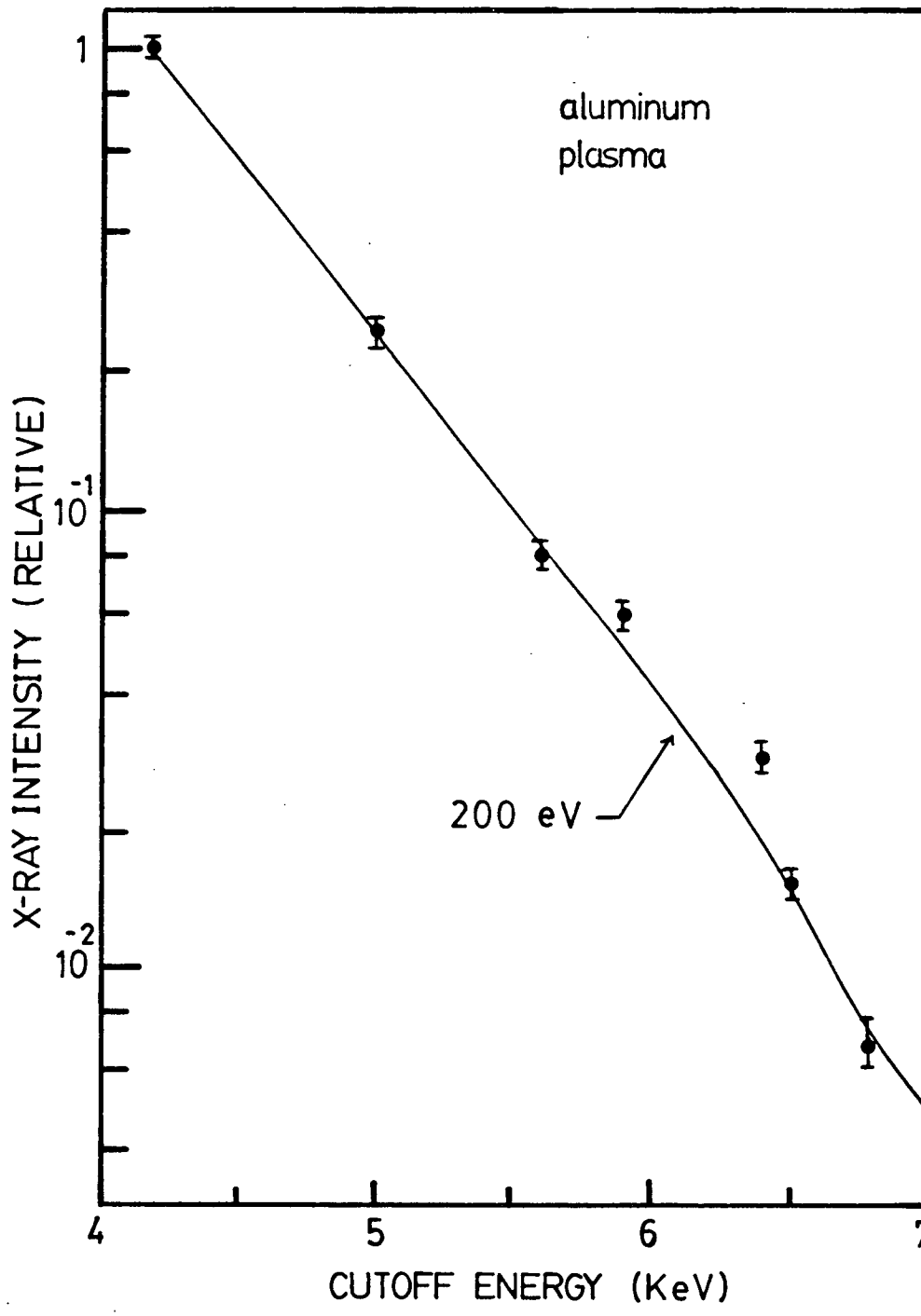

Figure 6–5 X-ray continuum spectrum for 0.266 μm radiation, $I_A = 3 \times 10^{13}$ W/cm^2.

X-ray components and from the fact that the X-ray intensity is proportional to the square of the electron density, the number of the hot electrons is roughly estimated to be $\leq 1\%$ of that of the thermal electrons.

The electron plasma temperature was also measured at 0.266 μm for an absorbed irradiance of 3×10^{13} W/cm^2. The results of the measurement is shown in Figure $6-5$. These indicate a plasma temperature of 200 eV. It is qualitatively in agreement with equation $4-36$ of Chapter 4, which predicts a lower plasma temperature for shorter laser wavelength. The X-ray spectrum did not show the presence of hot electrons. This was expected because we were operating below the threshold of laser-driven plasma instabilities. Also, with very strong inverse bremsstrahlung absorption, virtually no laser energy reached the critical density surface where resonance absorption could occur.

6-3 Laser induced plasma instabilities

As we have seen in Chapter 2 parametric instabilities are not expected to be important for our experimental conditions. To see if any instabilities were excited, the light backscattered through the focussing lens was monitored using a laser energy meter and a fast photodiode with different interference filters. The experimental arrangement has been shown in Figure $5-2$ of Chapter 5.

A low level ($< 4\%$) of Brillouin backscatter was observed in the 0.532 μm experiments. The Brillouin reflectivity as a function of incident laser intensity is shown in Figure $6-6$. The instability was observed to grow from noise at an intensity of about 8×10^{12} W/cm^2. Using the formula given in Table $2-1$ of Chapter 2 the threshold intensity for this instability is calculated to be 8×10^{13} W/cm^2. This apparent discrepancy may be due to the fact that we observe a spatially- and temporally-averaged intensity whereas the instantaneous intensity at the peak of the laser pulse and in the central part of the focal spot is much higher.

$(3/2)\,w_L$ light was also observed in the 0.532 μm experiment. The source of $(3/2)\,w_L$ light is not well understood[97]. It is generally assumed to arise from the presence of electron plasma waves near $n_{cr}/4$. The two possible sources of these waves are the two-plasmon decay instability and the stimulated Raman scattering instability. The $(3/2)\,w_L$ light is a second order process involving either the coalescence of three electron plasma waves or

a second order process involving either the coalescence of three electron plasma waves or the coalescence of an electron plasma wave and an electromagnetic wave. In our experiment the $(3/2)w_L$ light is probably due to the two-plasmon decay instability, as it has a lower threshold intensity. Figure 6 – 7 shows the backscattered intensity of $(3/2)w_L$ light as a function of the laser intensity. The maximum intensity measured corresponds to a reflectivity of less than 5×10^{-9}. Our measured threshold intensity for the excitation of the instability is 1.1×10^{13} W/cm^2 which is again smaller than the theoretically predicted value of 9.9×10^{13} W/cm^2. This may be due to the same reason discussed above.

In the 0.355 and 0.266 μm experiments, no $(3/2)w_L$ emission was observed. Only marginal signals from Brillouin backscatter were detected. This was expected because the intensity thresholds for all the laser driven plasma instabilities are higher for shorter laser wavelengths.

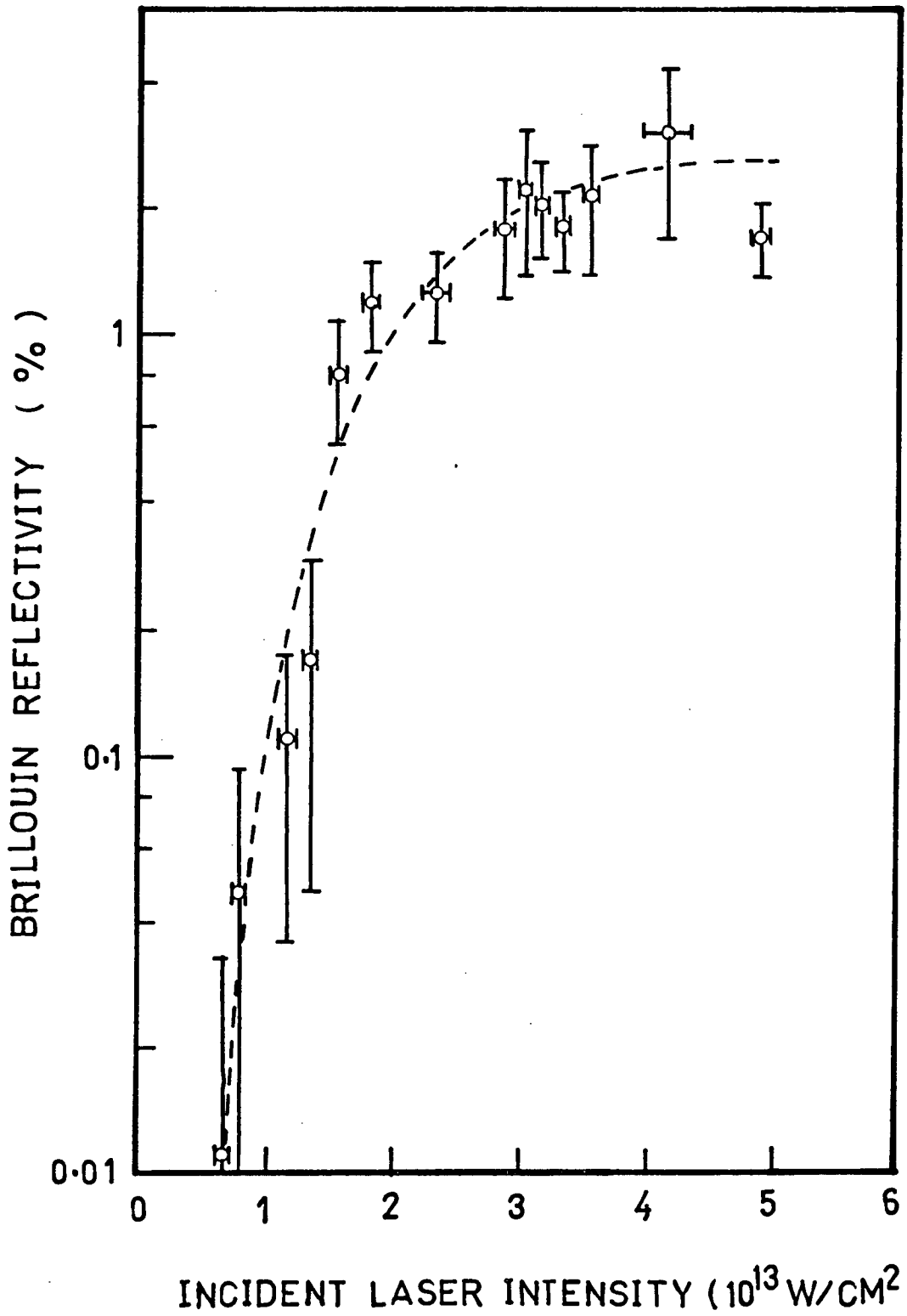

Figure 6–6 Brillouin reflectivity as a function of incident laser intensity for 0.532 μm radiation.

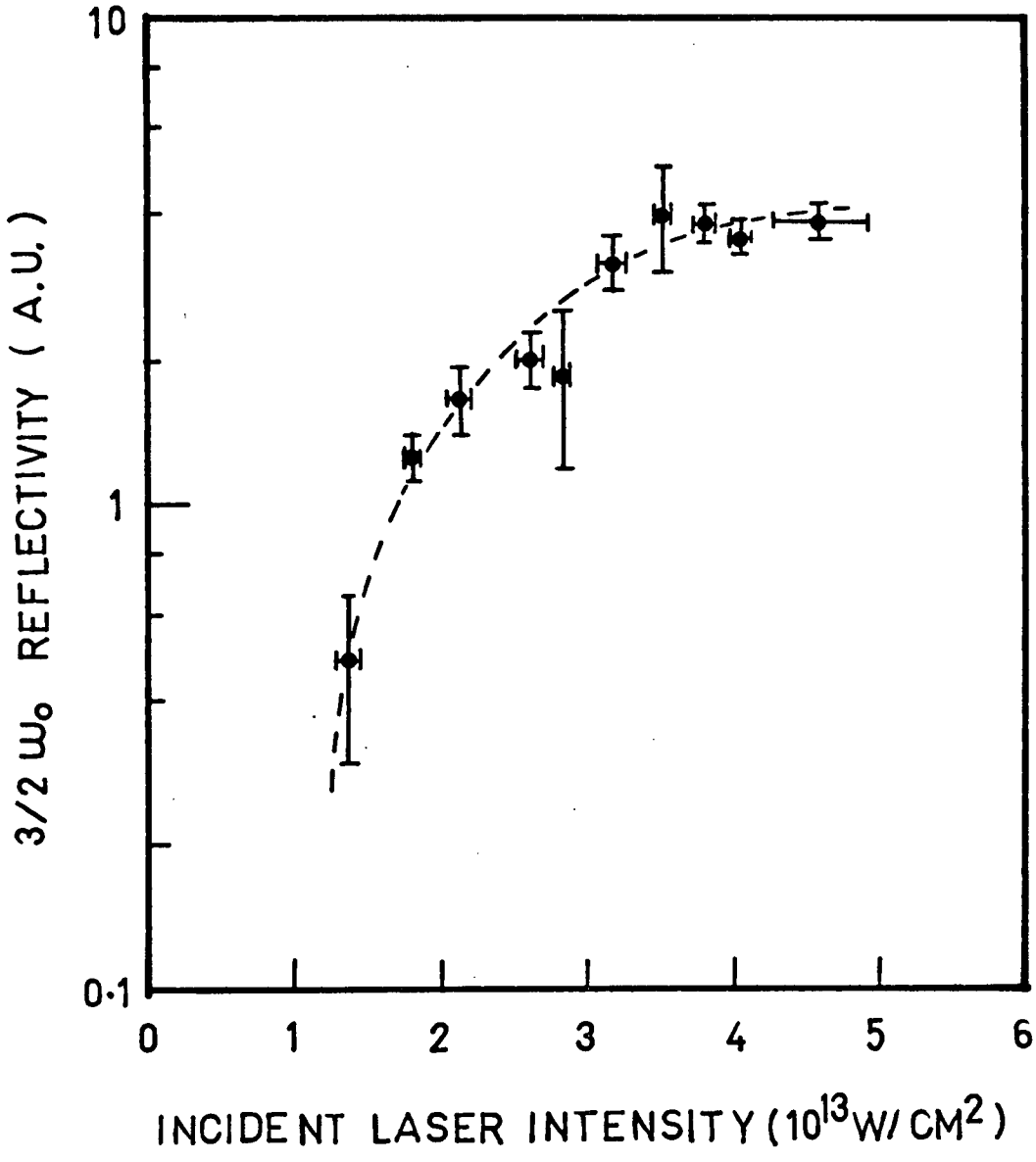

Figure 6–7 $\frac{3}{2}w_L$ backscatter reflectivity as a function of incident laser intensity for 0.532 μm radiation.

Chapter 7

Investigation of electron energy transport using multilayer targets

As discussed in Chapter 3, the extreme temperature and density gradients inherent in laser-produced plasmas render the exact theoretical description of heat transport difficult. There are many unresolved problems in correlating theory and experimental data. Thermal transport measurements are therefore important to gain a better understanding of this important aspect of the laser-target interaction. An observable quantity closely related to thermal transport is the mass ablation rate, $\dot{m}$, which is the rate at which material is ablated from unit target area. An average value for $\dot{m}$ can be defined by

$$\dot{m} = \frac{M}{A\,\tau_{Abl}} \quad , \qquad (7-1)$$

where M represents the total mass ablated during the interaction, A the ablation surface area and τ_{Abl} the average ablation time. In Chapter 8 we will present measurements of $\dot{m}$ based on a direct evaluation of the parameters of equation $(7-1)$.

The total mass ablated M can also be expressed as

$$M = \rho A d \quad , \qquad (7-2)$$

where ρ represents the initial target density and d the "ablation depth", that is, the thickness of material ablated during the interaction. In principle, the ablation depth can be obtained by measuring X-ray line radiation from the substrate layer of multilayer targets. This diagnostic technique was first reported by Seka *et al.*[98] and have been used in many experimental investigations of thermal transport[11,12,77,78,99–105]. Targets are made of a tracer substrate material coated with varying thicknesses of target material. During laser irradiation a thermal front penetrates into the solid, ablating the target material and eventually, for sufficiently thin target layer, reaches the substrate causing characteristics X-ray

lines to be emitted. By measuring the X-ray lines emission from the substrate as a function of the target layer thickness it is possible to study the propagation of the thermal front into the target material. The thickness of target layer at which the X-ray line emission disappear is usually taken as the laser ablation depth.

In this chapter we report on an investigation of thermal transport using such multilayer targets. In section $7-1$ the experimental conditions are described. This is followed in section $7-2$ by a summary of the results of this study, which revealed anomalies that indicate a limitation of the multilayer techniques for energy transport measurements. A simple hydrodynamic model which can account for such anomalies is presented in Section $7-3$.

7–1 Experimental conditions

In our experiment glass slides of thickness 130 microns were used as the substrate material. To study the effect of the target density on thermal energy transport, five different coating materials were selected. These included polystyrene (CH), magnesium (Mg), tin (Sn), silver (Ag) and gold (Au). Details about the procedures for target fabrication are given in Chapter 5, section $5-4$.

Silicon lines emitted from the glass (SiO_2) substrate were spectrally resolved using a flat KAP crystal spectrometer. The X-ray spectrometer is described in Chapter 5, Section $5-3-$ D. The instrument was oriented at 15° off target normal with a crystal-to-target distance of 12 cm (see Figure $7-1$). A typical silicon spectrum from the glass substrate is shown in Figure $7-2$. The spectrum was recorded using Kodak SC-5 X-ray film. It includes hydrogen-like and helium-like lines which are present only for plasma temperatures of several hundred electron volts[106]. The X-ray detector used was a plastic scintillator (NE102) coupled through fiber optics to a photomultiplier tube (RCA 8575). The scintillator surface exposed to the X-ray radiation was covered with a 25 μm thick beryllium foil to block off visible light. The combined response time of the plastic scintillator, photomultiplier tube and oscilloscope was of the order of 10 ns. Since the X-ray line emission is known to last for the duration of the laser pulse[104] (2 ns) only, the measured intensities were effectively time integrated. In order to discriminate properly between the X-ray emission from the glass substrate and the X-ray emission from the upper layer, an adjustable slit was positioned

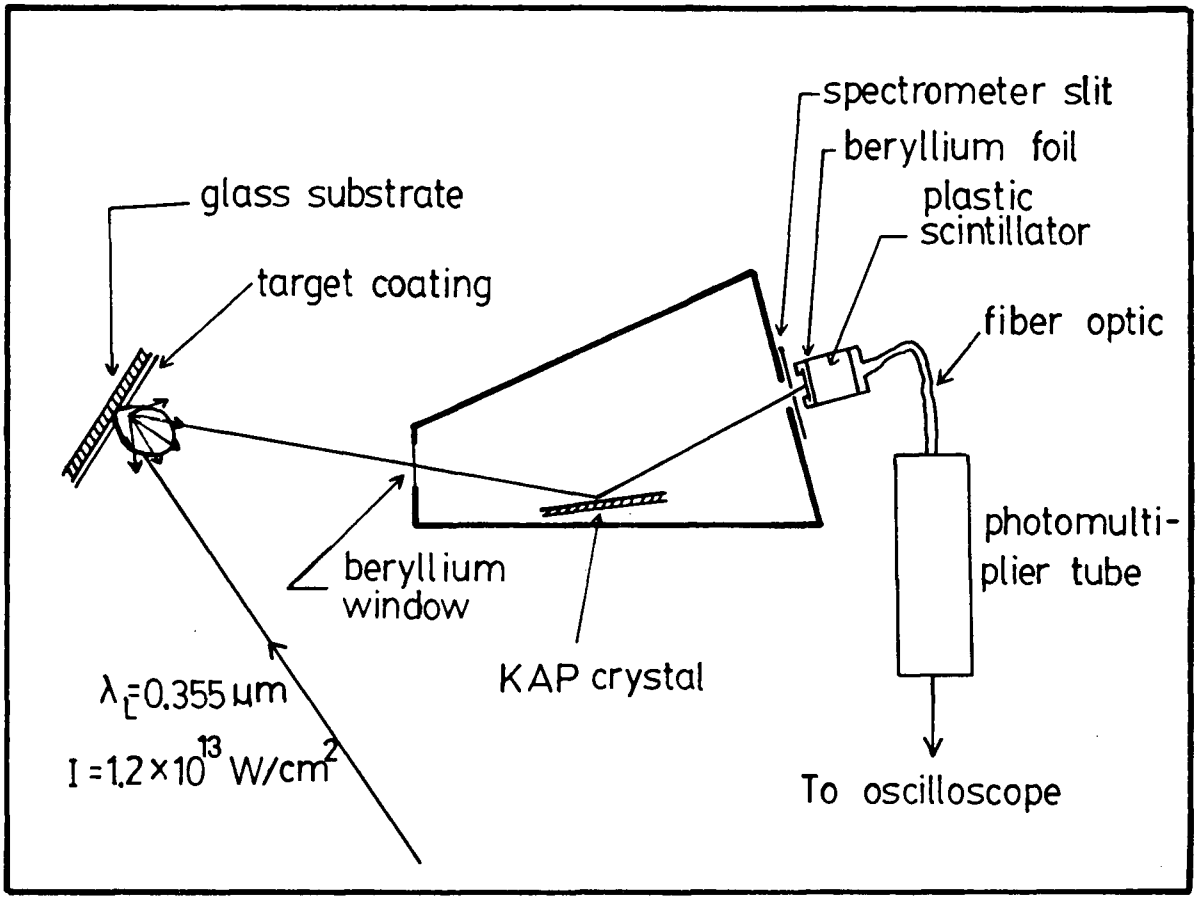

Figure 7–1 Experimental arrangement for energy transport measurement.

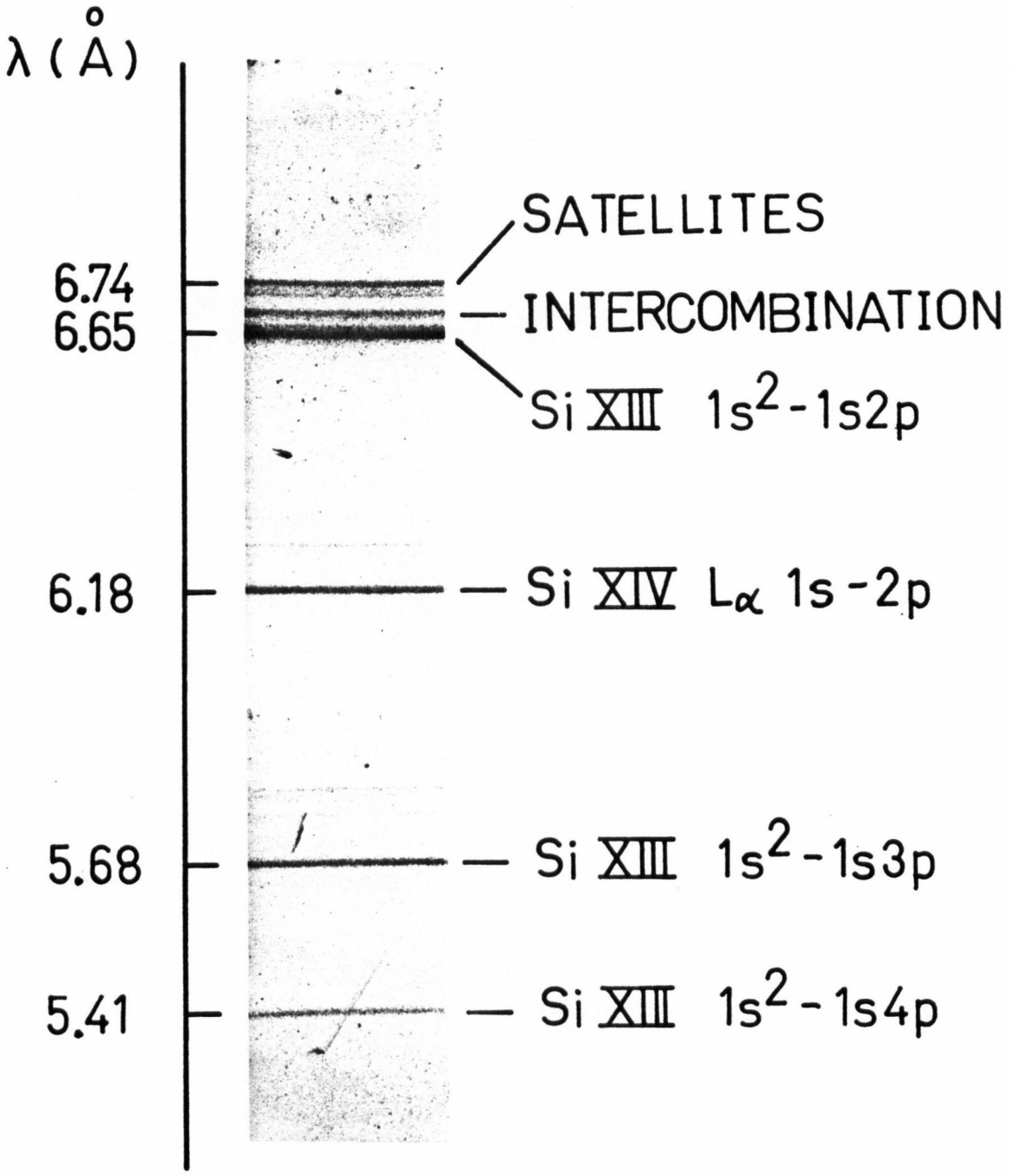

Figure 7–2 Silicon line spectrum.

at the rear of the spectrometer to accept only a selected part of the spectrum. For the CH-, Sn- and Ag-glass multilayer targets, the slit was adjusted to accept only that part of the spectrum between 6.65 and 6.74 Å. As shown on Figure 7 – 2 this includes the Si XIII $1s^2(^1S_0)-1s2p(^1P_1)$ resonance line, the intercombination line $1s^2(^1S_0)-1s2p(^3P_1)$ and some weaker satellite lines (the satellite lines are due to transitions in ions with outer shielding electrons). For the Mg- and Au-glass targets, emissions from the Mg or the Au layer were so strong that in order properly to isolate the substrate emission, the slit was narrowed to accept only the Si XIII $1s^2(^1S_0) - 1s2p(^1P_1)$ line.

This series of experiments was done using 0.35 μm laser light. The irradiance conditions were kept constant with 90% of the energy contained within a focal spot of 80 μm diameter, giving an intensity of 1.2×10^{13} W/cm^2 at the target surface.

7.2 Experimental results

Figure 7 – 3, 7 – 4 and 7 – 5 show the observed intensity of the silicon line group between 6.65 and 6.74 Å for CH-, Sn- and Ag-glass multilayer targets as a function of the target layer thickness. Figure 7 – 6 and 7 – 7 show the intensity of the silicon resonance line Si XIII $1s^2(^1S_0) - 1s2p(^1P_1)$ as a function of the target layer thickness for the Mg- and Au-glass multilayer targets. The intensity is given in arbitrary units, normalized to the intensity observed for zero coating thickness. Each data point on these figures represents a group average from many laser shots, with error bars indicating the corresponding standard deviations. The given target layer thicknesses are estimated to be precise within 10%. In Figures 7 – 3 to 7 – 7 we observe an expected drop in the intensity of the X-ray line emission from the glass substrate, for increasing target layer thickness. The intensity then reaches a plateau which corresponds to the basic noise level of each type of target, which was established by irradiating pure targets of the coating material. We here define as "laser penetration depth" the thickness of target layer for which X-ray line emissions from the substrate layer disappear. Figure 7 – 8 shows this laser penetration depth as a function of target material density. The best fitted line yields a density dependence of $\rho^{-1.5}$ for the penetration depth. As discussed in the introduction of this chapter the usual interpretation of the multilayer target diagnostic[101] is that the X-ray emission from the substrate layer is detectable only if the overcoat target layer has been completely ablated during the laser

pulse. However we will show that our results are inconsistent with this interpretation, and that the measured penetration depth differs significantly from the conventionally defined "ablation depth" which is a true measure of the thickness of material vaporized from a pure target. The ablation depth itself was measured using another experimental diagnostic. Far away from the target all the thermal energy of the plasma has been transformed into kinetic energy of expansion. By measuring both the energy and asymptotic velocity of the expanding plasma we can obtain the total mass ablated, which is given by

$$M = \frac{2E}{< V^2 >} \quad , \tag{7-3}$$

where E is the total plasma energy and $< V^2 >$ its mean square velocity. This was done for aluminum targets (details of the measurement are discussed in chapter 8; the experimental results are presented in Figure $8-3$ for different irradiance conditions). Now the ablation depth is simply obtained from equation $(7-2)$ as

$$d = \frac{M}{\rho A} \quad , \tag{7-4}$$

where ρ is the target density and A the ablation surface area. Using this formula, the value for the total mass ablated at 1.2×10^{13} W/cm^2 from Figure $8-3$, the density of aluminum and assuming the ablation crater to be of cylindrical geometry with a diameter the size of the focal spot, yields a value of 2.4 ± 0.8 μm for the ablation depth in aluminum. This ablation depth for Al is indicated on Figure $7-8$. In this figure, the dashed line indicates the actual penetration depth obtained. The ablation depth measured for Al clearly lies well below the penetration depth curve (X-ray intensity measurements on Al-glass targets could not be made because it was not possible to isolate silicon diagnostic lines from the intense nearby aluminum lines). Also, the density dependence given by equation $(7-4)$ is only ρ^{-1}, in marked disagreement with the observed density dependence of $\rho^{-1.5}$.

Two dimensional effects such as spatial inhomogeneities in the laser beam or thermal self-focusing[16] and filamentation[16] in the plasma could conceivably cause the laser energy to be channelled into a small area, drastically increasing the local irradiance. Thus the mass ablation rate would be greatly increased in a local region smaller than the laser focal spot, leading to large ablation depth. However no evidence for this was seen in the image

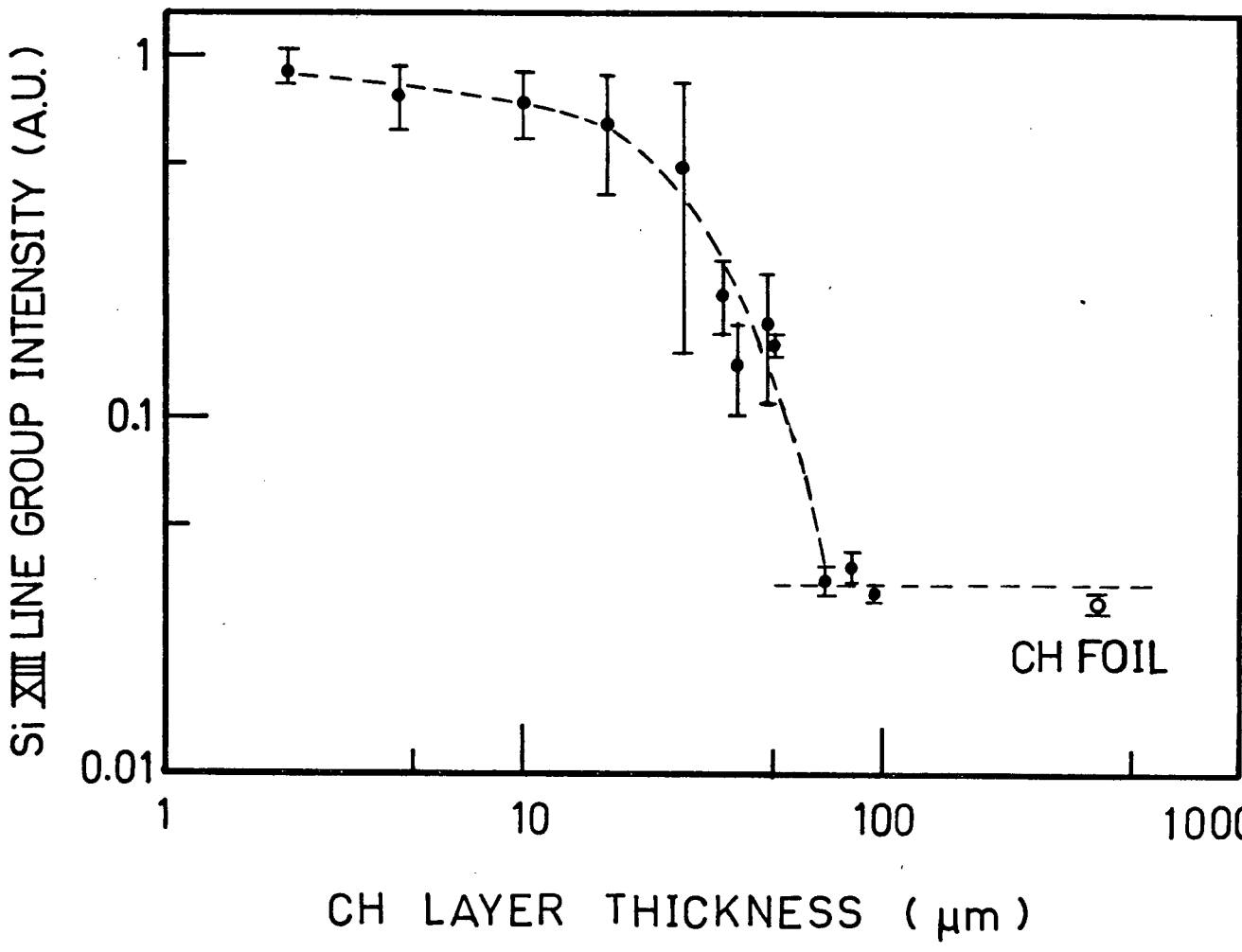

Figure 7–3 Intensity of the silicon line group between 6.65 and 6.74 Å as function of CH layer thickness.

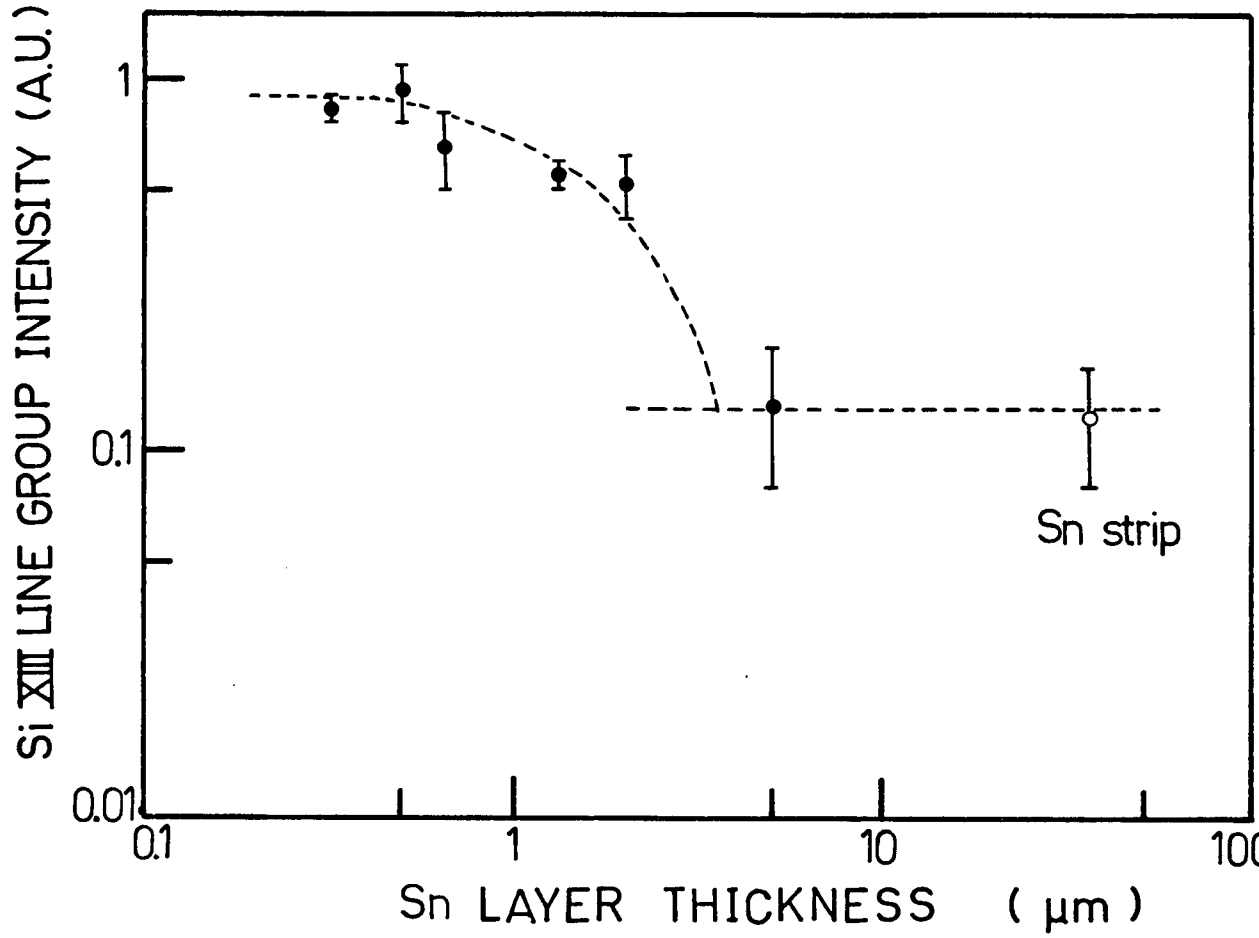

Figure 7–4 Intensity of the silicon line group between 6.65 and 6.74 Å as function of the Sn layer thickness.

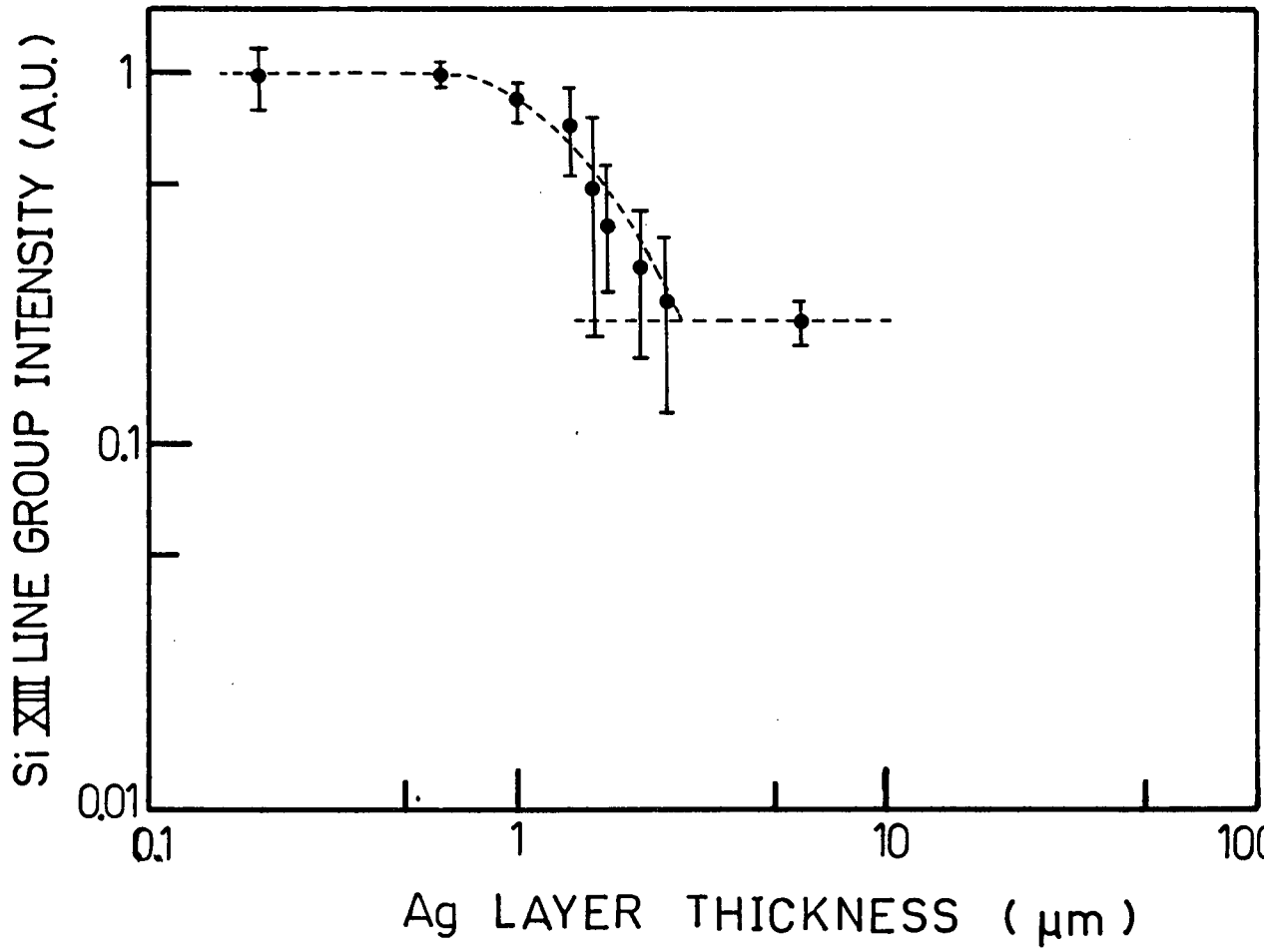

Figure 7–5 Intensity of the silicon line group between 6.65 and 6.74 Å as fuction of Ag layer thickness.

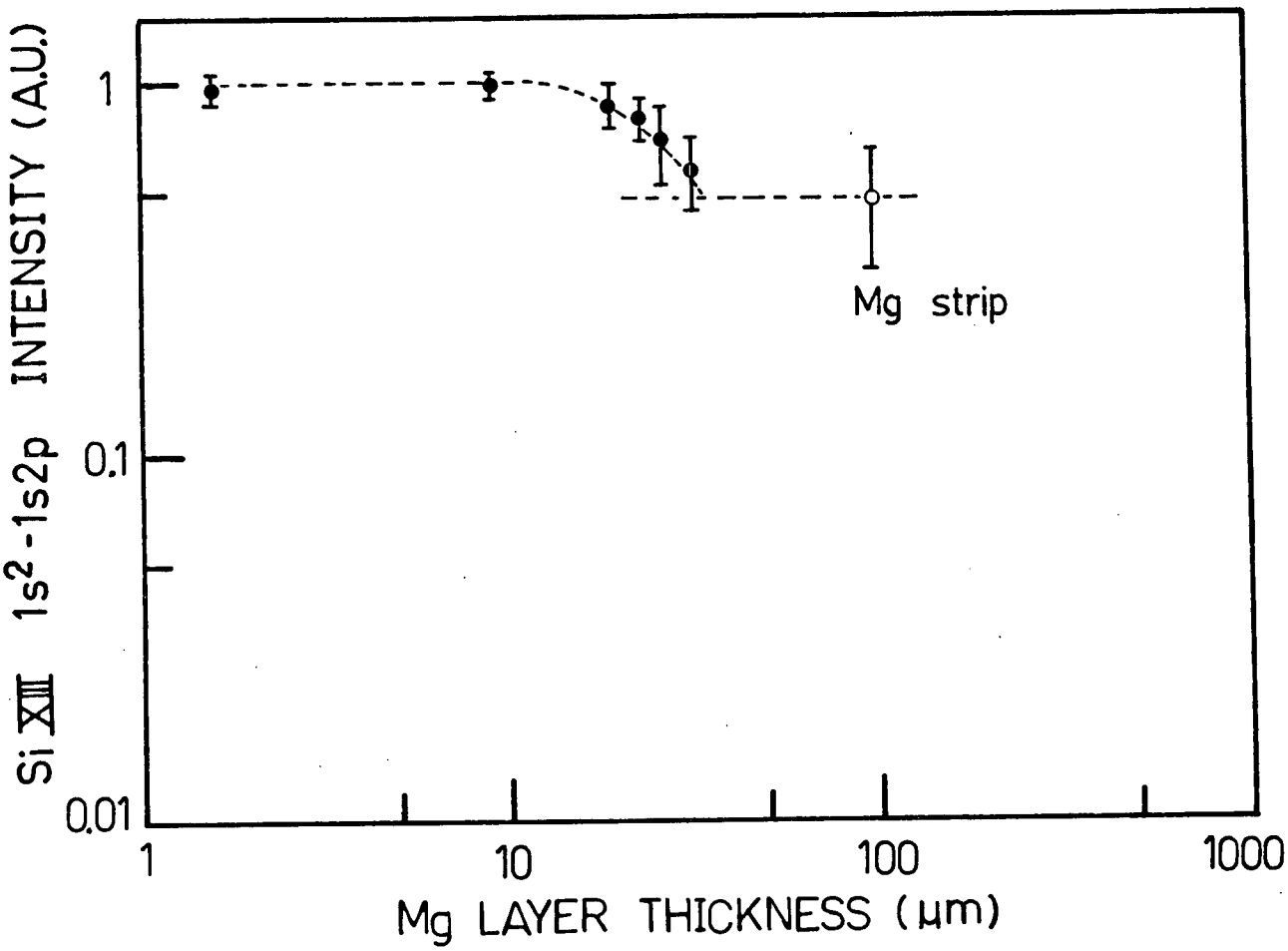

Figure 7–6 Intensity of the Si XIII $1s^2(^1S_0) - 1s2p(^1P_1)$ line as a function of Mg layer thickness.

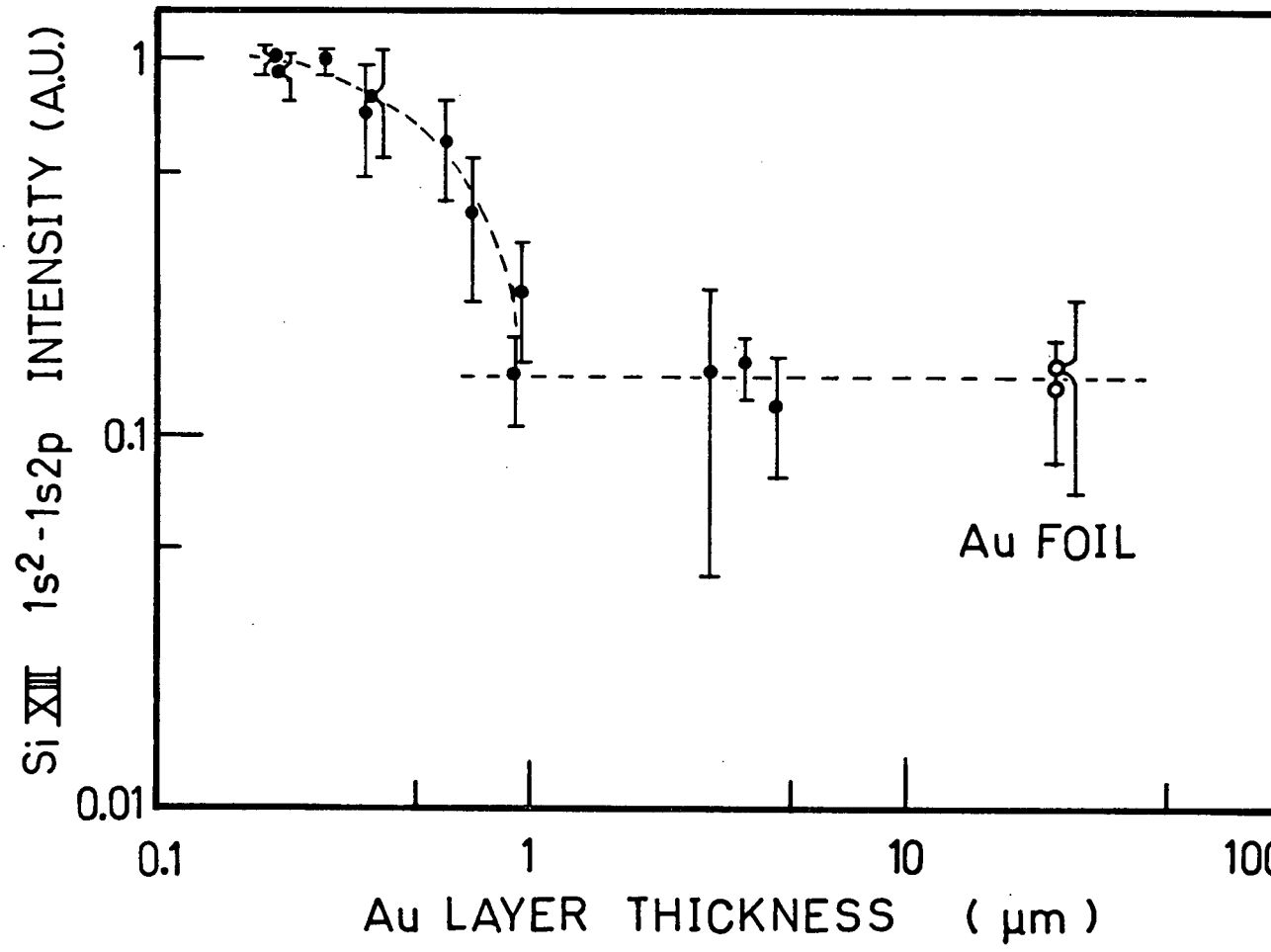

Figure 7–7 Intensity of the Si XIII $1s^2(^1S_0) - 1s2p(^1P_1)$ line as a function of Au layer thickness.

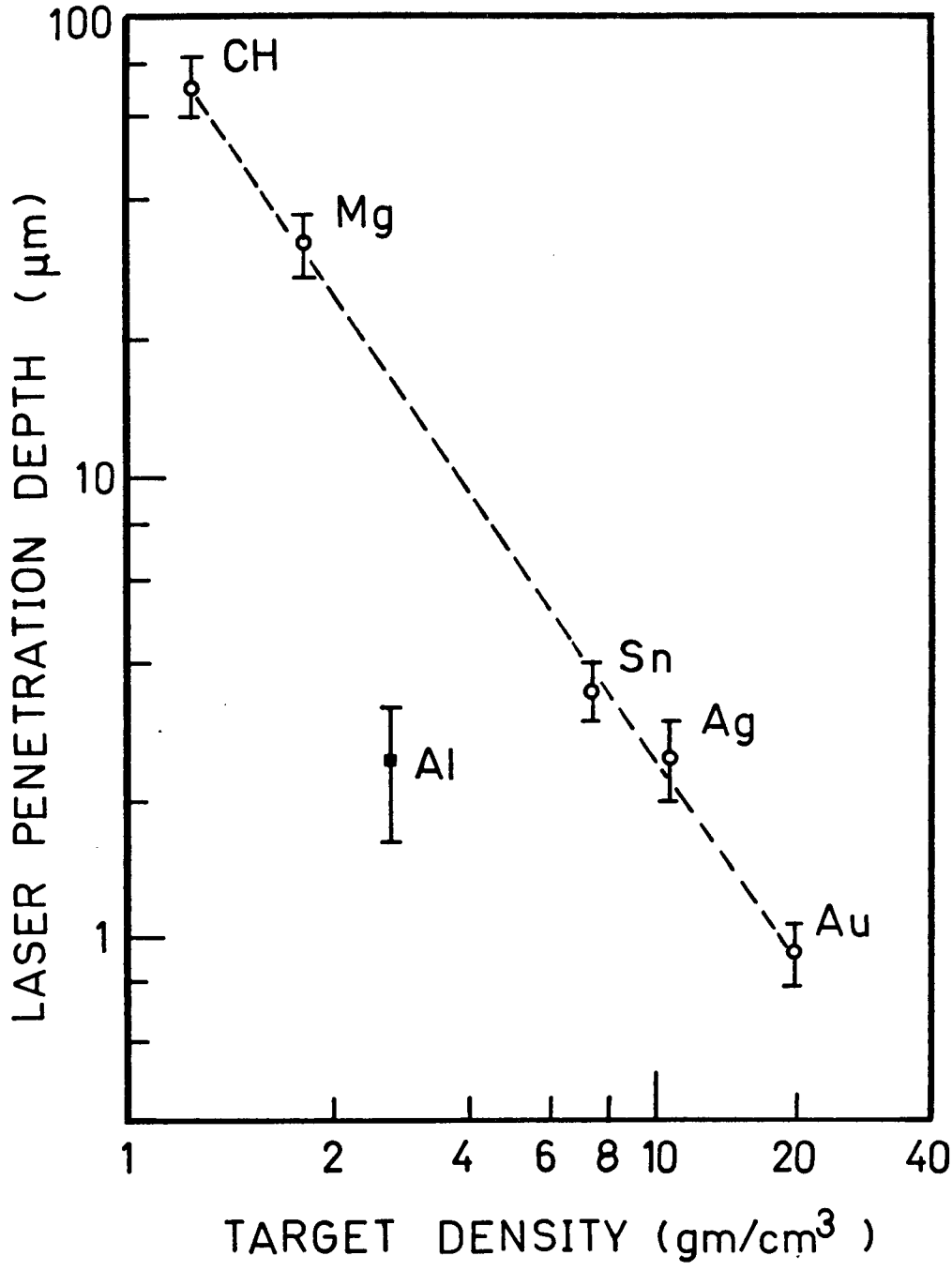

Figure 7–8 Laser penetration depth as a function of target density : (○) multilayer target measurements , (■) ions measurements.

of the focal spot, or in X-ray emission pictures of the plasma (see Chapter 5, Sections 5 – 2 and 5 – 3 – F). Moreover even if such variations in the local irradiance could explain the large penetration depth, it could not explain the measured density dependence. To explain these anomalies we propose in the next section a simple hydrodynamic model in which the ablation process is modified by an edge effect due to the finite, small focal spot.

7–3 A hydrodynamic model for laser penetration depth

In the irradiation of a solid by a high intensity laser, as indicated in Figures 4 – 1 and 4 – 2 of Chapter 4, a shock wave propagates into the solid with a characteristic velocity U_S. It is followed by an ablation front (boundary layer between the shock compressed solid and the resultant plasma) moving with a characteristic velocity V_a. This is shown schematically in Figure 7 – 9. To allow formulation of a tractable physical model, we have assumed, as depicted in Figure 7 – 9, that: (i) the lateral distribution of the laser intensity in the focal spot can be approximated as trapezoidal, (ii) the resulting ablation front A also has a trapezoidal profile and (iii) transient effects due to the density discontinuity at the target-substrate interface are not present and the ablation front A, contact surface B and the shock front C all propagate with steady velocities. The density discontinuity can cause the shock wave to be reflected at the interface if the substrate material is more dense than the target material, or produce a returning rarefaction wave if the substrate material is less dense than the target material[107]. Such detailed interactions, however will be neglected in this simple model. Given that the measured density dependence (Figure 7 – 8) appears to be insensitive to the density ratios of the target to substrate it is reasonable to assume that the effects of density discontinuity at the target-substrate interface may be neglected.

As illustrated in Figure 7 – 9, the hydrodynamic motions of the ablation surface and the contact surface produce a thin, stretched layer of target material along the edge of the irradiated spot. From the simplified geometry of trapezoidal profiles, shown in Figure 7 – 9 it follows that the thickness of the stretched target layer is simply

$$\Delta = \frac{L}{U_S \tau}\left(\frac{1}{(V_a/U_S)} - 1\right)D_o \qquad (7-5)$$

where L is the projection of the rising edge of the laser focal spot spatial profile (Figure 7–9), τ is a time of the order of the laser pulse length, U_S and V_a are the shock and ablation

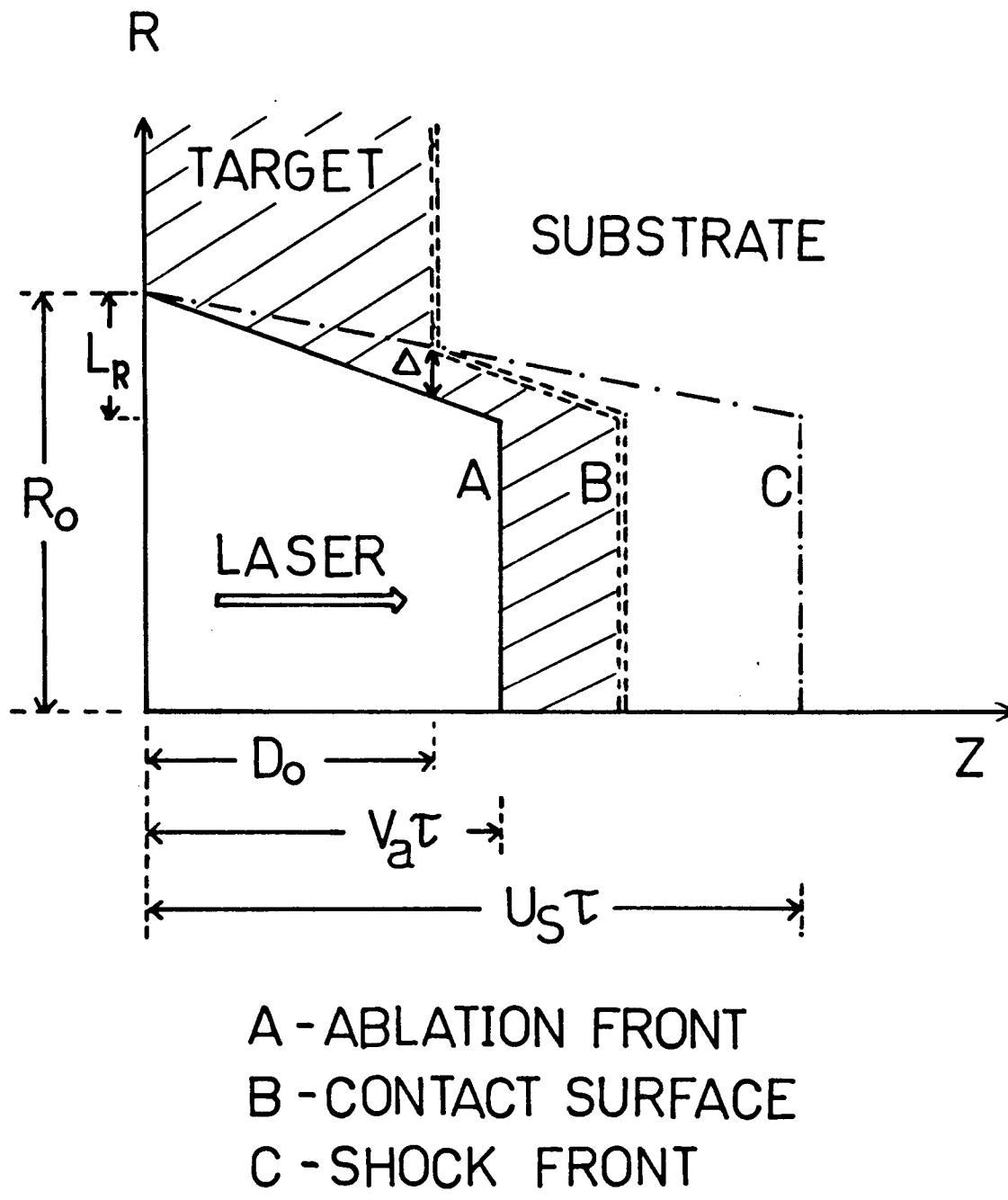

Figure 7–9 Schematic showing the hydrodynamic shearing of the target layer.

front speeds and D_o is the original thickness of the target layer. Shock compression of this layer is further assumed to be negligible. If such an edge distortion effect occurs before the end of the laser pulse, ablation of the stretched target layer by lateral thermal conduction can produce X-ray emissions from the substrate material. Thus, for an axial penetration depth D_o, there is a corresponding lateral ablation depth of Δ , indicated in Figure $7-9$. To see that this model predicts the observed behavior, Equation $7-5$ can be rewritten as

$$D_o = \frac{\tau}{L}\left(\frac{1}{(V_a/U_S)} - 1\right)^{-1} U_S \Delta \qquad (7-6)$$

in which L , τ and (V_a/U_S) are independent of the target density[110] ρ. From conservation equations[107] U_S varies as $\rho^{-0.5}$, while the ablation depth Δ varies as ρ^{-1}. Therefore, the penetration depth will scales as $\rho^{-1.5}$, in agreement with the measured scaling.

Further evidence for the model is obtained by considering the penetration depth in aluminum as inferred from the measured density dependence. Interpolation of the data in Figure $7-8$ yields a penetration depth in aluminum of 16 ± 3 μm. For an irradiance of 1.2×10^{13} W/cm^2, a shock pressure of 4.3 Mbar was measured (see Figure $8-4$). For such a shock pressure, calculations[108-109] showed that $U_S \approx 2 \times 10^6$ cm/s and $(V_a/U_S) \approx 0.6$. τ is taken as 2 ns which is the full-width-half-maximum duration of the laser pulse. Measurements of the laser intensity distribution in the focal spot indicated that $L \sim 15$ μm. Substituting these values into equation $(7-5)$, one obtains $\Delta = 4.0 \pm 0.8 \mu$m. This is reasonably consistent with the ablation depth of 2.4 ± 0.8 μm obtained from the ion energy and velocity measurements.

A direct test of the model would be the observation of the ring of emission in a temporally resolved, spatial image of the Si line. The insufficient X-ray flux, however precluded this observation in our work.

Chapter 8

Experimental scaling laws for the mass ablation rate and the ablation pressure

In this chapter we present experimental measurements of the ablation pressure and mass ablation rate using planar aluminum targets irradiated with 0.265 and 0.532 μm laser pulses of 2 ns (FWHM) and at irradiances of $10^{12} - 5 \times 10^{13}$ W/cm^2. To complete the analysis on wavelength dependence, we have also included the measured intensity scalings of the mass ablation rate and ablation pressure for 0.355 μm radiation from the work of P. Celliers[59]. In Section 8 – 1 we discuss the measurement principle and the experimental set-up. The experimental results are then presented in Section 8 – 2. Further discussions and comparison with theoretical predictions are given in Section 8 – 3.

8 – 1 Measurement principle and experimental set-up

By measuring the energy and velocity of the expanding plasma, time averaged values for the mass ablation rate and the ablation pressure can be obtained . This is possible because far away from the target all the plasma internal energy has been converted to kinetic energy of expansion and we can write:

$$E = \frac{1}{2} M < V^2 > \qquad (8-1)$$

where E is the total plasma energy, M the total mass ablated and $< V^2 >$ the mean square velocity of the expanding plasma. The total mass ablated M and the momentum $p_\perp$ carried off perpendicular to the target can be evaluated from:

$$M = 2\pi \int_0^{\frac{\pi}{2}} \frac{2E(\theta)}{< V^2(\theta) >} \sin\theta d\theta \quad , \qquad (8-2)$$

and

$$p_\perp = 2\pi \int_0^{\frac{\pi}{2}} \frac{2E(\theta)}{< V(\theta) >} cos(\theta) sin(\theta) d\theta \quad . \qquad (8-3)$$

Here θ represents the angular position from the target normal and cylindrical symmetry about the target normal is assumed. Average values for the mass ablation rate $\dot{m}$ and the ablation pressure P_{Abl} are then evaluated using the expressions:

$$\dot{m} = \frac{M}{A_{Abl}\,\tau_{Abl}} \quad , \tag{8-4}$$

and

$$P_{Abl} = \frac{p_{\perp}}{A_{Abl}\,\tau_{Abl}} \quad . \tag{8-5}$$

where A_{Abl} is the ablation area and τ_{Abl} the ablation time. In this analysis the ablation area was assumed to be the same size as the laser focal spot of 80 μm diameter for 90% energy content (Chapter 5, Section 5 – 2). The ablation time is of the same order as the laser pulse length but slightly longer because both $\dot{m}$ and P_{Abl} scale as the laser intensity to a power less than unity. To estimate τ_{Abl} we have used the width at the 1/e intensity points of our laser pulse taken to the 7/9 power (theoretical intensity scaling for ablation pressure). This was 2.7 ns. To evaluate expressions 8–4 and 8–5 the energy E and average velocity $< V >$ of the expanding plasma are required. The plasma energy was measured using differential calorimeters. A description of the differential calorimeters has been given in Chapter 5, Section 5 – 3 – C. The plasma calorimeters measure both the ion energy and the energy of the X-ray radiation emitted by the plasma. For an aluminum plasma the total amount of energy radiated in the X-ray range is expected to be of the order of 15% for our experimental conditions[15,111]. These X-rays are emitted isotropically in a 4π angle. In our analysis the X-ray contribution to the detector signal was assumed negligible. The possible effect of this assumption on our derived scaling laws is discussed below. The velocity of the expanding plasma was measured using Faraday cups which have been described in Chapter 5, Section 5 – 3 – B. A typical output signal is shown in Figure 5 – 7 – B. It shows a strongly peaked ion current signal indicative of a single narrow velocity distribution[112]. In our analysis the velocity given by the peak of the current trace was taken to approximate the average velocity of the expanding plasma.

The experimental set-up for the ion measurements is shown Figure 8 – 1. A total of seven differential calorimeters and seven Faraday cup collectors were used, arranged in a horizontal plane at angles between 5° and 80° from the target normal. The Faraday cups

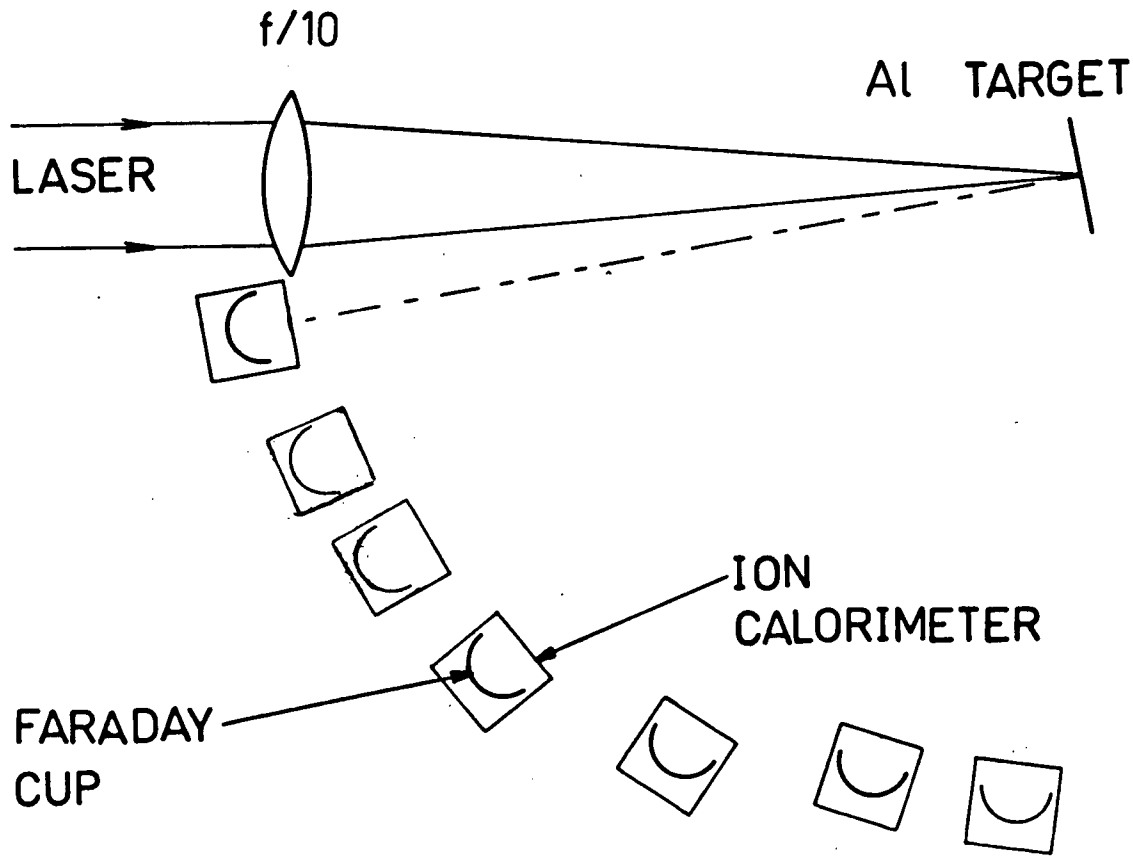

Figure 8–1 Experimental arrangement to measure energy and velocity of the expanding plasma.

were mounted directly above the calorimeters and therefore at the same angular position. The detector-pairs were placed at distance varying from 20 to 35 cm from the target. As indicated in Figure 8 – 1, 50 μm thick aluminum foils were used as targets and the pressure in the target chamber during these measurements was of the order of 10^{-5} Torr. Such vacuum is required to eliminate any significant charge exchange processes[114] which would modify the charge state of the ion flow arriving at the detector.

8–2–A Angular distributions of the plasma energy and velocity

Typical angular distributions of the plasma energy and velocity measured by the detectors are shown in Figure 8 – 2. The plasma energy is given in units of joules per steradian and the velocity in units of 10^7 cm/s. The angles in degrees are measured from the target normal. This particular energy and velocity distribution was observed for an incident irradiance of 6×10^{13} W/cm^2 and 0.532 μm laser light. Continuous functions representing the angular energy and velocity distributions were obtained by fitting cubic spline functions through the individual experimental data points. These functions were then used in expressions 8 – 4 and 8 – 5 to evaluate the mass ablation rate and the ablation pressure for each laser shot on target.

8–2–B Experimental scaling laws for the mass ablation rate and the ablation pressure

Figures 8 – 3 and 8 – 4 show the observed mass ablation rate in units of g/cm^2-s and the ablation pressure in units of Mbar (10^6 bars) as a function of the absorbed laser flux for different wavelengths. Each individual point represents one laser shot. Best-fitted lines to the data (solid lines on the figures) yielded the empirical scaling laws:

$$P_{Abl} = 4.4(I_A/10^{13})^{0.92} \quad \text{Mbar} \quad \text{for} \quad \lambda_L = 0.266\,\mu m \quad , \qquad (8-6-a)$$

$$P_{Abl} = 3.7(I_A/10^{13})^{0.84} \quad \text{Mbar} \quad \text{for} \quad \lambda_L = 0.355\,\mu m \quad , \qquad (8-6-b)$$

$$P_{Abl} = 3.0(I_A/10^{13})^{0.78} \quad \text{Mbar} \quad \text{for} \quad \lambda_L = 0.532\,\mu m \quad , \qquad (8-6-c)$$

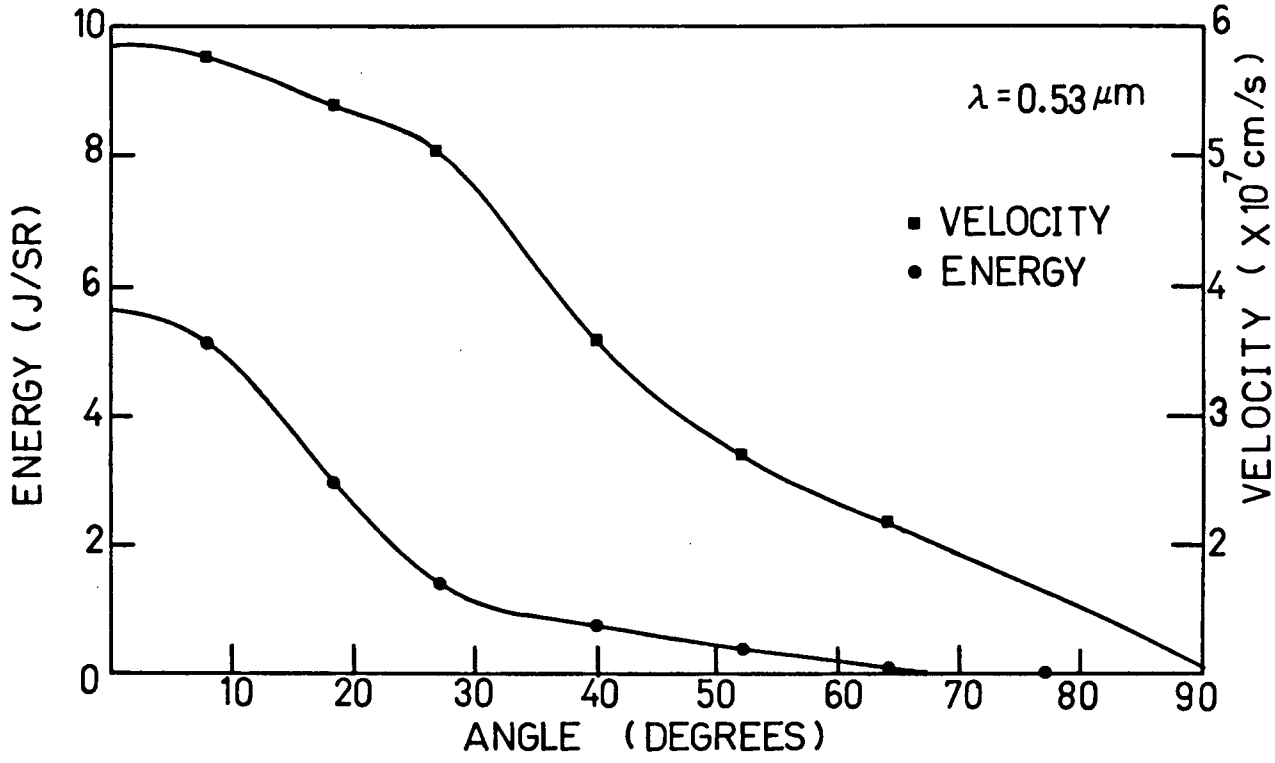

Figure 8–2 Energy and velocity distribution of the expanding plasma. $I_A = 6 \times 10^{13}$ W/cm^2.

and

$$\dot{m} = 3.3 \times 10^5 (I_A/10^{13})^{0.72} \quad \text{g/cm}^2\text{-s} \quad \text{for} \quad \lambda_L = 0.266\,\mu m \quad , \qquad (8-7-a)$$

$$\dot{m} = 2.3 \times 10^5 (I_A/10^{13})^{0.55} \quad \text{g/cm}^2\text{-s} \quad \text{for} \quad \lambda_L = 0.355\,\mu m \quad , \qquad (8-7-b)$$

$$\dot{m} = 1.3 \times 10^5 (I_A/10^{13})^{0.63} \quad \text{g/cm}^2\text{-s} \quad \text{for} \quad \lambda_L = 0.532\,\mu m \quad . \qquad (8-7-c)$$

The results show the ablation pressure and the mass ablation rate to increase for shorter wavelength radiation. This is expected since $P_A = 2n_0(\frac{Amp}{Z})C_0^2$ and $\dot{m} = n_0(\frac{Amp}{Z})C_0$ (eq. $4-18$ and $4-19$ of Chapter 4). For shorter laser wavelength the laser light penetrates to higher density n_0 (see eq. $4-34$ and $4-26$) with corresponding increases in P_A and $\dot{m}$. In general, wavelength scaling laws can then be derived from formula $(8-6)$ and $(8-7)$. However, at different laser wavelengths, both $\dot{m}$ and P_{Abl} exhibit slightly different dependences on the absorbed flux. This phenomenon was also observed in other scaling studies[14,104]. Consequently, the wavelength dependences of $\dot{m}$ and P_{Abl} may also be different at different irradiances, i.e. the intensity and wavelength scalings are not completely independent, in contradictions to steady-state ablation theories (see Chapter 4). To illustrate the wavelength dependences, experimental values of $\dot{m}$ and P_{Abl} are plotted against λ_L at absorbed fluxes of 2.6×10^{12}, 6.6×10^{12} and 10^{13} W/cm^2 (Figures $8-5$ and $8-6$) In these figures the data points represent average values for nearly identical laser intensities with the corresponding standard deviations. The dashed line represent the best-fitted line through the data points. For these irradiances, the wavelength scaling of $\dot{m}$ varied from $\lambda_L^{-1.15}$ to $\lambda_L^{-1.37}$ whereas that of P_{Abl} varied from $\lambda_L^{-0.34}$ to $\lambda_L^{-0.57}$.

8–3 Discussion of the results

Absorption measurements and the measured intensity scaling of the plasma electron temperature have indicated that inverse bremsstralung absorption is the dominant absorption mechanism in our experiments (Chapter 6). As described in Chapter 4, in this

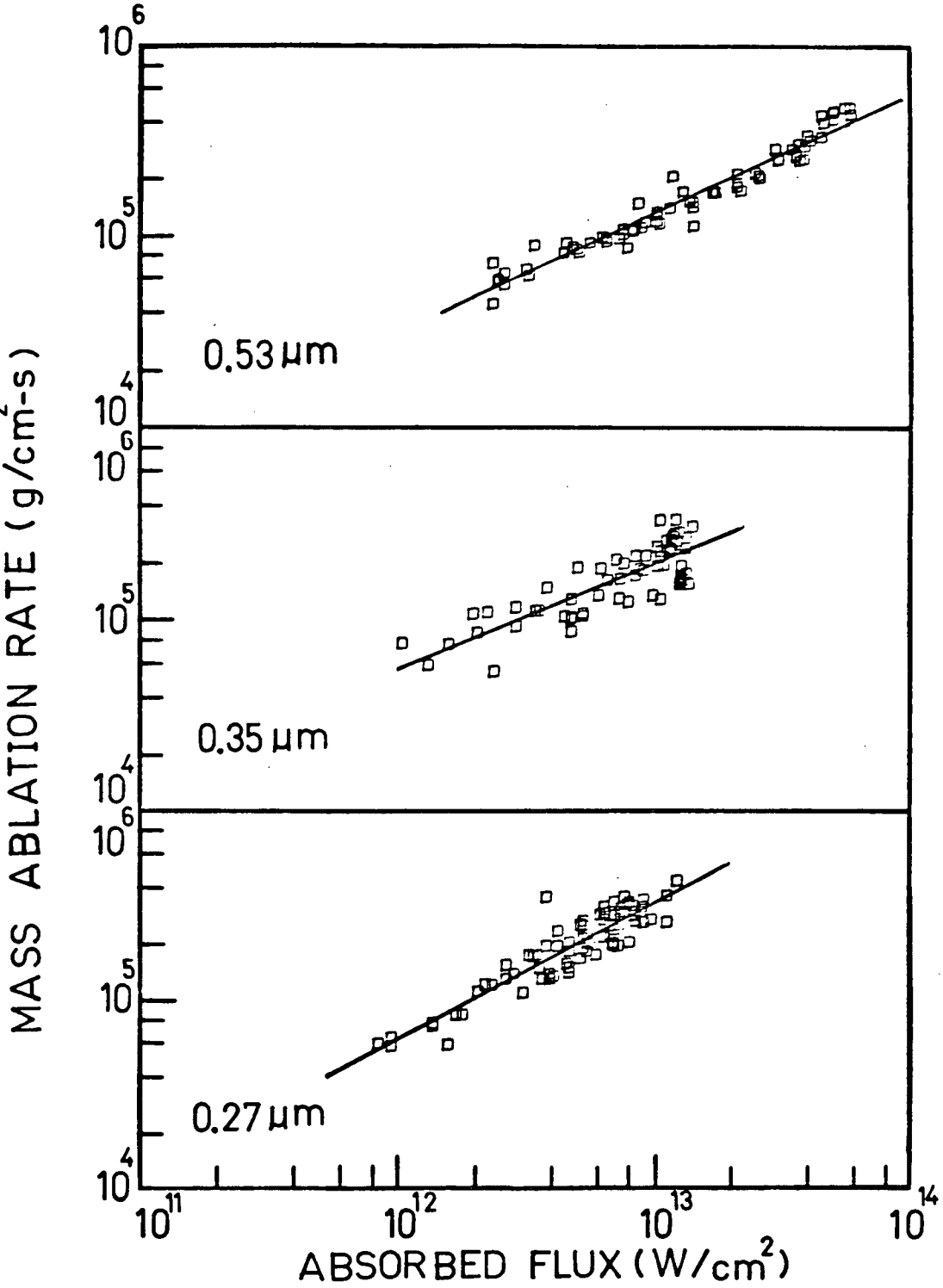

Figure 8–3 Mass ablation rate as a function of absorbed flux for 0.532, 0.355 and 0.266 μm laser light.

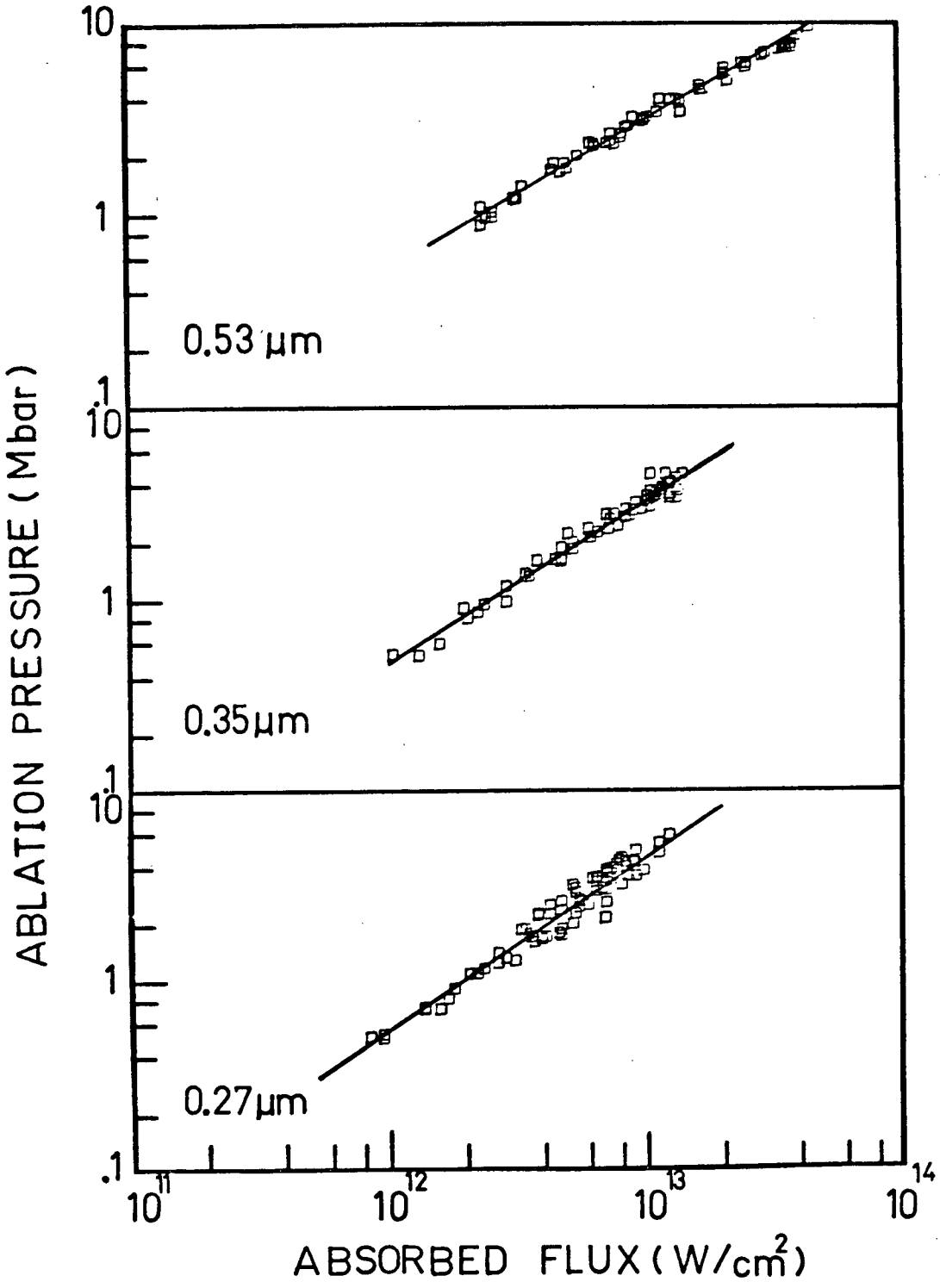

Figure 8–4 Ablation pressure as a function of absorbed flux for 0.532, 0.355 and 0.266 μm laser light.

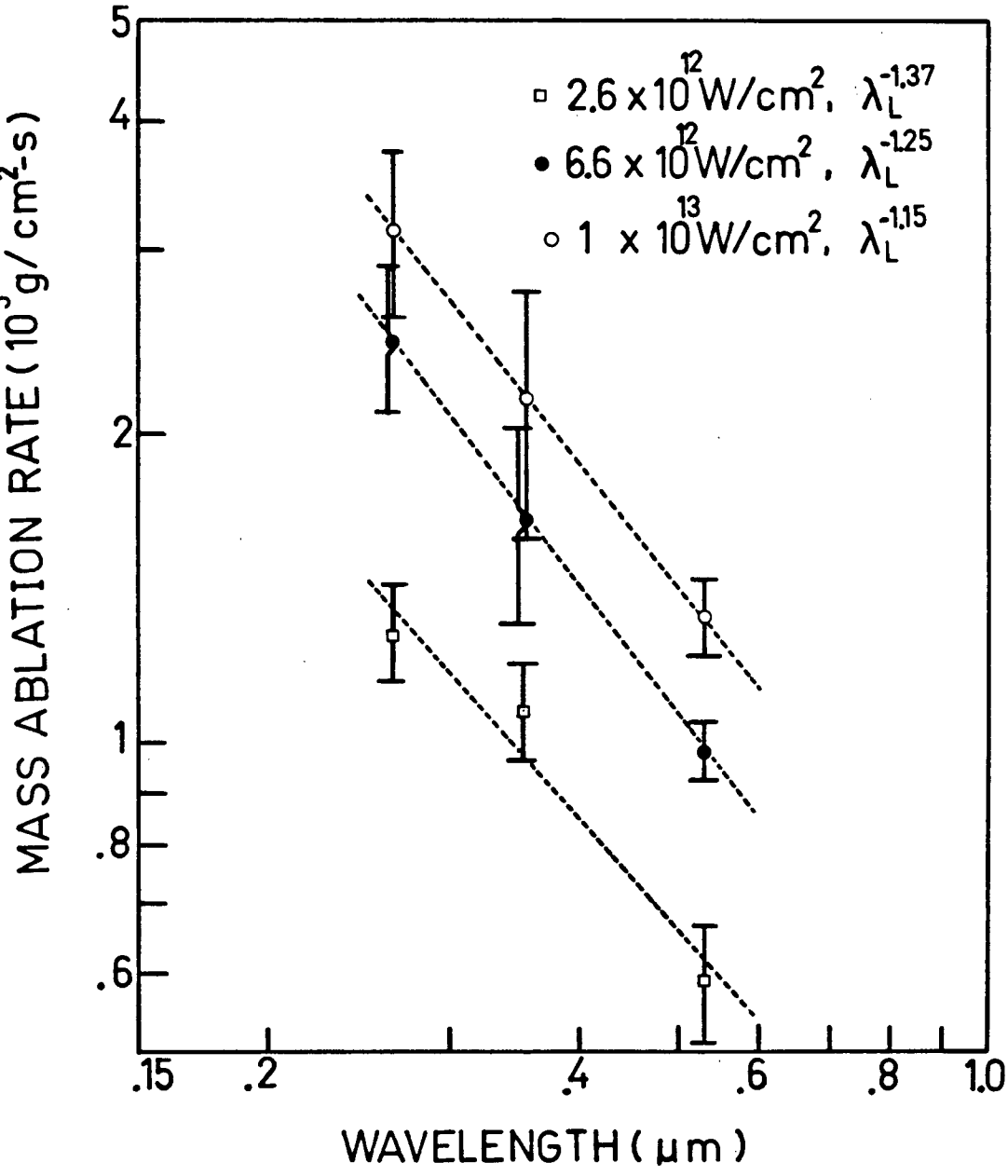

Figure 8–5 Wavelength dependence of mass ablation rate at absorbed irradiances of 2.6×10^{12}, 6.6×10^{12} and 10^{13} W/cm^2.

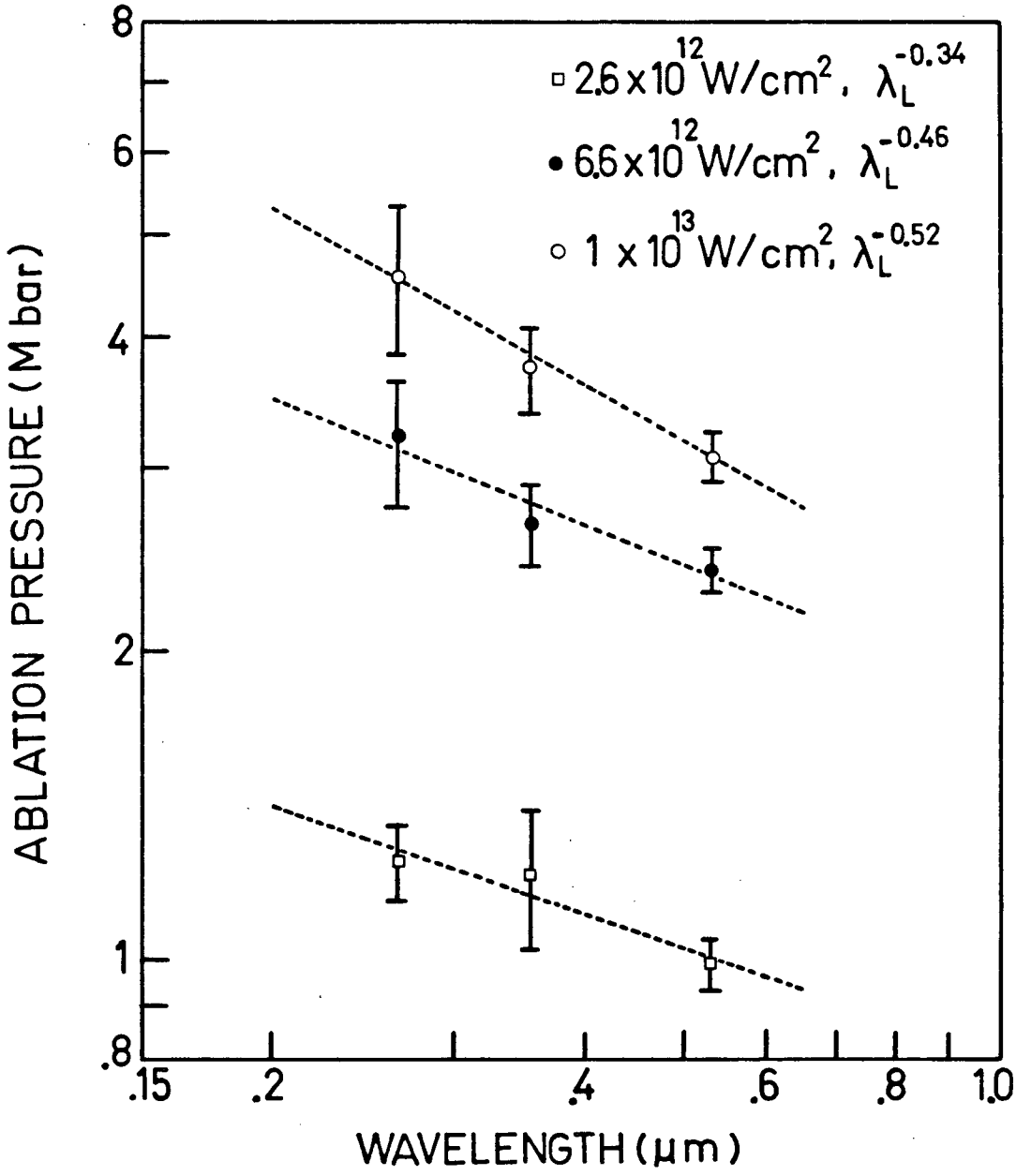

Figure 8–6 Wavelength dependence of ablation pressure at absorbed irradiances of 2.6×10^{12}, 6.6×10^{12} and 10^{13} W/cm^2.

absorption regime the following scaling laws for the mass ablation rate and the ablation pressure are expected:

$$\begin{aligned} \dot{m} &\sim I_A^{5/9}\lambda_L^{-4/9} \quad , \\ P_A &\sim I_a^{7/9}\lambda_L^{-2/9} \quad . \end{aligned} \tag{8-9}$$

Evidently, the intensity scalings of both $\dot{m}$ and P_A are in reasonable agreement with the measured scalings (eq. $(8-6)$ and $(8-7)$). On the other hand the predicted wavelength dependence of $\dot{m}$ is much weaker than the measured scalings of $\lambda_L^{-1.15}$ to $\lambda_L^{-1.37}$ whereas the theoretical scaling for P_A is also weaker than the observed $\lambda_L^{-0.34}$ to $\lambda_L^{-0.57}$ dependences for irradiances of $2.6 \times 10^{12}, 6.6 \times 10^{12}$ and $10^{13}\mathrm{W/cm^2}$.

Most recently, Meyer and Thiell[15] observed that the total ablated mass measured in planar targets irradiated with 0.35 and 1.05 μm laser light also scaled as $\lambda_L^{-1.3}$. They further pointed out that in Mora's model for strong inverse bremsstrahlung absorption (see Chapter 4 Section $4-2-$D$-$ii), the density gradient length L in the coronal plasma was assumed constant whereas numerical simulations from a hydrodynamic code describing the laser-target interaction showed a steepening of the density gradient for decreasing wavelength. This resulted in a different scaling for n_0, the maximum density for laser absorption, namely:

$$n_0 \sim n_{cr} I_A^{1/3} \quad . \tag{8-10}$$

using this new expression for n_0 the scaling laws for strong inverse bremsstrahlung absorption becomes:

$$\begin{aligned} \dot{m} &\sim I_A^{5/9}\lambda_L^{-4/3} \quad , \\ P_A &\sim I_A^{7/9}\lambda_L^{-2/3} \quad . \end{aligned} \tag{8-11}$$

These modified scalings relations are in almost complete agreement with our measurements except for the wavelength dependence of P_A, particularly at irradiances near 10^{12} W/cm^2.

Similar variation of n_0 with n_{cr} was also observed in our one-dimensional hydrodynamic simulations[113]. However when the computer simulation was run to reproduce the

experimental conditions it indicated the following dependence for $\dot{m}$ and P_{Abl}:

$$\dot{m} \sim I_A^{0.56} \lambda_L^{-0.52} \quad ,$$
$$P_{Abl} \sim I_A^{0.78} \lambda_L^{-0.26} \quad . \qquad (8-10)$$

for $I_A = 2.6 \times 10^{13}$ W/cm^2. These predictions do not agree with our measurements. (Curiously, they reproduce the results of Mora's model which should have been wrong because, as it has been pointed out, the density n_0 is not properly estimated.) One possible cause for these discrepancies in the wavelength scaling of the mass ablation rate and ablation pressure is the X-rays emitted by the plasma. The conversion efficiency of laser radiation to X-rays is known[7] to be higher for shorter laser wavelengths as the laser energy deposition occurs at higher plasma densities. However, energy transport by X-rays was not included in the hydrocode simulations used to obtain the scaling laws given by equation $8-10$. Also the X-ray contribution to the calorimeter signals was not taken into account in our analysis of the measurements. Neglect of the X-ray emission could lead to an underestimate of the theoretical wavelength scaling law exponents and to an overestimate of the experimental wavelength scaling law exponents.

Let us first consider the effect of the X-ray radiation on the ablation process. The X-rays transport energy to the ablation surface more efficiently than the electrons and if more laser energy is converted into X-rays this will lead to a higher mass ablation rate and ablation pressure. Therefore, if a greater amount of laser energy is converted into X-rays for the shorter laser wavelength, this would lead to a stronger wavelength dependence for the mass ablation rate and the ablation pressure. Preliminary results[113] obtained by including the effect of X-ray radiation in our hydrocode showed, as expected, higher values for the mass ablation rate and the ablation pressure. They also revealed a stronger wavelength scaling. As for the effect of X-ray radiation on the experimental measurements, if the X-ray contribution to the calorimeter signal is important, the ion energy will be overestimated. Consequently, the mass ablation rate and the ablation pressure (see eq., $8-2$ and $8-3$) would also be overestimated. This would lead to an overestimate in the wavelength scaling for the mass ablation rate and the ablation pressure, since the X-rays emission is higher for shorter laser wavelength.

Chapter 9

Summary and conclusions

9–1 Experimental effort

In the course of this work, many diagnostics have been developed. These include a spherical photometer, a multichannel X-ray detector, pinhole cameras and an X-ray crystal spectrometer. An *in-situ* calibration technique for X-ray films as well as a procedure for the fabrication of multilayer thin film target were also developed.

9–2 Experimental results and conclusions

As theoretically predicted, inverse bremsstrahlung absorption is very effective for short wavelength laser radiation. This was established from the high level of absorption measured (> 90 %) as well as the scaling of electron temperature with laser intensity. From the observed X-ray spectrum, the absorbed energy was found to be well thermalized, with a cooler plasma temperature for the shorter laser wavelength and insignificant amount of hot electrons produced. Parametric processes did not play any significant role as evidenced by the low level of scattered light measured. All these measurements showed good agreement with theory and confirmed the results of many other workers. The advantageous effects of short wavelength radiation on energy coupling are evident.

An experimental investigation of electron thermal transport using multilayer targets was performed at 0.355 μm. This experiment represented the first measurement of the effect of target density on energy transport. However, because of two-dimensional hydrodynamics, the measurement was dominated by an edge effect yielding an apparently much larger laser ablation depth in the target. This has been successfully explained using a simple model. Since layered target measurements are widely used by other workers, the identification and the explanation of a problem associated with this diagnostic are important.

Scaling laws for the mass ablation rate and the ablation pressure were obtained at 0.532, 0.355 and 0.266 μm for intensities ranging from 10^{12} to 5×10^{13} W/cm^2. This constituted the first detailed measurements in a strictly classical regime where direct comparison with an analytical model is possible. The measurement showed that much more efficient energy transport is obtained for shorter laser wavelength as indicated by the increase in the mass ablation rate and ablation pressure. A very interesting observation is that the observed wavelength dependence is much stronger than predicted. The X-ray energy radiated by the plasma is identified as a plausible cause for this stronger wavelength dependence.

9–4 New contributions

The multichannel X-ray detector[70] (Rev. Sci. Inst. **54**, 1091 (1983)) used for plasma temperature measurements and the *in-situ* X-ray film calibration technique[69] (Appl. Opt. **23**, 762 (1983)) constitute new and original diagnostic developements in this work.

In terms of the physics understanding in laser-matter interactions, we have identified and successfully explained the anomalous laser penetration depths in layered targets[115] (Appl. Phys. Lett. **44**, 713 (1984)) where edge-effects are important. Furthermore we have obtained the first detailed measurements of the scaling laws for both the mass ablation rate and ablation pressure for laser-driven ablations in a classical and steady-state regime[116] (Appl. Phys. Lett. (1984)). The results have indicated the inadequacies of the existing analytical theories.

9–3 Suggestions for future work

Future fusion drivers will be operating at intensities ranging from 10^{14} to 10^{15} W/cm^2. In this intensity regime the plasma temperature will be higher and inverse bremsstrahlung may become less effective. Also the threshold for the parametric processes will be exceeded, leading to increased scattering and to the production of hot electrons. It will be important to pursue the study in this regime. Such studies can be made possible by upgrading the existing laser facility.

For a better understanding of the laser-target interaction the knowledge of the actual amount of energy radiated as soft X-rays is essential. In particular the X-ray emission has been identified as the possible cause for the differences between our measured wavelength

scaling laws and that predicted from analytical and numerical models. As a large amount of the X-ray energy emitted by the plasma is in the soft X-ray range, spectral information on the X-ray emission can be obtained using a grazing incidence vacuum spectrometer and temporal information using an X-ray streak camera.

Finally an independent measurement of the wavelength scaling of ablation pressure can be obtained from measurements of the velocity of the laser produced shock waves in solids. Such measurements will eliminate the uncertainties associated with ion expansion measurements such as the ablation area and the X-ray contribution to the ion energy determined by the calorimeters.

Bibliography

1. J.D. Lawson, Proc. Phys. Soc. London, **B70**, 6 (1957).

2. J. Nuckolls, L. Wood, A. Thiessen, G. Zimmerman, Nature, **239**, 139 (1972).

3. G.H. McCall, Plasma Physics, **25**, 237 (1983).

4. R.E. Kidder, *Physics of High Energy Density*, (edited by Caldirola, Academic, New York, 1971), p. 306 .

5. F Amiranoff, R. Fabbro, E. Fabre, C. Garban, J. Virmont, W. Weinfield, Phys. Rev. Lett. **43**, 522 (1979).

6. W.C. Mead, E.M. Campbell, K.G. Estabrook, R.E. Turner, W.L. Kruer, P.H.Y. Lee, B. Pruett, V.C. Rupert, K.G. Tirsell, G.L. Stadling, F. Ze, C.E. Max, M.D. Rosen, Phys. Rev. Lett. **47**, 1289 (1981).

7. W.C. Mead, E.M. Campbell, K.G. Estabrook, R.E.Turner, W.L. Kruer, P.H.Y. Lee, B. Priett, V.C. Rupert, K.G. Tirsell, G.L. Stradling, F. Ze, C.E. Max, M.D. Rosen, B.F. Lasinski, Phys. Fluids, **26**, 2316 (1983).

8. C. Garban-Labaune, E. Fabre, C.E. max, R. Fabro, F. Amiranoff, J. Virmont, M. Weinfeld, A. Michard, Phy. Rev. Lett. **48**, 1018 (1981).

9. W. Seka, R.S. Craxton, J. Delettrez, L. Goldman, R. Keck, R.L. McCrory, D. Shvarts, J.M. Soures, R. Boni, Opt. Comm. **40**, 437 (1982).

10. D.C. Slater, Gar.E. Bush, G. Charatis, R.R. Johnson, F.J. Mayer, R.J. Scheder, J.D. Simpson, D. Sullivan, J.A. Tarvin, C.E. Thomas, Phys. Rev. Lett. **46**, 1199 (1981).

11. H. Nishimura, H. Azechi, K. Yamada, A. Tamura, Y. Inada, F. Matsuoka, M. Hamada, Y. Susuki, S. Nakai, C. Yamanaka, Phys. Rev. A **23**, 2011 (1981).

12. B. Yaakobi, T. Boehly, P. Bourke, Y. Couturie, R.S. Craxton, J. Delettrez, J.M. Forsyth, R.D. Frankel, L.M. Goldman, R.L. McCrory, M.C. Richardson, W. Seka, D. Shvarts and J.M. Soures, Opt. Comm. **39**, 175 (1981).

13. T.J. Goldsack, J.D. Kilkenny, B.J. MacGowan, S.A. Veats, P.F. Cunningham, C.L.S. Lewis, M.H. Key, P.T. Rumsby, W.T. Toner, Opt. Comm. **42**, 55 (1982).

14. M.H. Key, W.T. Toner, T.J. Goldsack, J.D. Kilkenny, S.A. Veats, P.F. Cunningham and C.L.S. Lewis, Phys. Fluids **26**, 2011 (1983).

15. B. Meyer and G. Thiell, Phys. Fluids **27**, 302 (1984).

16. C.E. Max *Laser-plasma interaction* (edited by R. Balian and J.C. Adam, North-Holland Publishing compagny, 1982), p.304 .

17. J.M. Dawson and C. Oberman, Phys. Fluids, **5**, 517 (1962).

18. T.W. Johnston, J.M. Dawson, Phys. Fluids, **16**, 722 (1973).

19. V.P. Silin, Sov. Phys. J.E.T.P. **20**, 1510 (1965).

20. A.B. Langdon, Phys. Rev. Lett. **44**, 575 (1980).

21. N.G. Denisov, Sov. Phys. J.E.T.P. **4**, 5444 (1957).

22. J.P. Freidberg, R.W. Mitchell, R.L. Morse and L.I. Rudsinski, P.R.L. **28**, 795 (1972).

23. V.L. Ginzburg, *The propagation of electromagnetic waves in plasma* , (Pergamon Press, London, 1964) p.213 .

24. C.N. Lashmore-Davies *Plasma physics and nuclear fusion research*, (edited by R.D. Gill, Academic Press, London, 1981), p.349 .

25. J.P. Freidberg, R.W. Mitchell, R.L. Morse, L.I. Rudsinski, Phys. Rev. Lett. **28**, 795 (1972).

26. K. Estabrook and W.L. Kruer, Phys. Rev. Lett. **40**, 42 (1978).

27. K.G. Estabrook, E.J. Valeo, W.L. Kruer, Phys. Fluids, **18**, 1151 (1975).

28. J.R. Albritton and A.B. Langdon Phys. Rev. Lett. **45**, 1794 1980).

29. F. Chen *Introduction to plasma phusics*, (Plenum Press, New York, 1^{st} edition, 1974), p.256 .

30. P.K. Kaw, W.L. Kruer, C.S. Liu, K. Niskikawa, *Advances in Plasma Physics*, (Wiley and Sons, New York, 1976), Vol.16 .

31. W.L. Kruer, Comments on Plasma Physics and Controlled Fusion **6**, 161 (1981).

32. F.W. Perkins and J. Flick, Phys. Fluids, **14**, 2012 (1971).

33. M.N. Rosenbluth, Phys. Rev. Lett. **29**, 565 (1972).

34. J. Jeans, *An introduction to the kinetic theory of gases* (Cambridge, England : At the University Press, 1940), p.47 .

35. S.I. Braginskii, *Review of Plasma Physics* (Consultants Bureau, New York, 1965), Vol.1 .

36. L. Spitzer and R. Härm, Phys. Rev. **89**, 977 (1952).

37. C.E. Max, C.F. McKee and W.C. Mead, Phys. Fluids **23**, 1620 (1980).

38. D.R. Gray and J.D. Kilkenny, Plasma Physics **22**, 81 (1980).

39. L.L. Cowie and C.F. McKee, Astrophys. J. **211**, 135 (1977).

40. R.C. Malone, R.L. McCrory, and R.L. Morse, Phys. Rev. Lett. **34**, 721 (1975).

41. W.L. Kruer, Comments Plasma Phys. Controlled Fusion **5**, 69 (1979).

42. M.G. Haines, in *Proceedings of the 20th Scottish Universities Summer School in Laser-plasma Interactions* (edited by R.A. Cairns and J.J. Sanderson, Scottish Universities Summer School in Physics, Edinburgh, 1980).

43. A.R. Bell, R.G. Evans, and D.J. Nicholas, Phys. Rev. Lett. **46**, 243 (1981).

44. J.P. Matte and J. Virmont, Phys. Rev. Lett. **49**, 1936 (1982).

45. D.J. Bond, Phys. Lett. **88A**, 144 (1982).

46. J.F. Luciani, P. Mora, J. Virmont, Phys. Rev. Lett. **51**, 1664 (1983).

47. C.E. Max, W.M. Manheimer and J.J. Thomson, Phys. Fluids **21**, 128 (1978).

48. J.A. Stamper, E.A. McLean, and B. Ripin Phys. Rev. Lett. **40**, 1177 (1978).

49. D.W. Forslund, J. Geophys. Res. **75**, 17 (1970).

50. R.J. Bickerton, Nuclear Fusion **13**, 457 (1973).

51. Lawrence Livermore National Laboratoty Report No. UCRL-85246, 1979, and references therein.

52. W.E. Manheimer, Phys. Fluids **20**, 265 (1977).

53. A.R. Bell, Phys. Fluids **26**, 279 (1983).

54. E. Fabre, F. Amiranoff, F. David, R, Fabro, C. Garban-Labaune, R. Pellat, J. Virmont, in *Proceedings of the Conference on Plasma Physics and Controlled Nuclear Fusion Research, Vienna, Austria, 1980,* (International Atomic Energy Agency, Vienna, 1981), Paper No. IAEA - CN - 38/1-4.

55. C.E Max, C.F. McKee and W.C. Mead, Phys.Fluids **23**, 1620, (1980).

56. W.M. Manheimer and D.G. Colombant, Phys. Fluids **25**, 1644 (1982).

57. P. Mora, Phys. Fluids **25**, 1051 (1982).

58. R. Fabro, E. Fabre, F. Amiranoff, C. Garban-Labaune, F. Virmont, M. Weinfeld, Phys. Rev. A **26**, 2289 (1982).

59. P. Celliers, M. A. Sc. Thesis, The University of British Columbia, (1983).

60. R. Fabro, Thèse de Doctorat, Université de Paris Sud Centre d'Orsay, (1982).

61. A. Caruso and R. Gratton, Plasma Physics **10**, 867 (1968).

62. C. Fauquignon and F. Floux, Phys. Fluids **13**, 386 (1970).

63. J. L. Bobin, Phys. Fluids **14**, 2341 (1971).

64. J.J. Duderstadt and G.A. Moses, *Inertial confinement fusion* (John Wiley & Sons, Inc. New York, 1982), p.72 .

65. J.E. Allen, J.G. Andrews, J. Plasma Phys. **4**, 187 (1970).

66. J. Denavit, Phys. Fluids **22**, 1384 (1979).

67. R.E. Kidder, Nucl. Fusion **16**, 3 (1976) ; and in *Laser Interaction and Related Plasma Phenomena*, edited by H. Schwarz and H. Hora (Plenum, New York, (1977), Vol. 4B, p. 1007 .

68. K.A. Brueckner and S. Jorna, Rev. Mod. Phys. **46**, 325 (1975); T.P. Hughes, *Plasma and Laser Light* (Wiley, New York, 1975).

69. D. Pasini, A. Ng and A.J. Barnard, Appl. Opt. **23**, 762 (1984).

70. A. Ng, K. Fong, A.J. Barnard, J. Kwan and D. Pasini, Rev. Sci. Inst. **54**, 1091 (1983).

71. Kodak Laboratory and speciality chemicals, Eastman Kodak company, Rochester, New York 14650 U.S.A.

72. F. Grun and G.W. Luckey, Appl. Opt. **7**, 2289 (1968).

73. E.B. Rosa, A.H. Taylor, *Scientific Papers of Bureau of Standards Vol 18 no.447* (1922).

74. R.D. Bleach, D.J. Nagel, J. Appl. Phys. **49**, 3832 (1978).

75. D.L. Matthews, L.N. Koppel, E.M. Campbell, J.T. Larsen, V.W. Slivinsky, S.M. Lane, N.M. Ceglio, Appl. Phys. Lett. **10**, 951 (1982).

76. J. Mizui, N. Yamaguchi, T. Yamanaka, C. Yamanaka, Phys. Rev. Lett. **39**, 619 (1977).

77. A. Zigler, H. Zmora, J.L. Schwob, Phys. Lett. **63A**, 275 (1977).

78. J.C. Couturaud, P.A. Holstein, M. Louis-Jacquet, B. Meyer, G. Thiell, Nuclear Fusion **21**, 1657 (1981).

79. K.M. Glibert, J.P. Anthes, M.A. Gusinow, M.A. Palmer, R.R. Whitlock, M.A. Nagel, J. Appl. Phys. **51**, 1449 (1980).

80. J.D. Kilkenny, R.W. Lee, M.H. Key, J.G. Lunney, Phys. Rev. A **22**, 2746 (1980).

81. R.F. Benjamin, P.B. Lyons, R.H. Day, Appl. Opt. **16**, 393 (1977).

82. K.S. Weaver, J. Opt. Soc. of Amer. **40**, 524 (1950).

83. C.M. Dozier, D.B. Brown, L.S. Birks, J. Appl. Phys. **47**, 3732 (1976).

84. R.A. Armstead, Rev. Sci. Inst. **45**, 996 (1974).

85. E.B. Turner, *Plasma diagnostic techniques*, (Academic Press, New York, 1965), p.345.

86. Société Kodak-Pathé, 18, Georges V, Paris - 8e, France.

87. The Grant Line measuring comparator, Grant Instruments, 1805 E. Shore Highways, Berkeley, California, U.S.A.

88. B.L. Henke, R.L. Elgin, *Advances in X-ray analysis, Vol.13* (Plenum, New york, 1970) p.639.

89. PIN Diode 100-PIN-250 N: Quantrad Corporation, 19900 S.Normandic Avenue, Torrence, California 90502 U.S.A.

90. H.G. Ahlstrom, *Physics of Laser Fusion Vol. II* (National Laboratory publication, California 1982), p.109.

91. F.C. Jahoda, E.M. Little, W.E. Quinn. G.A. Sawyer and T.F. Stratton, Phys. Rev. **119**, 843 (1960).

92. EG & G, Reticon, Sunnyvale, CA94086 U.S.A.

93. Application Note #101, EG & G, Reticon, Sunnyvale, CA94086 U.S.A.

94. R.S.M. Revel and A.W. Agar, British J. of Appl. Phys. **6**, 23 (1955).

95. Polystyrene Q-Dope #10-3704 G.C.Electronics, Rockford, Illinois 61101 U.S.A.

96. D.B. Brown and M. Fatemi, J. Appl. Phys. **51**, 2540 (1980).

97. E.M. Campbell, M.D. Rosen, D.W. Phillion, R.H. Price, K. Estabrook, B.F. Lasinski, B.H. Ripin, Appl. Phys. Lett. **43**, 54 (1983).

98. W. Seka, J.L. Schwob and C. Breton, J. Appl. Phys. **42**, 315 (1971).

99. A. Zigler, H. Zmora, Y. Paiss and J.L. Schwob, J. Phys. D: Appl. Phys., **10**, L159 (1979).

100. F.C. Young, R.R. Whitlock, R. Decoste, B.H. Ripin, D.J. Nagel, J.A. Stamper, J.M. McMahon and S.E. Bodner, Appl. Phys. Lett. **30**, 45 (1977).

101. B. Yaakobi and T.C. Bristow, Phys. Rev. Lett. **38**, 350 (1977).

102. K.B. Mitchell and R.P. Godwin, J. Appl. Phys. **49**, 3851 (1978).

103. J.A. Tarvin, W.B. Fechner, J.T. Larsen, P.D. Rockett and D.C. Slater, Phys. Rev. Lett. **51**, 1355 (1983).

104. T.J. Goldsack, J.D. Kilkenny, B.J. MacGowan, P.F. Cunningham, C.L.S. Lewis, M.H. Key and R.T. Rumsby, Phys. Fluids **25**, 1634 (1982).

105. R. Decoste, J.C. Kieffer and H. Pépin, Phys. Rev. Lett. **47**, 35 (1981)

106. T. Kato, The Astrop. J. Supp. Series **30**, 397 (1976).

107. Ya.B. Zel'dovich and Yu.P. Raizer, *Physics of shock waves and high temperature hydrodynamics phenomenon*, (Academic Press, New York, 1966), p.49.

108. R.J. Trainor, J.W. Shanes, J.M. Auerbach, N.C. Holmes, Phys. Rev. Lett. **42**, 1154 (1979).

109. R.J. Trainor and Y.T. Lee, Phys. Fluids **25**, 1898 (1982).

110. T.P. Hughes, *Plasmas and laser light*, (John Wiley & Sons, New York, 1975) p.298.

111. W.C. Mead, E.M. Campbell, W.L. Kruer, R.E. Turner, C.W. Hatcher, D.S. Bailey, P.H.Y. Lee, J. Foster, K.G. Tirsell, B. Pruett, W.C. Holmes, J.T. Trainor, G.L. Stradling, B.F. Lasinski, C.E. Max and F. Ze, Phys. Fluids **27**, 1301 (1984).

112. M.K.Matzen and R.L.Morse, Phys. Fluids **22**, 654 (1979).

113. L. Da Silva, M.A.Sc. Thesis, The University of British Columbia, (1984).

114. J.S. Pearlman and M.K. Matzen, Sandia Laboratories Report SAND78-0229.

115. A. Ng. D. Pasini, P. Celliers, Appl. Phys. Lett. **44**, 713 (1984).

116. A. Ng, D. Pasini, D. Parfeniuk, L. Da Silva, J. Kwan, Appl. Phy. Lett. (Accepted for publication, 1984).

117. K. Fong, Ph. D. Thesis, The University of British Columbia, 1982 .

118. H.R. Griem, *Plasma spectroscopy*, (McGraw-Hill, New York, 1964), p.105 .

119. M.H. Key and R.J. Hutcheon, Adv. At. Mol. Phys. **16**, 201 (1980).

120. D. Duston and J.Davis Phys. Rev. **21**, 1664 (1980).

Appendix A

Temperature measurements from X-ray continuum emission

As first described by F.C.Jahoda et al.[91] the plasma electron temperature can be determined by measuring the X-ray continuum emission through absorber foils of various thicknesses and comparing the results to theoretically calculated spectrum. In this Appendix we discuss the method used in such calculations.

A–1 Transmitted X-ray spectrum for different plasma temperatures

The X-ray intensity behind an absorber foil of thickness D is obtained by integrating over wavelength the product of the absorber's transmission function and the intensity of the incident continuum,

$$I_{trans} = \int I_{inc}(\lambda, T_e) \exp[-\mu(\lambda) D]\, d\lambda \qquad (A-1)$$

where I_{trans} is the transmitted intensity, I_{inc} the incident intensity, $\mu(\lambda)$ the absorption coefficient of the filter used and D the filter thickness.

The following expressions were used for the absorption coefficient of aluminum foils:

$$\begin{aligned} \mu(\lambda) &= 4.776 - 7.32\lambda + 3.84\lambda^2 + 13.84\lambda^3 - 0.755\lambda^4 \quad \mathrm{cm}^2/\mathrm{g} \quad \text{for} \quad \lambda < 7.9\,\text{Å} \\ \mu(\lambda) &= 42 - 35\lambda + 6\lambda^2 + 0.3838\lambda^4 \quad \mathrm{cm}^2/\mathrm{g} \quad \text{for} \quad \lambda > 7.9\,\text{Å} \end{aligned} \qquad (A-2)$$

where λ is the wavelength in Å. These polynomials were obtained[88] from least square fit to values of the absorption coefficient between 100 eV and 12 keV tabulated by Henke[117].

For an optically thin homogeneous plasma of length l, the intensity I is related to the plasma emissivity ϵ by

$$I = \epsilon l \qquad (A-3)$$

The plasma emissivity is due both to recombination radiation and bremsstrahlung continuum emission it can be expressed as[118] :

$$\epsilon(\lambda, T_e) = 4.08 \times 10^{-23}\left(\frac{E_H}{kT_e}\right)\frac{Z^2 N_i^Z n_e}{\lambda^2}\exp\left(-\frac{hc}{\lambda k T_e}\right)$$
$$\sum_{\substack{E_{Z-1,n} \\ < hc/\lambda}} \left[g_{ff} + g_{fb}\frac{2Z^2 E_H}{n_e^3 kT_e}\exp\left(\frac{E_{Z-1,n}}{kT_e}\right)\right] \qquad (\text{erg s}^{-1}\ \text{cm}^{-3}\ \text{sr}^{-1}\ \text{Å}^{-1}) \qquad (A-4)$$

where E_H is the ionization potential of hydrogen, k the Boltzmann's constant, n_e the electron number density (cm^{-3}), T_e the electron temperature (eV) , N_i^Z the number density (cm^{-3}) of ion of charge Z calculated assuming a coronal equilibrium model, λ is the photon wavelength, $E_{Z,n}$ the ionization potential in eV of an electron in the n-th shell of an ion of charge state Z, n the lowest level that has a vacancy for radiative recombination and g_{ff} , g_{fb} the Gaunt factors for bremsstrahlung and recombination radiation respectively.

Using equations $(A-2)$, $(A-3)$ and $(A-4)$, repeated numerical integrations* of expression $(A-1)$ for the various foil thicknesses D yielded curves of the relative transmitted X-ray intensity versus the absorber thickness for different electron temperatures. These were then compared to our experimentally measured spectrum. In the evaluation of expression $(A-4)$ for calculating the ground state ion densities, a steady state coronal equilibrium was assumed. We wish now to discuss the validity of this assumption.

A–2 Applicability of the Coronal model

The most complete model to calculate the ion populations in a plasma is the collisional radiative model where all the possible excited states of the ions are taken into consideration. However because of the complexity of a full collisional radiative model computation, simpler approximate models are more commonly used[119]. In particular the Coronal model is used if the electron density is such that

$$n_e \leq 1.5 \times 10^{10} T_e^4 \chi^{-1/2} \qquad (\text{cm}^{-3}) \qquad (A-5)$$

* The computer program to perform these calculations was written by K. Fong[117]

where n_e is the electron density (cm^{-3}), T_e is the electron temperature in eV and χ is the ionization potential of an ion of charge Z. At the other extreme, the local thermodynamic equilibrium modele (LTE) is used if

$$n_e \geq 1.7 \times 10^{14} T_e^{1/2} \hat{\chi}^3(p,q) \qquad (cm^{-3}) \qquad (A-6)$$

where $\hat{\chi}(p,q)$ is the largest energy gap in the term scheme of the ion considered. Typical values for the plasma in our experiments were : $n_e \sim 4 \times 10^{21}$ cm^{-3}, $T_e \sim 500$ eV and $\hat{\chi}(p,q) \sim \chi \sim 2000$ eV . The conditions $(A-5)$ and $(A-6)$ for these plasma conditions becomes:

$$n_e \leq 2.1 \times 10^{19} \quad (cm^{-3}) \qquad \text{for Coronal model}$$

$$n_e \geq 3.1 \times 10^{25} \quad (cm^{-3}) \qquad \text{for LTE model}$$

Thus we see that our plasma with $n_e \sim 4 \times 10^{21}$ cm^{-3} lies between the coronal and LTE regions and an accurate calculation of the ionization distribution should in principle employ the collisional radiative model.

In the following table we compare the calculation of the relative ion density populations for an aluminum plasma at $T_e = 500$ eV using computed values from our coronal model and published[20] collisional radiative values.

Table A-1

Comparison between Coronal and Collisional radiative model calculations

Relative ion density population	Coronal model	Collisional radiative model
N^{+10}/N_{Total}	.006	.008
N^{+11}/N_{Total}	.853	.74
N^{+12}/N_{Total}	.136	.24
N^{+13}/N_{Total}	.005	.005

A Coronal model approximation is probably rather crude for calculating the line emission where the population of the bound states have to be known. However for calculating the recombination radiation, only the total relative population density of a given type of ion need to be known and the results of the above table show that it is well justified to use a Coronal model calculation.